THE EFFECTS OF RADIATION ON MEMRISTOR-BASED ELECTRONIC SPIKING NEURAL NETWORKS

by

Sumedha Gandharava Dahl

A dissertation

submitted in partial fulfillment

of the requirements for the degree of

Doctor of Philosophy in Electrical and Computer Engineering

Boise State University

August 2020

BOISE STATE UNIVERSITY GRADUATE COLLEGE

DEFENSE COMMITTEE AND FINAL READING APPROVALS

of the dissertation submitted by

Sumedha Gandharava Dahl

Dissertation Title: The Effects of Radiation on Memristor-Based Electronic Spiking Neural Networks

Date of Final Oral Examination: 10 June 2020

The following individuals read and discussed the dissertation submitted by Sumedha Gandharava Dahl, and they evaluated their presentation and response to questions during the final oral examination. They found that the student passed the final oral examination.

Kurtis D. Cantley, Ph.D.	Chair, Supervisory Committee
Kristy A. Campbell, Ph.D.	Member, Supervisory Committee
Benjamin C. Johnson, Ph.D.	Member, Supervisory Committee

The final reading approval of the dissertation was granted by Kurtis D. Cantley, Ph.D., Chair of the Supervisory Committee. The dissertation was approved by the Graduate College.

DEDICATION

To

DR. BHOJ RAJ SINGH

and

KARL B. DAHL

ACKNOWLEDGMENTS

I would like to sincerely thank my Ph.D. advisor, Dr. Kurtis Cantley, for his advice, supervision, guidance, motivation, and support throughout the duration of this research work. Dr. Kurtis Cantley's constant encouragement inspired me to persist and persevere through the challenges, failures, and obstacles I faced during my Ph.D. research work.

I would also like to thank my committee members Dr. Kris Campbell and Dr. Ben Johnson for their advice, constructive critique, and guidance. I would also like to acknowledge my research group members Robert Ivans, Sepideh Rastegar and Sierra Bush for their help, support and motivating discussions.

I am also grateful for the help provided by the Department of Electrical and Computer Engineering (ECE) at Boise State University. ECE department provided all the research facilities, lab, classroom access, and support from staff, which made the research and compilation of this dissertation possible.

ABSTRACT

In this dissertation, memristor-based spiking neural networks (SNNs) are used to analyze the effect of radiation on the spatio-temporal pattern recognition (STPR) capability of the networks. Two-terminal resistive memory devices (memristors) are used as synapses to manipulate conductivity paths in the network. Spike-timing-dependent plasticity (STDP) learning behavior results in pattern learning and is achieved using biphasic shaped pre- and post-synaptic spikes. A TiO_2 based non-linear drift memristor model designed in Verilog-A implements synaptic behavior and is modified to include experimentally observed effects of state-altering, ionizing, and off-state degradation radiation on the device. The impact of neuron "death" (disabled neuron circuits) due to radiation is also examined.

In general, radiation interaction events distort the STDP learning curve undesirably, favoring synaptic potentiation. At lower short-term flux, the network is able to recover and relearn the pattern with consistent training, although some pixels may be affected due to stability issues. As the radiation flux and duration increases, it can overwhelm the leaky integrate-and-fire (LIF) post-synaptic neuron circuit and network does not learn the pattern. On the other hand, in the absence of the pattern, the radiation effects cumulate and the system never regains stability. Neuron-death simulation results emphasize the importance of non-participating neurons during the learning process, concluding that non-participating afferents contribute to improving the learning ability of the neural network. Instantaneous neuron death proves to be more detrimental for the network compared to when the afferents die over time thus, retaining network's pattern learning capability.

TABLE OF CONTENTS

LIST OF FIGURES

LIST OF ABBREVIATIONS

ANNs	Artificial Neural Networks
CBRAM	Conductive Bridging Random Access Memory
CG	Control Gate
CMOS	Complementary Metal-Oxide-Semiconductor
ESNNs	Electronic Spiking Neural Networks
LIF	Leaky Integrate-and-Fire
MIM	Metal-Insulator-Metal
MOSFET	Metal-Oxide-Semiconductor Field-Effect-Transistor
non-SNN	non-Spiking Neural Networks
PCM	Phase Change Memory
RRAM	Resistive Random Access Memory
SDC	Self-Directed Channel
SNNs	Spiking Neural Networks
STDP	Spike-Timing-Dependent Plasticity
TEAM	ThrEshold Adaptive Memristor Model
TEM	Transmission Electron Microscopy

CHAPTER 1: INTRODUCTION

The human brain's ability to learn and adapt is a hallmark for intelligence. It can process multiple streams of information simultaneously while using very little energy. The average human brain has billions of neurons and trillions of synaptic connections [1]. It is extremely difficult to model the vastness and complexities of the human brain partially because its operation is still not completely understood and partially because our computing technology is not advanced enough. Presently, the fastest supercomputer, OLCF-4, developed by IBM for Oak Ridge National Lab is capable of operating at 200 petaFLOPS (10^{15}) and the human brain is postulated to operate at 1 exaFLOPS (10^{18}) [2]. That said, researchers, today are working to mimic the behavior of complex biological networks using electronic artificial neural networks.

Artificial neural networks (ANNs) are densely connected computing systems inspired by the topology of biological neural networks. ANNs are adept at processing massive amounts of information in parallel and have the ability to derive meaning from complicated or imprecise data by recognizing complex patterns and trends. ANNs can adapt based on the inputs such that they can independently determine the action they need to take. ANNs also have the ability to learn new functions without help based on the inputs and deduce reasonable output. A trained ANN can perform visual recognition [3], character recognition [4], voice-activated assistance [5], stock market forecasting [6], and are used in self-driving cars [7]. Presently, multilayer/deep ANNs (having multiple hidden layers of neurons between input and output layers) are designed using complicated algorithms. Any

successful hardware implementation of ANNs with a computer becomes a complex task, as they require higher processing speed and system memory. Custom-designed hardware can reduce the implementation cost, increase the processing speed, and simplify the whole network [8].

A memristor is a non-linear passive two-terminal electrical component relating electric charge and magnetic flux (see Section 0). They are nonvolatile analog memories that are programmable, consume relatively low power, are manufactural at the nanoscale, have high density, and function very similar to biological synapses [9], [10]. Due to all these properties, memristors have been emerging as viable candidates for electronic spiking ANNs. Memristors are widely expected to be used in future electronic spiking neural network implementations.

Industry pioneers are designing neural networks that can also be used in solar radiation forecasting, object classification and matching, event filtering, facial recognition, combat automation, target identification, and weapon optimization [11]–[15]. Future systems are expected to be even more deeply biologically inspired, using pulses or spikes to transfer data between elements as opposed to continuous variables and activation functions. Customized hardware implementations will enable these spiking neural networks (SNNs) to be not only highly efficient but also incredibly robust and fault-tolerant. Therefore, SNNs will find numerous applications in harsh, radiation-filled environments such as space or at nuclear and military installations to carry out a wide variety of missions. Presently, shielding and hardening are common practices to protect devices and circuits from radiation, but these techniques are unable to block all particles from interacting with underlying electronics [16], [17]. It is therefore important to observe,

model, and simulate the effects of radiation on electronic SNNs so that more robust networks can be designed for these applications.

This dissertation explores resistive memory devices and models that could be used as electronic synapses. Further, radiation effects on the memristive devices are studied and a behavioral model is modified to include these effects. The memristor model is used to design a feed-forward fully connected neural network for spatio-temporal pattern recognition. Learning in the network is achieved using spike-timing-dependent plasticity (STDP) learning behavior. The effects of the radiation on the STDP learning rule, system stability, and pattern learning ability of the spiking neural network are reported in this dissertation. Lastly, the effect of the neuron death on SNN is also discussed.

This chapter will provide a detailed background and the literature review on biological brain anatomy, neural networks, electronic synapses, memristive devices, and radiation basics. These basic components provided the necessary motivation for the approaches used in this research. Section 0 will summarize the highlights of the research and overview of the following chapters.

1.1 Biological Neural Networks

The core component of the human nervous system is the brain, which contains cells known as neurons. Neurons are electrically excitable and communicate with each other by electro-chemical signaling through synapses, which form at the connection points. The human brain consists of more than 100 billion neurons and each neuron is connected to as many as 20,000 synapses (Purkinje cell in the cerebellum) [1].

A neuron, as illustrated in Figure 1.1, consists of three basic parts: soma (cell body containing the nucleus), dendrites (branches extending away from the soma forming a

"dendritic tree") and a single axon (nerve fiber extending from the soma and much longer than other dendrites).

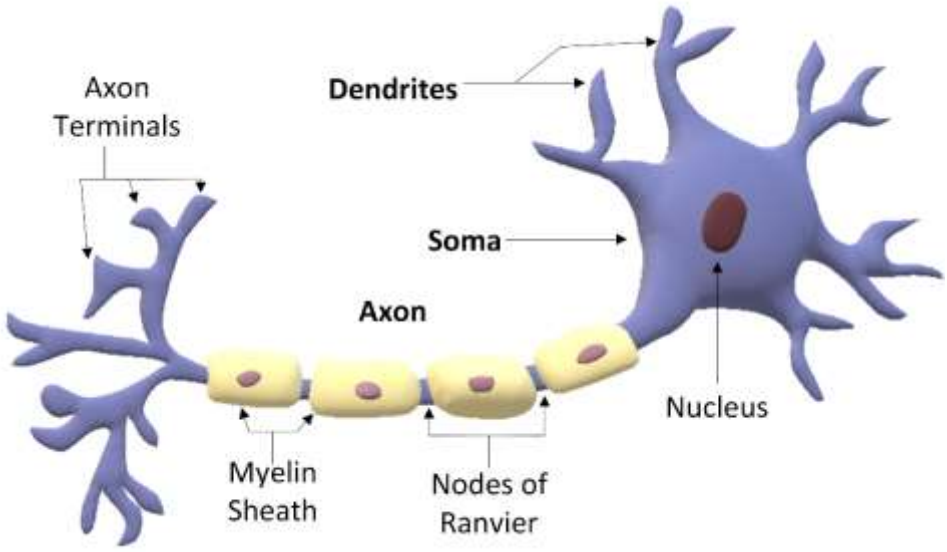

Figure 1.1 llustration of a typical neuron structure and its common anatomical features. The figure is adapted from https://commons.wikimedia.org/wiki/File:Neuron-nl.svg.

The neuron sends out spikes of electrical activity through the axon but collects signals from other neurons through dendrites. Neurons maintain a voltage gradient across their membrane with the help of sodium, potassium, chloride, and calcium ions. Due to the change in concentration of these ions, the voltage gradient may change significantly, depolarizing the neuron [18]. In such a case, the nucleus will generate an electrochemical pulse called an action potential, similar to one in Figure 1.2, which travels down its axon. A neuron requires a threshold of about −30 to −50 mV to initialize an action potential, throughout the firing process the membrane potential reaches about 40 mV in humans. A neuron may take about 1 ms of the refractory period to reach its resting state after reaching action potential [1], [19].

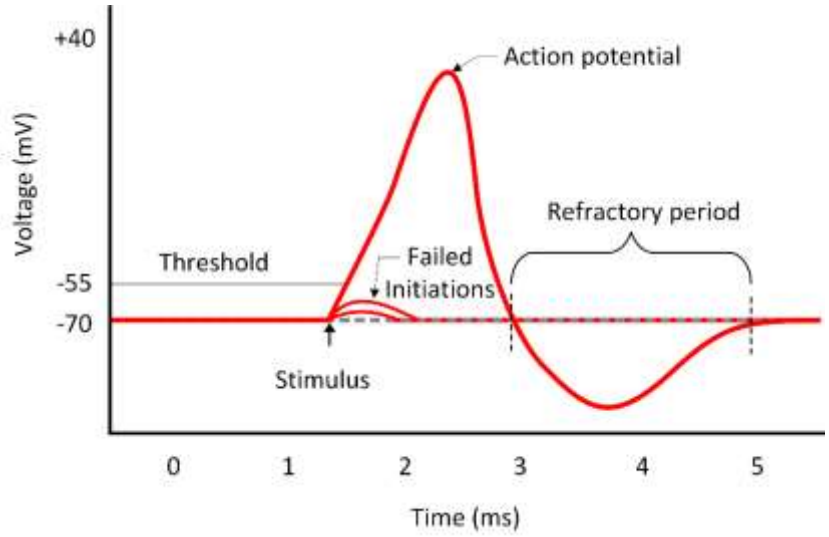

Figure 1.2 Approximation of an action potential generated by a neuron [20]. The figure is published under the Create Commons license and is adapted from https://commons.wikimedia.org/wiki/File:Action_potential.svg.

Myelin sheath (found in long-range never connections) is sometimes wrapped around the axon, as shown in Figure 1.1, facilitates the flow of the action potential across the axon by providing electrical insulation. The Nodes of Ranvier refreshes the action potential as it travels down the long distance, as they are the centers of voltage-gated sodium channels [1], [19]. A typical neuron may fire anywhere from five to fifty times every second. As action potential reaches the axon terminal, as in Figure 1.1, it is ready to be transmitted to another neuron via a connection called a synapse.

A synapse is a junction between two neurons that facilitates transmission of the action potential between two neurons, and this transmission is the synaptic connection. A synaptic cleft is a small gap between two neurons, as seen in Figure 1.3. Synapses are about 20 to 40 nm wide but they can vary in size, structure, and shape. Synapses are mostly unidirectional and are most commonly observed between the axon-dendrite, as shown in Figure 1.3, but there are a few found between dendrite-dendrite, axon-axon, or dendrite-axon [21].

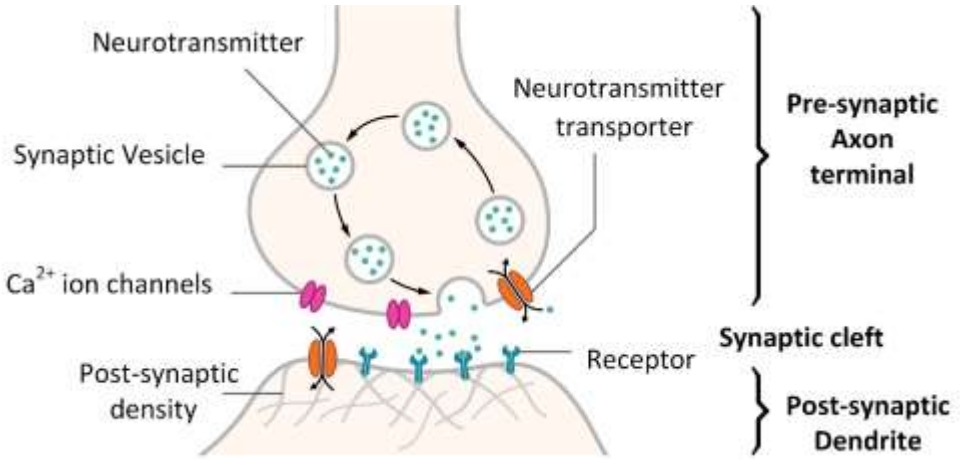

Figure 1.3 Illustration of the anatomy of a chemical synapse axon to dendrite communication. During an action potential, the synaptic vesicle releases the neurotransmitters defining synaptic weight. Neurotransmitters received by the post-synaptic dendrite contribute to simulate the action potential in the post-synaptic neuron [22]. The illustration is published under the Create Commons license and is adapted from https://commons.wikimedia.org/wiki/File:SynapseSchematic_en.svg.

The pre-synaptic neuron's axon terminals contain multiple membrane-bound synaptic vesicles filled with neurotransmitter molecules (like the amino acids glutamate, adrenaline, and GABA) as shown in Figure 1.3. When the neuron generates an action potential, Ca^{2+} ion channels open, increasing the ion concentration inside the cell that leads to the release of neurotransmitters into the synaptic gap between neurons. These neurotransmitters diffuse across the gap and bind to the receptors attached to the dendrites of the post-synaptic neuron. This changes the permeability of the receptor neuron membrane and as a result, the ion concentration inside the cell increases. Thus, the post-synaptic neuron sees the potential change. This process takes just a few milliseconds [21], [23].

1.2 Artificial Neural Networks

Artificial neural networks (ANNs) are systems that are inspired by biological neural networks like the brain. Today, we desire our ANNs to have the ability to derive meaning

from complicated or imprecise data. Contrary to biological neural networks, spiking ANNs have to be trained to perform every task from scratch, using a fixed topology chosen for the set task. The learning process takes more iterations and an ANN can be usually trained for one or only a few specific tasks. On the other hand, ANNs are 10 million times faster than biological networks and are over a million times less prone to error than the human brain. The human brain is slower but unlike ANNs, has massive parallel computing ability, and can work with multiple receptors on skin, ear, eyes, mouth, and skin at a time [24]. Even though the ANNs are still in their infancy, their development will be a significant step forward for humankind and will undoubtedly advance both neuroscience and engineering.

In literature, ANNs are designed by either using non-spiking neural networks (non-SNNs) or spiking neural networks (SNNs). Unlike non-SNNs, SNNs use the shape and size of the pulses to change the conductivity of the synapse similar to spike-timing-dependent plasticity (STDP). STDP is a biological process that changes the strength of the connection between neurons in the brain based on the pre- and post-synaptic neuron firing time. Non-SNNs can either be software-based deep learning networks implemented using software like Python, MATLAB, or TensorFlow, or they can be designed using hardware, these are true analog networks that use voltage signals and systems to implement their software counterparts. Similarly, SNNs can be software-based or hardware-based (electronic spiking neural networks). The following section compares the hardware and software-based spiking neural networks.

Compared to most ANNs, SNNs are more biologically realistic and potentially powerful [25]. They are designed using spiking neurons that transfer information via

precise timing or sequences of neural action potentials [26]. Neurons in biological neural networks are electrically excitable and communicate with each other by electrochemical signaling via synaptic connections. The strength of the connections between biological neurons is referred to as the synaptic weight, which changes over time depending on the pre- and post-synaptic neuron activity. Spike-timing-dependent plasticity (STDP) is one biological process that alters the weight depending on the pre- and post-synaptic neuron firing time. One way to implement STDP in electronic SNNs is to modify the time, shape, and magnitude of the action potentials appropriately.

1.2.1 Software-Based SNNs

In software-based SNNs, weight change, topology, and learning are defined using software algorithms implemented using a digital, or von Neumann architecture. The time difference between pre- and post-synaptic neurons is detected and synaptic weights are modified accordingly using the STDP rule. Many multi-layer SNN algorithms have been successfully implemented in software to solve practical problems like speech recognition [27], face recognition [28], handwriting recognition [29], and robot control [30].

Software-based SNNs lead to a tradeoff among accuracy, memory, and processing speed. The need for non-volatile synaptic weight storage becomes a concern because continuous updates and fetch-decode-execute cycles require significant power consumption. Another concern is the implementation of multilayer networks that need a readout of synaptic weights in each epoch. These are complicated to implement and add mismatches and communication errors into the network [10], [31], [32].

1.2.2 Hardware-Based or Electronic SNNs (ESNNs)

On the other hand, the physical realization of synapses using memristors is becoming a reality because they have the potential to solve many of the above-mentioned issues [33], [34]. Memristors are non-volatile and do not lose their state, thus eliminating the need for readout of synaptic weights and reducing communication overhead across the network. Unlike other non-volatile memories, memristors do not need to be refreshed to maintain their state, and this decreases the power consumption of the system. Hardware implementation of SNNs will not require complex algorithms and their scalability will solve the issue of chip area [10].

1.3 History of Electronic Synapses

In literature, electronic synapses are implemented using various electrical circuits and components. Past studies focus mainly on CMOS synapses, floating gate transistor synapses, and the memristive synapses that are discussed in this section. Since our brain has over a quadrillion synapses, a circuit that can mimic one synapse might not be very useful when scaled to a larger scale. Thus, lower density makes an electrical system very desirable as an electrical synaptic device because it will decrease power consumption and it will be more manageable and understandable.

1.3.1 CMOS Synapses

In 2003 Chicca et al. [35] designed a CMOS circuit where each synapse is represented using 14 transistors and two capacitors covering about 55 or145 μm × 31 μm in a 0.8 μm CMOS process. Later, in 2007, the Douglas team implemented the CMOS synaptic circuit on a chip with neurons in an array [36]. Using a 0.8 μm CMOS process the team successfully implemented a network of 32 neurons and 256 synapses in an area of

1.6mm^2. They were also expecting to implement a network of 32 neurons and 8000 synapses using .32 µm CMOS technology using a 10 mm^2 Si chip space [36].

In 2004 Asai et al. [37] implemented a synaptic circuit where they were able to significantly decrease the number of transistors to 5 with no capacitor required, as shown in Figure 1.4. This layout decreased the total area of each synapse to 35 µm × 36 µm with a 1.5 µm scalable CMOS rule. Unfortunately, they were not able to implement their synapses with a larger neural network because of the large values of parasitic capacitances across the wafer.

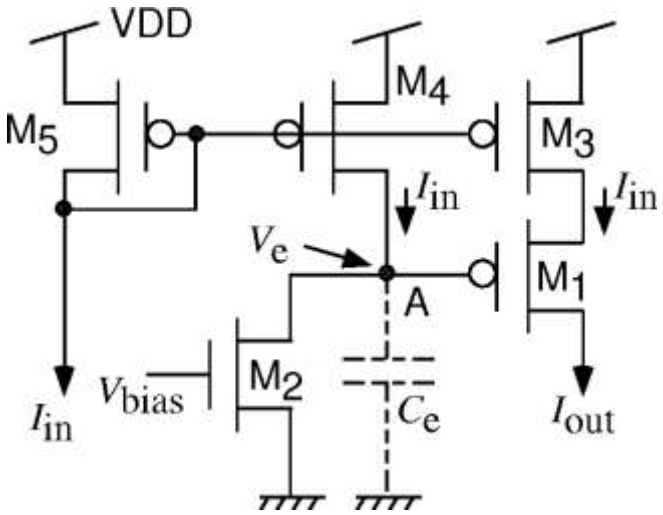

Figure 1.4 CMOS synaptic circuit with five transistors and no capacitor, thus decreasing the chip area considerably. Unfortunately, the circuit did not make it to the larger neural networks due to the presence of a large parasitic capacitor [37]. © 2005, 1EEE.

Implementation of CMOS synapse with a tunable pair-based STDP learning rule has been simulated in [38]. This design achieved a more biologically realistic STDP response while using fewer components than the energy-efficient synaptic circuit presented in [39].

It is very complicated if not impossible to design large neuromorphic circuits (~10^{15} synapses) where each CMOS synapse is implemented using multiple transistors and capacitors. Thus, scalability and extremely high density is the biggest concern in the case of CMOS synapses. On the other hand, a single floating gate transistor can represent one synapse, thus floating gate transistors were a more desirable representation of a synapse than CMOS transistors.

1.3.2 Floating Gate Transistor Synapses

Floating gate transistors work very similarly to flash memory cells and can be designed to store a range of charge states in the floating gate. The biggest advantage of using floating gate synapses was that their area can be scaled down.

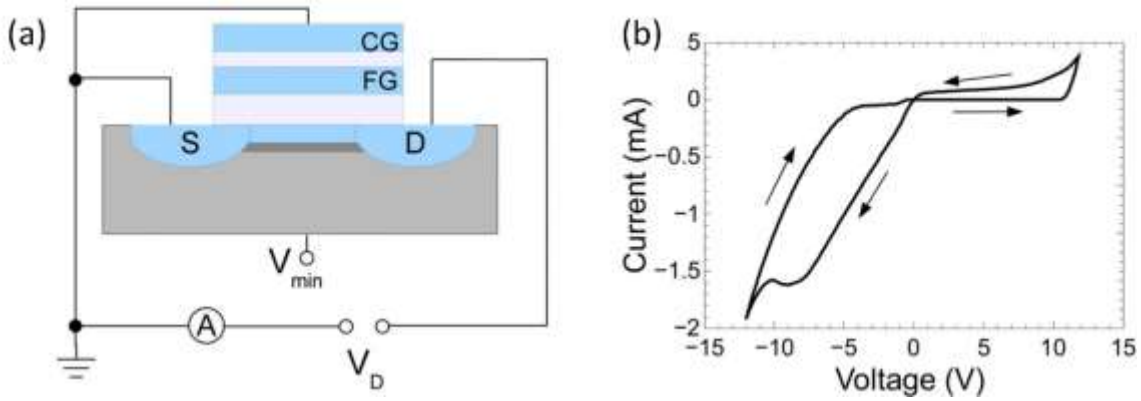

Figure 1.5 (a) Schematic of a two-terminal floatation gate transistor operating in memristive operation mode. Control gate (CG) and Source (S) are grounded while drain (D) sees the bias change. Bulk is kept at minimum voltage to avoid shorting with drain. (b) The pinched I-V characteristic of the said schematic [40]. The figure is reprinted from M. Pierce, Journal of Applied Physics 114, 194506 (2013), with the permission of AIP Publishing.

In 1996, Diorio et al. [41] designed a floating gate synapse. This synaptic transistor was nonvolatile, bidirectional, dependent on stored memory, compact, and operated off of a single polarity supply with low power consumption. To change the state of the device,

bias is applied to the Control Gate (CG as in Figure 1.5 (a)) that will inject the hot electrons to the Floating Gate, and Fowler–Nordheim tunneling is used to remove those electrons [41], [42].

By 2013, the Ziegler group [40] was able to design a synaptic floating gate transistor, its characteristics are depicted in Figure 1.5 (b) and are very similar to memristors. The resistance or conductance of the device is determined by the amount of charge stored on the floating gate capacitor. These devices had higher cycling capacity, better switching control, silicon technology compatibility, and were able to follow the Hebbian learning rule successfully. The floating gate had finite capacitance, which introduced a saturation limit for the synaptic weight [40].

Many more groups developed floating gate transistor synaptic arrays and circuits [43]–[47]. Unfortunately floating gate suffers from a SiO_2 trapping issue, making the devices unreliable and leading to a slower weight update [40]–[44].

1.3.3 Memristor Synapses

Memristors (discussed in detail in Section 0) are very similar to the synapses in our brains. In the brain, synapses facilitate communication between the neurons. Synaptic weight defines the strength of the connection between neurons, which is believed to enable our biological system to remember, forget, and function [36], [48], [49]. A memristor behaves similarly to synapse for it can store past state, giving it a characteristic hysteresis, as presented in Figure 1.8. Similar to synapses, memristors are the connections between the electronic neurons. Memristors can change their conductivity to make the connection between two electrical neurons more or less resistive based on the pre- and post-synaptic activity. Unlike most memristors, synapses are unidirectional and are chemically driven.

Synapses designed using multiple memristors are also studied in the literature, like memristor-based differential pair synapse [50], memristor-based bridge synapse [9], and multi-memristive synapse [51]. Multi-memristive synapses are used to increase the dynamic range and resolution of the synapses, differential pair synapse includes both short- and long-term synaptic plasticity, and bridge synapses improve the linearity of memristor over the synaptic weight range.

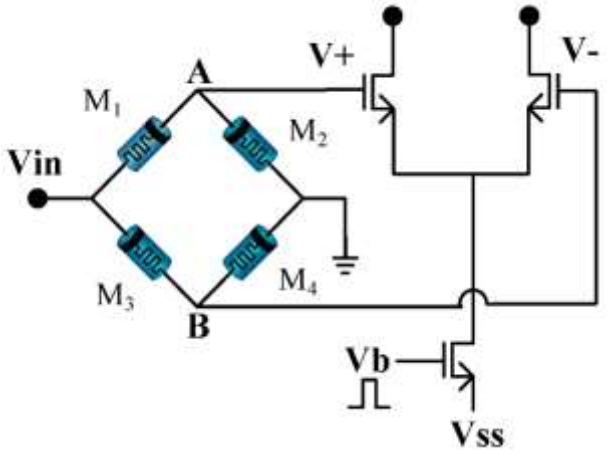

Figure 1.6 The schematic of memristor-based bridge synapse. V_{in} changes the weight of the memristors set-up as a voltage-divider circuit. The total synaptic weight across terminal A and B is converted to current by the three transistor differential amplifier added to the left [9], [10]. © 2012, 1EEE.

In 2011, Kim with Chua [9] introduced the concept of the memristor-based bridge synapse, as in Figure 1.6. The weight of the memristors is changed by varying in the input voltage "V_{in}" which will have the memristor set-up as a voltage-divider circuit. When V_{in} is positive, memristance of M_1 and M_4 will decrease but M_2 and M_3 will see the increase in memristance. In this case, the voltage at Node A will increase and represent the increase in synaptic weight. This synaptic weight is converted to current by the three transistor differential amplifier added to the left of the synaptic bridge circuit in Figure 1.6. This circuit was simulated with the neuron circuit to implement a 2-D image-processing task.

Each memristor size is projected to be less than 5 nm thus decreasing the synaptic area and the power consumed considerably less compared to the CMOS or the floating gate synapse (discussed in Section 0 and 0 [9].

In 2012, Adhikari et al. [10] went a step further and used the memristor bridge synapse to simulate a multilayer neural network and presented its learning behavior. The networks were successfully able to learn and solve the real-world problem of car detection. This simulation presented the possibility of using a memristor-synapse based neural network in real-world applications with the benefits of simpler architecture, reduced chip area, weight evolution linearity, and reduced power consumption [10].

A memristor has been successfully implemented as a synapse in literature in multiple other studies and multiple neural networks also supported the use of memristors as a synapse [52]–[56].

1.4 Memristors

Chua postulated the memristor in 1971 [57]; he defines it as the fourth basic circuit element along with the resistor, capacitor, and inductor. The four basic variables of voltage, charge, current, and flux associate the four basic circuit elements, as shown in Figure 1.7. The Ideal resistor is defined by the relationship between the current (i) and voltage (v) as $v = iR$. Similarly, the capacitor is defined by the charge (q) and voltage (v) as $dv = dq/C(q)$. The ideal inductor relates magnetic flux (φ) and current (i) as $d\varphi = L(i)\, di$. Chua postulated a memristor as a memory resistor defined by the relationship between flux (φ) and charge (q) as $d\varphi = M(q)\, dq$ [57]. He further expanded on this theory in references [57]–[63].

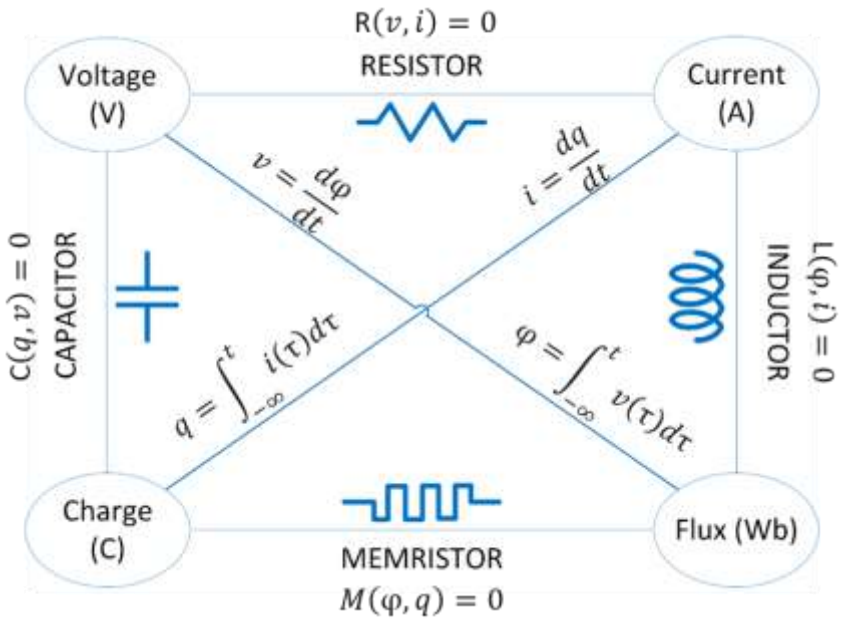

Figure 1.7 Four basic circuit elements and their relationship with each other via basic electrical variables [57]. The figure is adapted from [64].

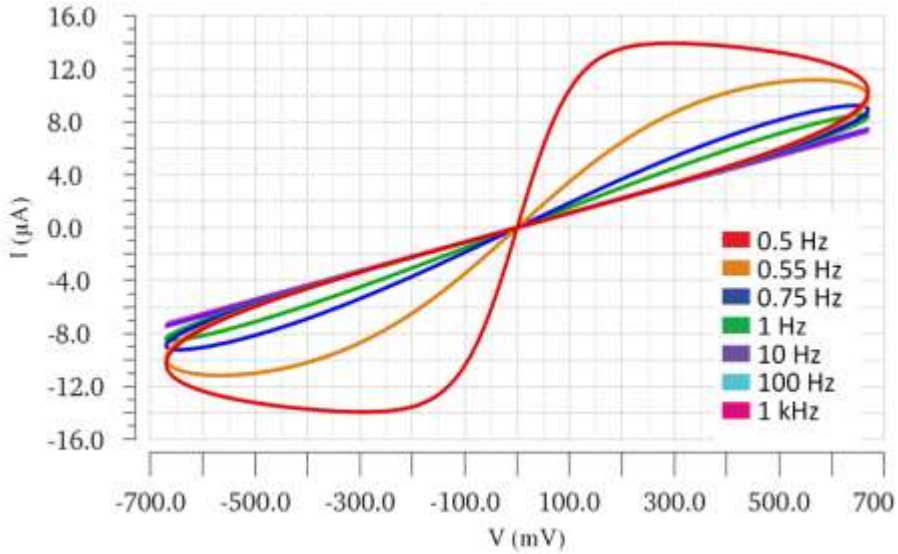

Figure 1.8 Memristor I-V characteristics resulting from 650 mV peak-to-peak sine pulse. Characteristics show a hysteresis loop pinched at zero, the area of hysteresis decreases with increasing frequency and becomes a straight line at very high frequency [65].

Chua [57]–[63] and many other researchers [65]–[68] show the electrical properties of the memristors. Figure 1.8 shows the I-V characteristics of a memristor from the behavioral memristor model used in this dissertation. For any device to be a memristor, it

should exhibit the following three characteristics [65]; a pinched hysteresis loop when a periodic signal is applied, the hysteresis lobe area must decrease monotonically as input frequency increases, and the pinched hysteresis loop must reduce to a line as frequency tends to infinity, as shown in Figure 1.8.

A typical memristor will change its resistance state when the desired bias is applied across it and will maintain this new resistance state until another set of sufficient bias changes it. A low resistance state is the set-state and the high resistance state is the reset-state. This property enables the memristor device to be used as a memory element. The memristive device can also show multiple intermediate states depending on the material and the switching mechanism of the device. The following section explains different types of memristors, see Figure 1.9 and their physical switching mechanisms.

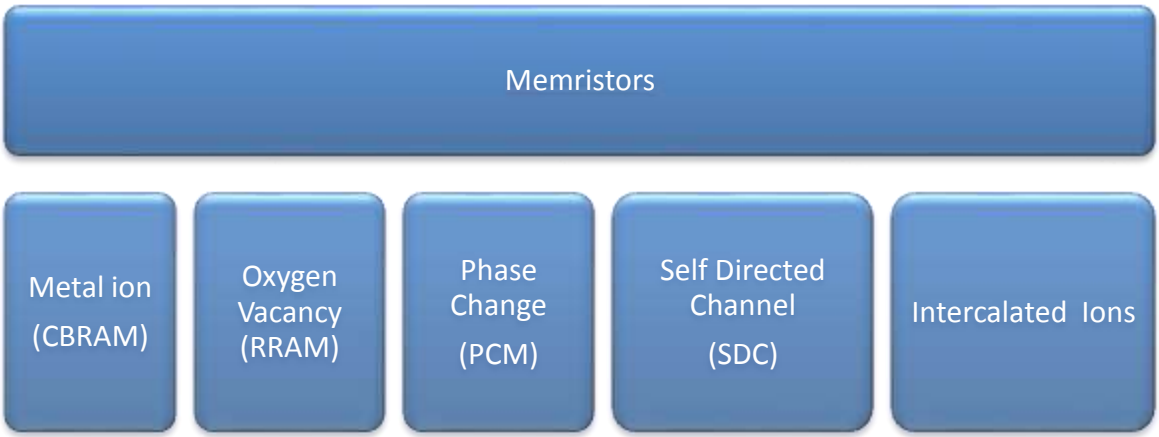

Figure 1.9 Classification of memristors based on their switching mechanism.

1.4.1 Metal Ion (Conductive Bridging RAM)

Conductive Bridging Random Access Memory (CBRAM) devices have a Metal-Insulator-Metal (MIM) structure [69]. The device structure is asymmetric, with one electrode as an active metal like Ag or Cu. Positive voltage oxidizes the active metal atoms

into ions, which migrate through the insulator layer under the applied electric field. The metal filament continues to grow until it reaches the other electrode. At this point, the connection completes and the device resistance decreases significantly, putting it in the set-state as shown in Figure 1.10 (a). A negative voltage is applied to reset the device, which reverses the electrochemical process and leads to retraction of the filament thus putting the device in the high resistance state as in Figure 1.10 (b) [69]–[71].

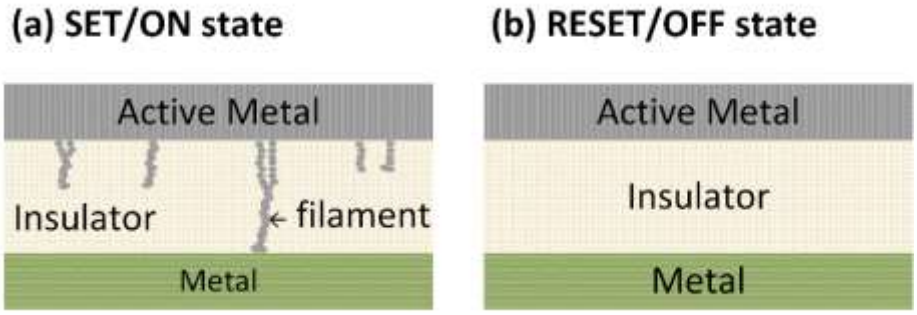

Figure 1.10 Illustration of CBRAM memristive device MIM structure. (a) The device is in low resistance state as the conductive active metal filament connects the top and the bottom electrode. (b) The metal filament is retracted to the top electrode, putting the device in a high resistance state. The figure is adapted from [72].

CBRAM devices are fabricated by multiple researchers, as in [73]–[81]. Typically Ag and Cu are the active metal for these devices due to their high ion mobility. It is observed in the previous research that the characteristics of CBRAM devices are mainly dependent on the active metal ion mobility, active metal oxidation rate and the supply of the ions forming the metal filament [69], [71], [82]. CBRAM devices are scalable, have fast switching time, low current, and high ON/OFF ratio. The CMOS compatibility study, however, indicates device variability and endurance issues with these devices [69], [71], [73], [75], [77], [80], [81].

1.4.2 Oxygen-Vacancy (RRAM)

In resistive random access memory (RRAM) devices, atoms reduced to anions migrate across the active layer. Most devices use oxygen-vacancies (V_O) in the migration process. Oxygen-vacancy memristors are also MIM devices, but unlike CBRAM, RRAM uses inert top and bottom electrodes and the oxygen ions are native to the active/switching layer. There is a built-in asymmetry in the device, as one of the oxide electrode interfaces will have a higher V_O concentration depending upon the metals used. As an electric field is applied, the concentration of V_O increases and diffuses through the active layer, forming a channel. This conductive channel can set and reset the device depending upon the bias applied across the device [69], [71], [83], [84].

Successful fabrication of RRAM devices is reported in [83]–[90]. Switching in these devices is the result of Joule heating, ionic motion and electrochemical reactions driven by the electric field [69], [71], [84], [86], [89]–[92]. RRAM devices show desirable characteristics like excellent scaling, multilevel switching (desirable for neuromorphic computing), high endurance and fast switching, but are usually accompanied by high programming current, device variability, low power efficiency and low on/off ratio [69], [71], [85], [87]–[89], [93].

1.4.3 Phase Change Memory (PCM)

PCM devices change their phases from amorphous to crystalline or vice-versa to change their resistive state. The amorphous phase presents the high resistance or reset-state and the crystalline state is the low resistance or set-state. To change the state of the device, bias is applied to melt the active layer, and then the device is quenched fast into the amorphous state or cooled slowly into the nucleation and growth state, thus crystallizing

the active layer. Thus, set and reset input pulses for PCM devices look very different [69], [94]–[96].

Many groups have successfully fabricated PCM devices as in [97]–[102]. As PCM is the first of the memristive devices, they are one of the most refined memristive devices and are in production by IBM, Micron, and Intel. PCM devices are observed to have low voltage unipolar switching and multilevel switching but are observed to have lower endurance, and higher current, thus higher power consumption and require relatively larger feature size [97], [102]–[105].

1.4.4 Self-Directed Channel (SDC)

SDC memristive devices are ion-conducting devices that change resistance as Ag^{+} moves into channels within its active layer. Permanent conductive channels formed in Ge_2Se_3 active layer via metal-catalyzed reaction contain Ag agglomerate sites. The Ag concentration determines the resistive state of the device. SDC device looks similar to the CBRAM that also uses Ag or Cu ions to change its resistance. However, SDC fabrication, structure (as in Figure 1.11), and working mechanisms are significantly different. SDC devices use Ge-rich chalcogenide glass and do not require photo-doping or thermal annealing. The Ag source and the active layer are separated by the SnSe layer thus avoiding Ag ion migration at high temperature [106].

In the first forming cycle, Sn ions generated from SnSe are forced into the active Ge_2Se_3 layer. Sn ions facilitate an energetically favorable substitution of Ag for Ge on the Ge-Ge bond, thus, creating Ag-Ge sites in the active layer that work as Ag agglomeration sites. The device resistance can be changed by adding or removing Ag from the agglomeration sites, without necessarily forming a metallic filament [106]. SDC devices

are observed to work well over a wide range of temperatures, have fast and multilevel switching, and provide low voltage switching thus low power consumption [106].

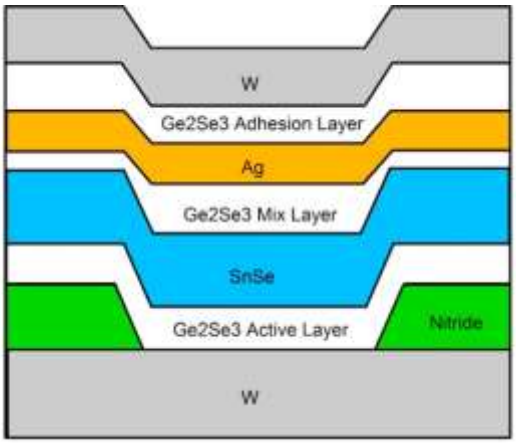

Figure 1.11 Layered structure of an SDC memristive device showing the separation Ge_2Se_2 active layer and Ag metal layer, thus making the device operable to higher temperatures. Layer thicknesses not to scale [106]. The figure is adapted from the article published under the Create Commons license, https://doi.org/10.1016/j.mejo.2016.11.006.

1.4.5 Intercalated Ions

Recently, in 2017, references [107] and [108] used Li and an organic polymer, respectively, to create a synaptic device for neuromorphic computing and a synaptic transistor for low power analog computing. These devices have great retention and low programming power, but both lag in switching speed, energy efficiency, and drive current. In 2018 [109] presented a three-terminal electrochemical graphene memristor and [110] designed a two-terminal monolayer MoS_2 device for synaptic computation. These devices have lower power consumption, good endurance, and show multilevel switching, but further improvements are required to improve energy efficiency and switching speed.

In three-terminal memristive devices [109], Li-ions intercalate between multi-layer graphene when current is applied at the reference electrode, shown in Figure 1.12 (b). The intercalated Li-ions make the graphene layer more conductive similar to the biological

synapse shown in Figure 1.12 (a). Thus, the resistivity of the graphene layer can be changed by changing the concentration of intercalated Li ions in the graphene as seen in Figure 1.12 (c). Li is chosen because it has been well characterized and has a high diffusion coefficient (7×10^{-5} cm^2s^{-1}) in a graphene bilayer, leading to fast switching speed [111], [112]. These memristive devices are compatible with CMOS and may find applications in flexible electronics [113], [114].

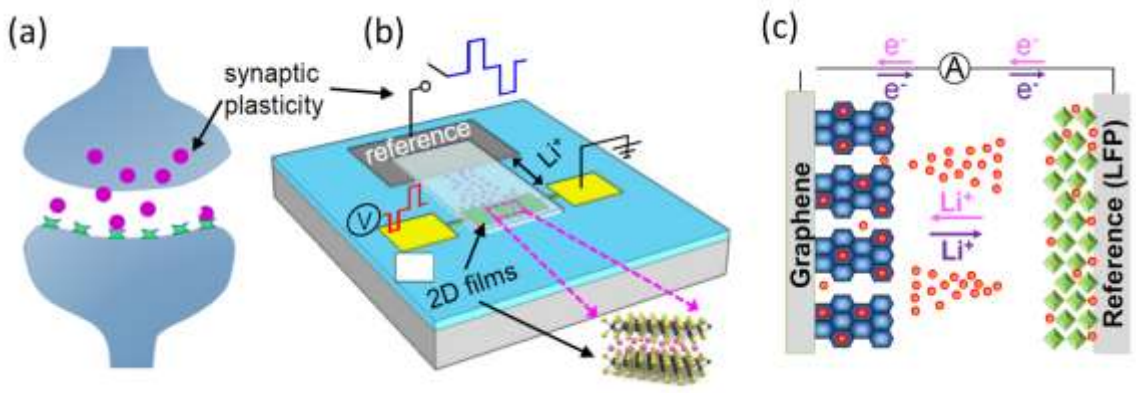

Figure 1.12 Intercalated Li-ion in graphene memristive device structure. (a) Schematic of a biologic synapse compared with (b) schematic of the graphene synapse, applying current at reference electrode changes the synaptic weight. Pink arrows zoom into the illustration of the intercalated Li ions into graphene. (c) The purple arrow indicates the de-intercalation of Li-ion out of graphene and the pink arrow shows the intercalation of Li ions moving into graphene [109]. © 2018 Wiley. Used with permission from Mohammad Taghi Sharbati, Yanhao Du, Jorge Torres, Nolan D. Ardolino, Minhee Yun, and Feng Xiong, Low- Power, "Electrochemically Tunable Graphene Synapses for Neuromorphic Computing", Advanced Materials, John Wiley and Sons.

1.5 Radiation

Radiation is the energy emitted as an unstable atom undergoes radioactive decay. Sources of radiation range from stars in space, to nuclear warheads, nuclear power plants, and nuclear accidents on earth. Radiation can be non-ionizing (have enough energy to vibrate the atoms in a molecule) or ionizing (can remove electrons from the atoms), which

can be detrimental to living things and electronic devices and circuits. Ionizing radiation can be in the form of fast-moving energy particles (alpha, beta, and neutrons) or electromagnetic rays (gamma and x-rays). The electromagnetic spectrum is presented in Figure 1.13.

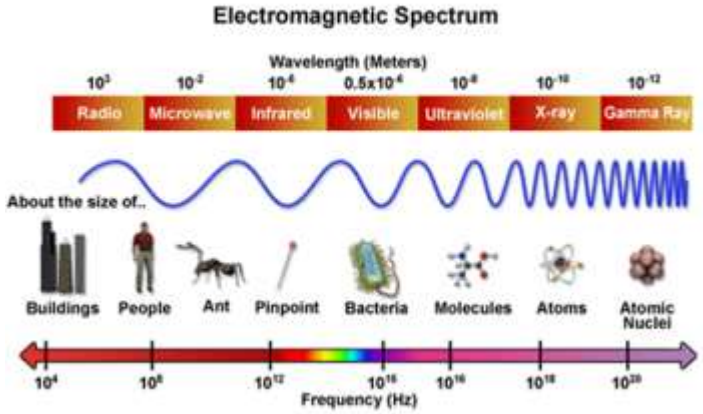

Figure 1.13 Electromagnetic spectrum. All radiation frequencies above ultraviolet are ionizing due to their higher energy [115]. The figure is courtesy of https://sites.duke.edu/missiontomars/the-mission/radiation/what-is-radiation/

Alpha particles are charged particles; they have very limited penetration ability and a sheet of paper can block them. Beta particles are similar to electrons (lighter than alpha). They can travel a few feet in the air and they can penetrate the skin, but plastic or a woodblock can stop them. Neutron, gamma, and x-rays can penetrate much deeper and can ionize the material making them radioactive. Electronics and living things require more careful shielding from this radiation [116].

In electronic circuits, radiation can cause bit or state flip (in the case of a single radiation event) or total ionization. The total ionizing dose (TID) depends on the exposure dose and time, as it is an accumulating effect. The ionizing dose can be a cause of leakage current or can destroy the transistors completely because it can generate an excess number of $e^{-}h^{+}$ pairs [17], [117]. Tungsten and lead shielding is an effective way to shield the

circuits from radiation but it makes the design, installation, and replacement a complex and expensive task. Memristors are being studied as strong candidates for radiation prone applications due to their tolerance of higher total ionizing doses and displacement damage from radiation. Phase change and oxide-based memristors like TiO_2, TiO_x, and HfO_2 devices are studied for radiation tolerance [118], [119].

1.6 Summary

This chapter explained the motivation behind the following research work and discussed the literature and background needed to understand the presented material. Major work in this dissertation is based on neural networks, thus, software and artificial neural networks are compared for their advantages and disadvantages. This dissertation uses pulse shaping to mimic the synaptic spike-timing-dependent plasticity (STDP) rule that facilitates the spatio-temporal pattern recognition (STPR) in the memristors-based spiking neural networks. Thus, the chapter also talked about the different potential electronic candidates used in literature to mimic synaptic behavior. Since this dissertation uses a memristor as the potential candidate to mimic synaptic mechanisms in a hardware-based neural network, thus, the working mechanisms of different kinds of memristors with their properties were also reviewed.

1.6.1 Research Summary

In this research, memristor-based spiking neural networks are designed to learn spatio-temporal patterns representing 25 and 100-pixel characters. Two-terminal resistive memory devices (memristors) are used as synapses to manipulate conductivity paths in the network. Spike-timing-dependent plasticity (STDP) learning behavior results in pattern learning and is achieved using biphasic pre- and post-synaptic spikes. A TiO_2 based non-

linear drift model designed in Verilog-A is used to implement memristor behavior and is modified to include experimentally observed state-altering and ionizing radiation effects on the device. Effects of state-altering radiation on the STDP learning rule, system stability, and pattern learning ability of the spiking neural network are observed.

Radiation events distort the spike-timing-dependent plasticity (STDP) learning curve undesirably, making the connection between afferents stronger by increasing the conductance of synapses overall. At lower flux, the network can recover and relearn the pattern. As the radiation flux increases, it can overwhelm the leaky integrate-and-fire (LIF) post-synaptic neuron circuit and make the network less stable. In the absence of patterns, the radiation effects accumulate in the system and the network never regains stability.

The impact of neuron "death" (disabled neuron circuits) due to radiation is also examined. Neuron-death simulation results emphasize the importance of non-participating neurons during the learning process, concluding that non-participating afferents contribute to improving the learning ability of the neural network. Instantaneous neuron death proves to be more detrimental for the network compared to when the afferents die over time thus, retaining the network's pattern learning capability.

1.6.2 Overview of the Dissertation

Chapter 2 discusses the TiO_2 memristor device model in detail, as this is the model used throughout the dissertation for the neural network simulations. The non-linear window is discussed in detail and explains the non-linearity achieved in the model to mimic the actual device behavior. The behavioral model is designed in Verilog-A and the simulations representing the model behavior are also presented. This chapter also discusses the three-terminal intercalated ion devices mentioned in Section 0. The behavior is modeled

including both drift and diffusion characteristics of the device and the resulting simulations are presented. Model verification characteristics are published in [120].

Chapter 3 discusses the experimental studies of the effects of radiation on various memristive devices. In literature, radiation is prominently observed to alter the given state of the memristive device, generate ionizing current in the circuit, or change the off-resistance of the memristive device. The three experimental observations are discussed in detail in this chapter. The chapter also discusses the modifications made in the behavior of the memristor model to include all three effects of radiation. Later in the chapter, the designed model is simulated to verified designed behavior with the given experimental results. The contributions from this chapters are published in [120].

In Chapter 4, the design and topology of the different neural networks used in the dissertation are laid out. This chapter talks about the design of the post-synaptic neuron, which is a leaky integrate-and-fire neuron that generates the desired biphasic spike when a certain threshold is reached. The post-synaptic spike aids synaptic memristors in realizing STDP and helps the neural network in spatio-temporal pattern learning. The chapter continues with the simulating pair-based STDP and discusses the factors that affect the shape of the STDP learning curve. The factors that are observed to affect STDP are the initial state and threshold of the memristive device and the shape and pulse width of the pre- and post-synaptic afferent. A later section of the chapter discusses the spatio-temporal pattern learning behavior of the neural network and the related simulations. The contributions from this chapters are published in [120], [121].

Chapter 5 analyzes the effect of radiation on the spatio-temporal pattern learning ability of the memristor-based spiking neural network. The radiation effects discussed in

Chapter 3 are simulated on the neural network discussed in Chapter 4. The chapter starts with analyzing the effects of radiation on the spike-timing-dependent plasticity (STDP) curve by observing the changes in the learning rule. A pulsed neural network is used to simulate the cumulative effects of the long-term radiation on the network in the absence of the pattern. Later parts of the chapter analyze the effect of radiation on the spiking neural network when subjected to short-term radiation under varying flux for varying durations of time. The chapter also discusses the changes in network behavior when it is learning in the presence of constant radiation. Changes in network stability are also statistically analyzed. The contributions from this chapters are published in [120]–[122] and are under journal review.

Chapter 6 discusses the effects of neuron death on the learning behavior of the neural network. The chapter discusses the design and topology of the network used to simulate the neuron death in the spiking neural network. Later in the chapter, the simulated results are analyzed to compare the pattern learning ability of the network in case of instantaneous neuron death (due to radiation flare or strong radiation event) and gradual neuron death (in case of low but continuous radiation events, like in war zones, or post-nuclear accident sites). The contributions from this chapter are in process for publication.

Lastly, the implications of radiation effects and neuron death results are discussed in Chapter 7. This chapter also talks about the prospects of the work presented in this dissertation.

CHAPTER 2: RESISTIVE MEMORY MODELING

The literature shows that extensive effort has been made to physically implement memristors, but significant progress has been made in modeling these devices as well [64], [123]–[136]. Modeling not only helps better understand the working principles and the performance of the device but also facilitates the simulation of the devices in larger and more complicated circuits. The presently available models in the literature can be categorized into either physical or mathematical models. The mathematical SPICE models like TEAM [124], Simmons Tunneling [126], and Yakopcic [125] have a minimal (if any) physical explanation for the relatively large number of input parameters used (up to 13). The mathematical models have many parameters to choose from and represent their respective device characteristics very closely, but their accuracy is limited. It is thus difficult to use pulse shaping reliably because the input parameters need to be modified for each given shape and frequency of the input [125], [126], [137]. On the other hand, most of the physical memristor models presented in literature depend on the ionic drift behavior for TiO_2 memristive devices presented by Strukov et al. [64]. This chapter discusses and presents the simulation results of the TiO_2 based non-linear ionic drift memristor model and the intercalated-ion memristor model. The intercalated-ion memristor model is based on a three-terminal low-power, electrochemically tunable graphene synaptic device revealed recently, in 2018 [109]. TiO_2 based model verification characteristics are published in [120].

2.1 Memristor Models

Many models are studied in the literature, the most explored ones are the linear ion drift model by Strukov et al. [64], the non-linear ion drift model by Laiho et al. [33], the Simmon tunneling barrier model by Pickett [127], the Yakopcic model by Yakopcic et al. [138] and the TEAM model by Kvatinsky et al. [124]. Both the linear and the nonlinear drift models are based on the theory that memristors are represented by a circuit with two resistors, the high resistance coming from the non-conductive (oxide) region and the low resistance from the conductive region, discussed in detail in Section 0. The Laiho et al.'s non-linear drift model assumes non-linear dependencies between the voltage and the state variable ($\frac{w}{D}$), which is a normalized parameter. The Simmons model assumes that the ions in the devices present exponential dependence, thus the model has exponential and symmetric switching behavior between the current and the state variable. The TEAM model assumes the polynomial dependence between the memristor current and the state variable. Other models are also presented in the literature for SDC devices [106], where an empirical compact model is used to match the SDC device I-V characteristics [139].

This work uses a TiO_2 based ionic drift memristor model, which is discussed in Section 0. The model simulations are a close representation of oxide-based device characteristics at multiple frequencies, pulse shapes, and sizes. Another reason this model is chosen is because multiple radiation studies have already been performed on TiO_2 memristive devices [118], [140], [141]. The model is also voltage controlled, has an explicit I-V relationship, includes non-linearity, has a normalized state variable ($\frac{w}{D}$), and the model is not purely mathematical. The model has lower accuracy but has been widely

used in simulations and comparison studies like Chua et al. for designing memristor bridge synapse base neural networks and by other references [10], [125], [142]–[145].

The memristor models are accompanied by a window function that is used to add non-linearity to the model, which is specific to the device. The window function also forces the physical boundary ($0 \leq \frac{w}{D} \leq 1$) of the device in the model. Multiple window functions compatible with the ion-drift model are used in the literature by Joglekar and Wolf [66], Biolek et al. [146], Prodromakis et al. [145], and piecewise by Yu at al. [147]. All of the window functions can induce non-linear drift in the model and can only provide symmetrical window functions (except the piecewise function which could induce asymmetry). Symmetrical Joglekar and asymmetrical modified piecewise window functions are shown in Figure 2.1.

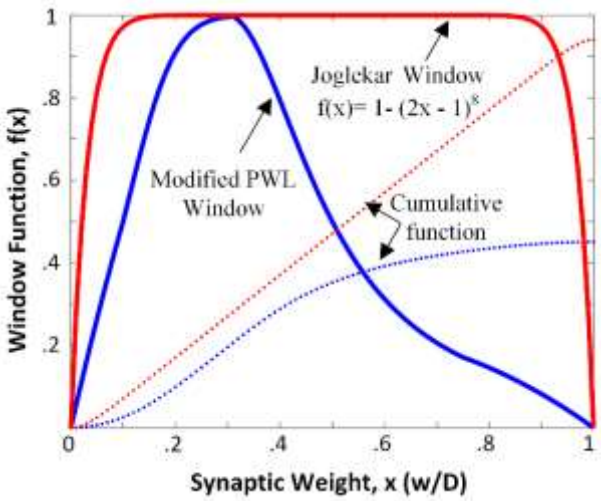

Figure 2.1 The evolution of a window function (f(x)) with normalized synaptic weight ($\frac{w}{D}$) is plotted. The symmetric Joglekar window function shows the sharp change near the boundary conditions, thus limiting the physical boundary of the device such that $0 \leq w \leq D$. Asymmetrical modified PWL function shows the asymmetry of the function. PWL does not end sharply as $\frac{w}{D}$ reaches one but still limits the physical boundary of the function as $0 \leq w \leq D$.

2.2 The TiO_2 Memristor Model

The TiO_2 based non-linear ionic drift memristor model was proposed by Strukov et al. in 2008 [64]. Since then, the model has been widely adopted in the literature, and has been used extensively in simulations and comparison studies, like Chua et al., for designing memristor bridge synapse base neural networks [10], [125], [142]–[145].

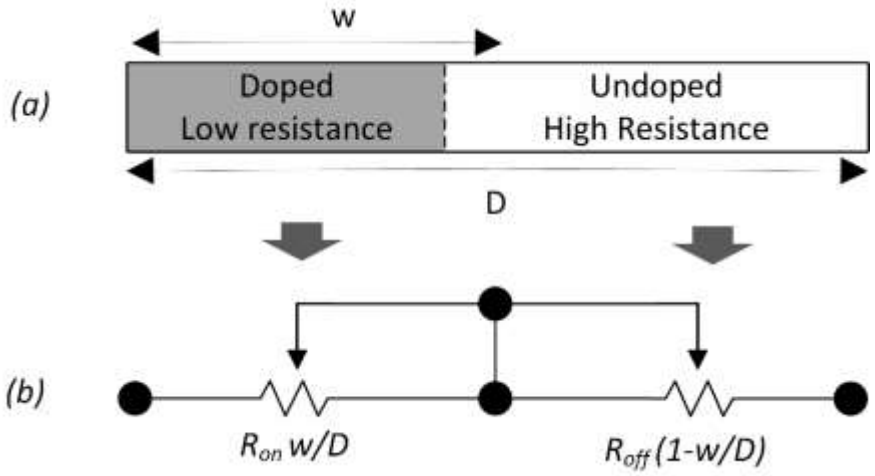

Figure 2.2 Representation of a memristor as suggested by Strukov. (a) Memristive device of thickness "D" represented as a combination of doped (low resistance) and undoped (high resistance) regions. (b) Circuit representation of two variable resistors, the total device resistance is R_{on} when $\frac{w}{D}=1$, and R_{off} when $\frac{w}{D}=0$ [64]. Reprinted by permission from Macmillan Publishers Ltd: Nature, [64], copyright (2008)

The ionic drift model effectively treats the instantaneous total resistance of a memristive device R_{mem} as two variable resistors connected in series, as represented in Figure 2.2 (a). One of these resistors represents a conductive region of thickness w inside a device with physical thickness D. The other resistor corresponds to a less conductive region of thickness D−w. When w is almost equal to the device thickness, D, the device is in its lowest resistance state, with the resistance value R_{mem} equal to R_{on}. The device is in

a high resistance state, with R_{mem} equal to R_{off}, when w is much less than the total device thickness D.

The total resistance of this memristive device is called the memristance (R_{mem}) and has units of Ohms. The I-V relationship of the two variable resistance system represented in Figure 2.2 (b) can be given by Ohm's Law, where R_{mem} is a state-dependent resistance. Thus, the memristance can be written mathematically as:

$$R_{mem} = R_{on}\frac{w}{D} + R_{off}\left(1 - \frac{w}{D}\right) = R_{off} - (R_{off} - R_{on})\frac{w}{D} \tag{2.1}$$

From Equation (2.1) at $w \approx D$, the $R_{mem} \approx R_{on}$ (low resistance state) and at $w \approx 0$, the $R_{mem} \approx R_{off}$ (high resistance state). The ratio $\frac{w}{D}$ is referred to as the state variable of the device and is physically bounded $0 < \frac{w}{D} < 1$, 0 being the more resistive state and 1 being the more conductive state. Change in the state variable is a function of time and depends on the mobility of dopant ions (μ) drifting under a uniformly applied electric field as:

$$\frac{dw}{dt} = \frac{R_{on}\,\mu}{D} I_{mem} \tag{2.2}$$

In Equation (2.2), $\frac{R_{on}}{D} I_{mem}$, is the electric field in the conductive region of length w. The equivalent circuit, as suggested by Biolek et al. [146], is represented in Figure 2.3 (a) and consists of dependent voltage source E_{mem} and resistance R_{off} in series. Thus, the circuit equation is:

$$V_{mem} = R_{mem} I_{mem} = R_{off} I_{mem} + E_{mem} \tag{2.3}$$

Comparing Equation (2.1) and Equation (2.3):

$$E_{mem} = -I_{mem}(R_{off} - R_{on})\frac{w}{D} \tag{2.4}$$

Equation (2.4) shows that E_{mem} is a dependent voltage source that is controlled by the state variable ($\frac{w}{D}$) of the device (from the auxiliary circuit in Figure 2.3 (b)) and, current (I_{mem}) at a given time.

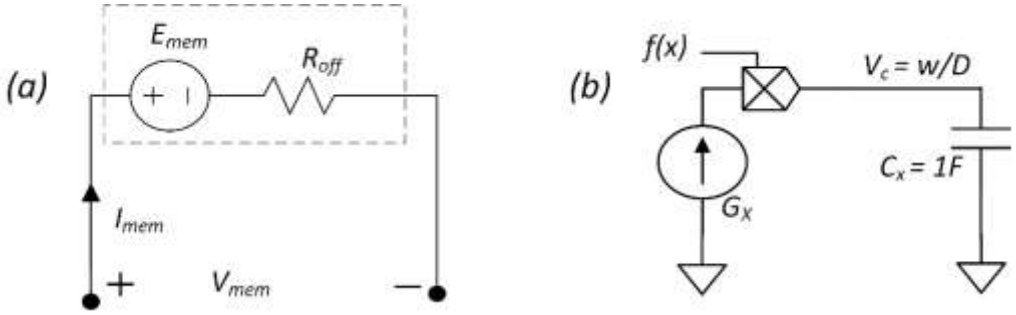

Figure 2.3 Schematic representation of the memristor model as suggested by Biolek [146]. (a) Implementation of the memristive circuit with dependent source E_{mem} and resistance R_{off}. (b) Auxiliary circuit with I_{mem} dependent current source G_x and 1 F capacitor C_x. The voltage across C_x controls E_{mem}. The figure is adapted from an article published under the Create Commons license, https://www.radioeng.cz/fulltexts/2009/09_02_210_214.pdf.

The auxiliary circuit, shown in Figure 2.3 (b), which sources E_{mem}, contains a dependent current source, G_x, connected to a large 1 F capacitor (C_x). The voltage across the capacitor, C_x, feeds the E_{mem} in the memristor circuit shown in Figure 2.3 (a). I_{mem} drives the current source (G_x) as:

$$G_x = \frac{R_{on}\,\mu\,I_{mem}}{D^2} \tag{2.5}$$

Thus, using the relation $I = C\,\frac{dV}{dt}$ we get,

$$\frac{dV_c}{dt} = G_x\,f(x), \qquad \text{if } 0 < \frac{w}{D} < 1,\ f(x) = 1 \quad \text{else, } f(x) = 0 \tag{2.6}$$

Where f(x) is the window function, explained in the next section.

2.2.1 Non-Linear Window Function

The ionic drift model does not address the non-linearity observed in many physical memristive devices, making it useful for very limited applications. However, non-linearity can be introduced in the device by using an appropriate non-linear window function, f(x).

In Figure 2.3 (b), the current source is multiplied by the window function, f(x). This window function handles the non-linear dopant drift in w when it is near the physical boundaries, which occur when $\frac{w}{D} \approx 0$ or $\frac{w}{D} \approx 1$. It also helps keep $\frac{w}{D}$ bounded in the appropriate range between 0 and 1. The window function used in this work is from Joglekar and Wolf [66] and is given as:

$$f(x) = 1 - (2x - 1)^8 \tag{2.7}$$

Thus, using the relation, $I = C\,\frac{dV}{dt}$, we get:

$$\frac{dV_c}{dt} = G_x\, f(x) \tag{2.8}$$

The window function in Equation (2.7) is symmetric about zero voltage, but different window functions can be used, that change depending on the polarity of the applied voltage, to model asymmetry in the I-V characteristics [125]. Other parameters used in the model are R_{on} = 10 kΩ, R_{off} = 100 kΩ (when not changing due to radiation), $\mu = 10\ fm^2/V$ and D = 10 nm, to mimic the characteristics of the HP Labs memristor as estimated in [146].

2.2.2 Simulation Results for the Memristor Model

The memristor behavioral model is implemented in Verilog-A (APPENDIX A) and the simulations are done using Cadence Virtuoso Spectre. The simulated current versus

voltage characteristics of the model results are shown in Figure 2.4 (a). The plot displays all of the three characteristic fingerprints of a memristor [57], [60], [65]. The hysteresis curve is pinched at the center, the area of the hysteresis is decreasing with increasing frequency, and finally, it ends in a straight line at higher frequencies of 100 Hz and 1 kHz. These results demonstrate the same results from the ionic memristor model with window function represented by Equation (2.7). In this case, the memristor model has no threshold, thus, even at smaller voltages, the device forces the change in the conductivity as observed in Figure 2.4 (a).

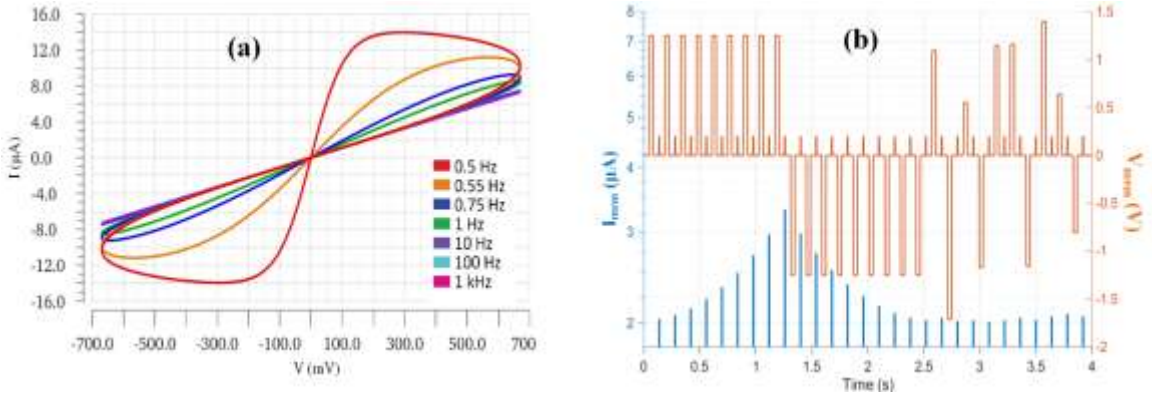

Figure 2.4 (a) I-V characteristics of the memristor model used in the study. (b) The current and voltage plot in time shows the increase in I_{mem} as a train of a positive pulse is applied across the device. Similarly, the resistance increases, and the current decreases as a train of negative pulses is applied. Only the current measurements during the read cycle are presented here for clarity.

The change in the memristor current I_{mem} with applied voltage V_{mem} is plotted in Figure 2.4 (b), where V_{mem} is a train of write (1.25 V) and read (0.2 V) pulses followed with erase (−1.25 V) and read (0.2 V) pulses followed again with random voltage write/erase and read pulses starting at 2.5 s. The positive voltage pulses increase I_{mem} due to decreases in memristance. On the other hand, the negative voltage pulses lead to a decrease in the current flowing through the device, due to an increase in the memristance.

The random pulses show similar behavior in proportion. Figure 2.4 shows the gradual and controlled change in the state of the device. Similar experimental results are reported in [106].

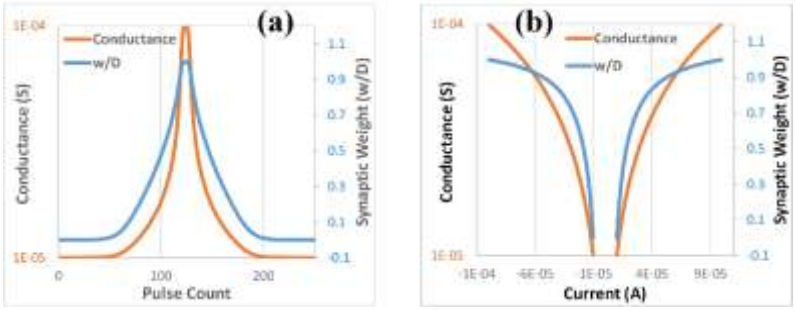

Figure 2.5 The memristor device shows a non-linear change in conductance and synaptic weight ($\frac{w}{D}$) when a train of 125 +1 V pulses followed with 125 −1 V pulses are applied (Pulse Width = 0.9 ms, Pulse Period = 1 ms). (a) Conductance and $\frac{w}{D}$ versus pulse count plot. (b) Conductance and $\frac{w}{D}$ versus device current plot.

Figure 2.5 shows the electrical characteristics of the memristor model when the threshold voltage of 0.6 V is included in the behavioral model. To analyze the non-linearity in the device, a train of 125 +1 V pulses followed with 125 −1 V pulses, are applied with a pulse period of 1 ms and a pulse width of 0.9 ms. Figure 2.5 (a) and (b) plot the conductivity and synaptic weight ($\frac{w}{D}$) of the memristor versus the pulse count and device current, respectively. Non-linearity is obvious in Figure 2.5 (a) when the device reaches the off-state (lowest conductivity) and the slight change in the linearity of $\frac{w}{D}$ is also present as the device reaches the on-state (highest conductivity). A similar pattern can be observed in Figure 2.5 (b) where a logarithmic change in conductance vs current is almost linear, representing a logarithmic change in conductance with the device current.

Figure 2.6 (a) and (b) show the I-V characteristics of the device when a 0.6 V sinusoidal and triangular periodic voltage is applied to the memristive device at the varying

frequencies (respectively). At a higher device threshold of 0.5 V in Figure 2.6 (b), the memristor could not change the state completely as the frequency increases. In Figure 2.6 (a), at a lower threshold of 0.25 V, the device switches state completely before reaching the threshold at higher frequencies. Figure 2.6 (a) and (b) also show the stability of the model at different resistance states. Note that the I-V curve displays a pinched hysteresis loop and that the hysteresis lobe area decreases as the input frequency increases, finally reducing to a line at a higher frequency. These are necessary characteristics of the I-V curve of a memristive device [63]. Model verification characteristics are published in [120].

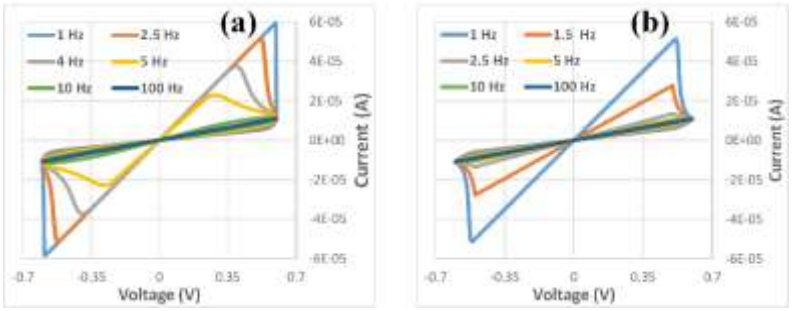

Figure 2.6 The I-V characteristics of the memristor as (a) 0.6 V sine input is applied with 0.25 V threshold and (b) 0.6 V triangle input applied with a 0.5 V threshold, showing the characteristic decrease in the pinched hysteresis lobe area as the frequency increases.

2.3 Intercalated-Ion Model

Section 0 discussed the organic polymer and intercalated-ion memristive devices published recently, in 2018. In the three-terminal memristive devices [109], [148], when current is applied at the reference electrode as shown in Figure 2.7 (b) and (c), Li-ions drift towards the graphene and get intercalated in the graphene structure. The intercalated Li-ions make the graphene layer more conductive, similar to a synapse as shown in Figure 2.7 (a). Over time, Li-ions intercalated in the graphene structure start to diffuse exponentially

out of the graphene layer, depending upon the length and width of the graphene synapse. This characteristic is similar to biological synapse.

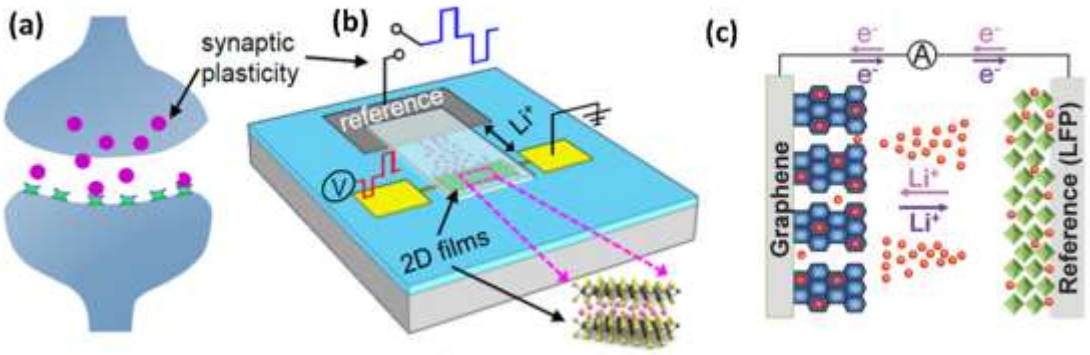

Figure 2.7 The graphene intercalated Li-ion memristive device structure. (a) Schematic of biologic synapse compared with (b) schematic of the graphene synapse, where applying current at the reference electrode changes the synaptic weight. Pink arrows zoom into the illustration of the intercalated Li ions into graphene. (c) Blue arrow indicates the de-intercalation of Li-ion out of graphene and pink shows intercalation of Li ions moving into graphene [109]. © 2018 Wiley. Used with permission from Mohammad Taghi Sharbati, Yanhao Du, Jorge Torres, Nolan D. Ardolino, Minhee Yun, and Feng Xiong, Low- Power, "Electrochemically Tunable Graphene Synapses for Neuromorphic Computing", Advanced Materials, John Wiley and Sons.

2.3.1 Experimental Results

Figure 2.8 shows the published experimental results obtained from the graphene intercalated Li-ion device from Sharbati et al. [109]. Figure 2.8 (a) and (b) represents the synaptic behavior of the device. In Figure 2.8 (a), a 50 pA current pulse is applied at the reference electrode for 10 ms to potentiate the device. This drifted the Li-ions into the graphene, resulting in a 30 Ω decrease in resistance, but diffusion recovered 20 Ω, and the resulting change was -10 Ω. In Figure 2.8 (b) a depressive −50 pA current pulse is applied at the reference electrode for 10 ms, showing similar characteristics for drift and diffusion resulting in the 10 Ω gain in resistance. Figure 2.8 (c) shows the change in conductance of the device as repeated sets of 250 positive pulses followed by 250 negative pulses, are

applied at a higher frequency. The resistance of the device subsequently swings between 880 Ω (1136 μS) and 7.78 kΩ (128 μS).

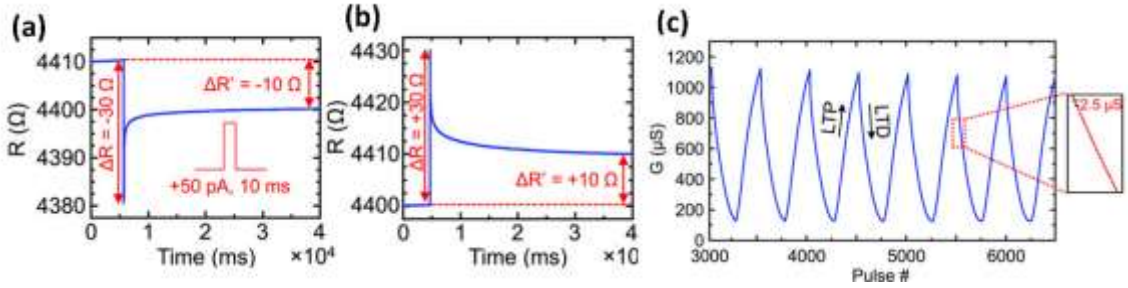

Figure 2.8 Synaptic behavior of the device. (a) potentiation, (b) depression (c) change in conductance [109]. © 2018 Wiley. Used with permission from Mohammad Taghi Sharbati, Yanhao Du, Jorge Torres, Nolan D. Ardolino, Minhee Yun, and Feng Xiong, Low- Power, "Electrochemically Tunable Graphene Synapses for Neuromorphic Computing", Advanced Materials, John Wiley and Sons.

2.3.2 Model Design

The memristor model is implemented in Cadence Virtuoso using Verilog-A (APPENDIX B), shown as the greyed-out part of Figure 2.9. The model for the graphene intercalated Li-ion devices is designed while keeping in mind that at any given time the resistance of the device depends on the number of Li ions intercalated in the graphene layer. The number of Li ions intercalated in the graphene layer depends on the drift and diffusion occurring in the device over time. Thus, the resistance of the device at any given time is the sum of the drift resistance (R_{drift}) and the diffusion resistance (R_{diff}) as shown in the schematic in Figure 2.9 and is given by the equation:

$$R_{mem} = R_{drift} + R_{diff} \tag{2.9}$$

2.3.3.1 Drift

Li-ions present in the device drift towards (away) from the graphene when a current pulse is applied at the reference electrode. For every electron (e^-) flowing into (out) of the

graphene in the external circuit in Figure 2.7 (c), a corresponding Li-ion enters (leaves) the graphene through the electrolyte. Thus, the charge transferred into/out of the graphene will depend on the magnitude and length of the current pulse on the reference electrode (Q = I*t). At any given point, the voltage across a 1 F capacitor is equal to the charge on it (Q = CV and if C = 1 F, Q = V). The voltage across a 1 F capacitor will be V_{drift} and reflect the amount of charge transferred by a reference electrode current pulse. Thus, V_{drift} will be the voltage drop across the variable resistor R_{drift}, as represented in the model schematic in Figure 2.9.

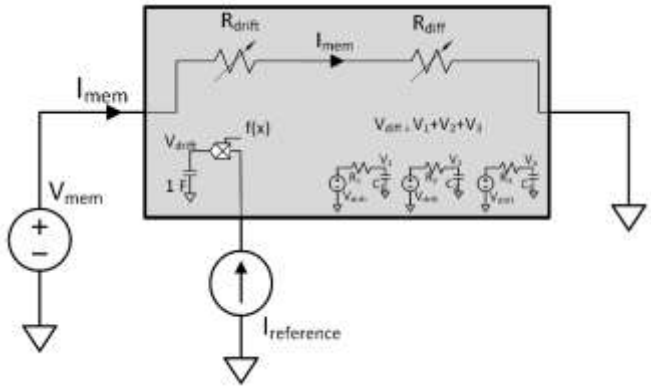

Figure 2.9 Schematic representation of the model developed for graphene intercalated Li-ion devices. The auxiliary circuit connected to the reference electrode current source controls drift resistance (R_{drift}). Three RC delay circuits controlled by V_{drift} modify the diffusion resistance (R_{diff}).

2.3.3.2 Diffusion

Diffusion starts right after the input reference pulse or as the drift ends. Diffusion in the device was observed to be exponential and was speculated to depend on three factors: the width of the graphene synapse, the length of the graphene synapse, and the diffusion process from the reference electrode to the graphene [109]. Thus, three independent RC delay circuits represent the diffusion voltage (V_{diff}) and control the diffusion resistance

(R_{diff}), as presented by the model schematic in Figure 2.9. The diffusion was modeled such that the device will see the change in conductance due to diffusion for 1.5 s after the last drift.

2.3.3 Simulation Results

The Spectre transient simulation tool was used in Cadence to generate all the following waveforms. The simulated synaptic behavior from the designed model is presented in Figure 2.10. Figure 2.10 (a) shows that the input depression (−50 pA) and potentiation (50 pA) current pulse are applied at the reference electrode for 10 ms at an interval of 2 s. Figure 2.10 (b) shows the resulting change in the resistance of the device over time due to both drift and diffusion. Drift resulted in a ∓30 Ω change in resistance, but diffusion recovered ∓20 Ω, and the resulting change was ∓10 Ω respectively. Figure 2.10 (c) and (d) show the zoomed-in depression and potentiation pulse resulting in an instantaneous increase and decrease in resistance due to drift. The simulation results are very similar to the actual device characteristics, as represented in Figure 2.8 (a) and (b).

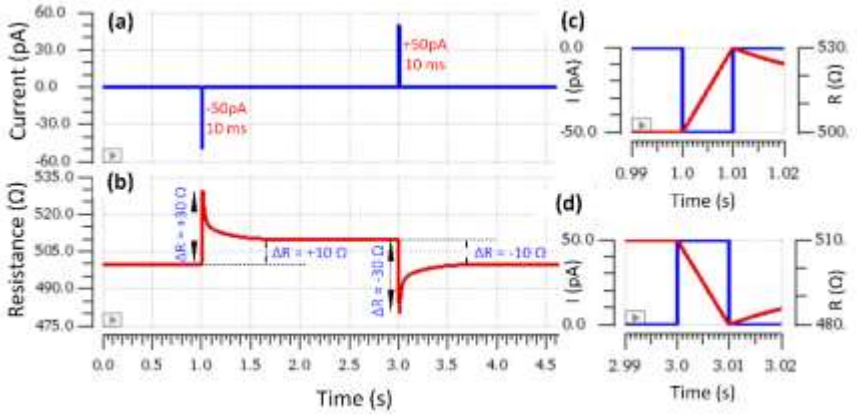

Figure 2.10 Synaptic behavior (a) depression and potentiation current pulse (b) drift resulted in ∓30 Ω change in resistance but diffusion recovered ∓20 Ω. (c) Potentiation pulse resulting in an instantaneous decrease in resistance due to drift (d) Depression pulse resulting in an instantaneous increase of resistance due to drift.

The model was further verified by the simulation represented in Figure 2.11. For this simulation, the reference current pulses of ±50 pA and10 ms duration were applied at a frequency of 74 Hz. A pulse train of 250 positive pulses followed by 250 negative pulses was repeated for 3,500 pulses and the resulting resistance vs pulse count plot is presented in Figure 2.11. Similar to the experimental data, the conductance of the device swings between 1,136 μS (880 Ω) and 128 μS (7.78 kΩ), but the model is missing the change in slope that happens in the device resistance as it reaches closer to maximum or minimum resistance. The simulated model has symmetrical depression and potentiation, whereas that is not the case with the experimental data. These effects are still under study and will be added to the model in the future when more experimental data is available.

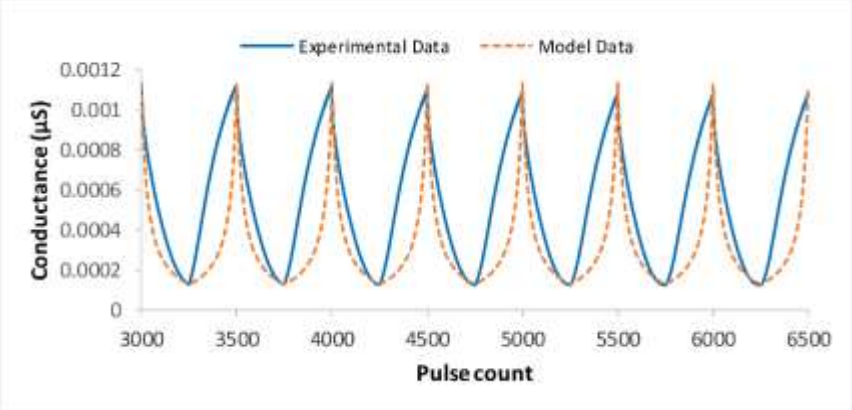

Figure 2.11 Behavior of the experimental device and the designed model as a pulse train of 250 positive pulses followed by 250 negative pulses is repeated for 3500 pulses. Similar to the experimental data, the conductance of the device swings between 1136 μS (880 Ω) and 128 μS (7.78 kΩ). © 2018 Wiley. Used with permission from Mohammad Taghi Sharbati, Yanhao Du, Jorge Torres, Nolan D. Ardolino, Minhee Yun, and Feng Xiong, Low- Power, "Electrochemically Tunable Graphene Synapses for Neuromorphic Computing", Advanced Materials, John Wiley and Sons.

2.4 Conclusion

The academic literature presents a wide range of memristor models [124], [126], [138], many of which are still under development. Some of the models are more

mathematical, with many parameters to choose from, making them input and application limited. This dissertation uses the non-linear drift model, which is motivated by TiO_2 memristive devices, and is also used in multiple studies, including Chua et al. in their memristor bridge synapses [9], [10]. A window function is used to implement non-linearity in the model. This model captures the non-linearity presented by memristive devices, while still using the physical characteristics of the device. The exact model parameters used, the simulated characteristics and the nonlinearities observed in the model were laid out in detail in this chapter.

The intercalated-ion model was also discussed in this chapter. It is a physical model based on the organic polymer and intercalated-ion three-terminal memristive devices published recently in 2018 [109]. Due to the lack of the availability of the detailed experimental results, the model was not extremely well calibrated but does serve as a starting point. It is not used in the remainder of the dissertation, but possibly will be used for future collaborative research.

CHAPTER 3: RADIATION EFFECTS ON A MEMRISTOR

It is important to model the effects of radiation on the memristive devices to understand the response of systems deployed in harsh environments, such as those experienced during certain military and space missions. Further, smaller dimensions change the way radiation interacts with devices, often making them more susceptible to radiation events [17]. In this chapter, Section 0 discusses the effects of various types of radiation on different types of oxide-based memristive devices with different active materials and structures. Section 3.2 shows the design of the model developed that is added to the memristor model discussed in Section 0 and used in this dissertation. The contributions from this chapter are published in [120].

3.1 Experimental Results of Radiation on Memristors

Multiple studies have experimentally examined the radiation effects on oxide-based memristive devices. Reference [141] discusses the effects of proton and neutron radiation on TiO_2 memristive devices. No significant changes in the device characteristics were observed when exposed to $3x10^{14}$ 14.1-MeV neutrons/cm^2. On the other hand, $7.75x10^{16}$ 350-keV proton/cm^2 irradiation is estimated to induce 1.7% additional vacancies in TiO_2 leading to an increase in conductivity of the device in the off-state [141]. A similar conclusion is drawn in [149] post proton exposure of their TiO_2 memristive devices.

Another experimental study on TiO_2 memristive devices in [118] observes the significant change in the on-state of the device post alpha radiation (10^{14} 1-MeV alphas/cm^2) although other kinds of irradiation events did not affect the device on-state.

Gamma, neutron, and bismuth ion radiation did not affect the off-state of the device, but when exposed to protons and alpha particles the device conductivity increased as noted in Figure 3.1 (a) [118].

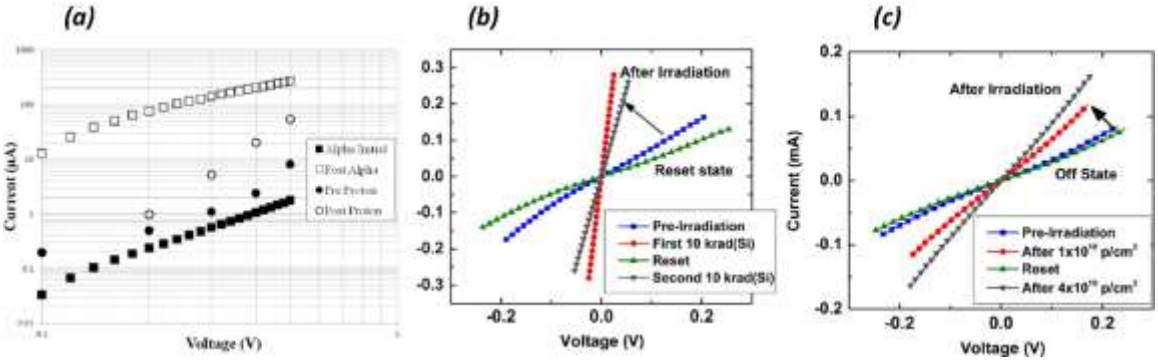

Figure 3.1 State change in oxide-based memristive devices due to radiation events. (a) comparing pre and post alpha and proton irradiation, alpha radiation (10^{15} cm^{-2} 1-MeV) changes the TiO_2 device state more than proton radiation [118], © 2013, IEEE. (b) X-ray irradiation changed the state of the TaO_x device, making it more conductive. (c) Proton irradiation affects the TaO_x device similarly and changes the device state to more conductive [150]. © 2012, IEEE.

The effects of radiation on the electrical characteristics of TaO_x memristive memories are experimentally assessed in [150]. Switching from high resistance to low resistance and complete failure of a few devices due to a cumulative dose of 10 keV x-ray irradiation is experimentally observed, plotted in Figure 3.1 (b). Reference [150] also shows that a 220 ^{60}Co gamma radiation source radiating at a dose rate of 53 rad(Si)/s did not affect the TaO_x device samples. A 4.5 MeV protons source up to a dose of 5 Mrad(Si) did not affect the state of the devices, but when irradiated with protons of energy 105 MeV, the off-state resistance of the devices generally decreased with increasing proton fluence, indicating cumulative device degradation, as plotted in Figure 3.1 (c). 800 keV Si ions bombardment created oxygen vacancies in the device, which lead to reduced resistance similar to the results observed in TiO_2 devices in [150].

Proton-based total-dose irradiation effects on Cu-doped-HfO_2-based resistive-random-access-memory (ReRAM) devices are experimentally studied in [151]. Results show positive shifts in the set, reset and on-resistance after proton irradiation, possibly due to induced electron trap changes in the HfO_2 layer. The effects are observed to enhance almost linearly when the dose increases from 1.5 to 3 to 5 Giga-rad[Si] at a constant dose rate of 237 ± 1.8 krad[Si]/s. Proton irradiation also decreased the off-resistance of the device, by creating more defects and thus increasing the device leakage current [151].

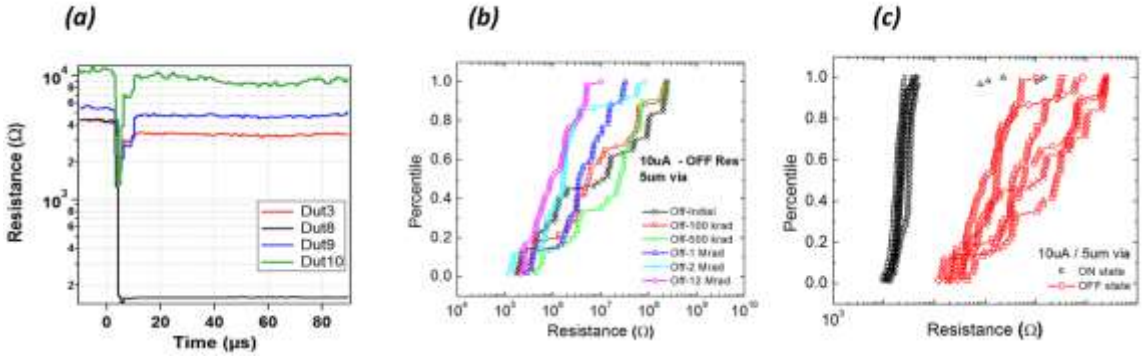

Figure 3.2 Off-resistance change in memristive device post-radiation exposure. (a) All four TaO_x devices under test saw the decrease in R_{off} post-irradiation with DUT 10 being affected the most, from [152] at the dose rate of rad (Si)/s and a pulse width of 500 ns. © 2014, IEEE. (b) Plots the decreasing R_{off} with increasing radiation dose (c) Comparing R_{on} and R_{off} change due to radiation. Radiation does not affect on-resistance as much it changes off-resistance. Plots (b) and (c) from [153] saw electron radiation with 10 µA programming current. © 2014, IEEE.

Reference [152] also experimentally investigates the effects of high dose rate ionizing radiation and total ionizing dose on TaO_x memristors. Data shows that the dose rate of $1x10^8$ rad(Si)/s, with a radiation pulse width of 1 µs, did not affect the off-resistance of the device. On the other hand, when exposed to a higher dose rate of $4.3x10^8$ rad(Si)/s for 500 ns, the off-resistance of the devices decreased as plotted in Figure 3.2 (a) [152]. In the case of X-ray irradiation (dose rate of $4.3x10^8$ rad(Si)/s), the lack of a discharge path due to the floating terminal setup leads to a decrease in the off-resistance of the device

(pointing to circuit setup dependencies) [152]. Paper [152] also uses a ^{60}Co proton source to evaluate total ionizing dose-response, the state change was observed at the dose rate of $4x10^8$ rad(Si)/s but not at $1x10^8$ rad(Si)/s. The study indicates that the irradiation response was dependent on the irradiation conditions, bias configuration, and varied from device to device [152].

The impact of the proton, gamma, and alpha irradiation on the retention and endurance of Ag filament-based resistive RAMs (with amorphous $Ge_{30}Se_{70}$ (photo doped with silver) as an active layer) is experimentally studied in [153]. It is noted that devices were able to retain their states until 2.8 Mrad of gamma radiation from ^{60}Co. Figure 3.2 (b) and (c) show the cumulative distribution of on- and off-resistance of the devices post 100 keV electron exposure. On-resistance does not seem to vary with irradiation (Figure 3.2 (c)) but off-resistance decreases as the total ionizing dose become higher than 1000 krad (Figure 3.2 (b)). This characteristic was noticed in all the cases when the device was programmed at 10 μA, 50 μA, and 100 μA pre-exposure [153].

Figure 3.3 shows the cumulative distribution gathered from the same $Ge_{30}Se_{70}$ ReRAMs devices when exposed to a 50 MeV proton irradiation from the front and the backside of the device [153]. On-resistance remained mostly unaffected in both cases of front and back exposure, Figure 3.3 (a) and (b). Off-resistance seems to be affected more strongly when the device is proton irradiated from the backside, Figure 3.3 (a) and (b) [153]. The exposed from the back protons move through the Si, SiO_2, and Ni layers before interacting with the active $Ge_{30}Se_{70}$ active layer, which may result in displacement and ionization damage in the layers due to recoiled nuclei on the way. On the other hand, during

the front exposure, the protons are incident directly on the active layer, passing through it with minimal interaction [153].

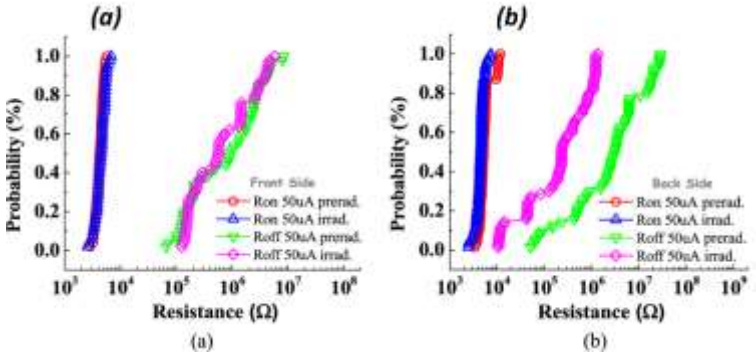

Figure 3.3 Irradiation direction affecting the impact of proton irradiation on the memristive device. Cumulative probabilities of HRS and LRS states of Ag-$Ge_{30}Se_{70}$ RRAMs exposed to 50 MeV protons. (a) Devices irradiated from the front did not significantly change state. (b) A similar device irradiated from the back shows considerable R_{off} changes for the same programming current of 50 µA[153]. © 2014, IEEE.

In all the studies mentioned above, the devices were able to recover their states after a few cycles and no permanent damage was observed. Studies show that memristors have excellent resistance to damage from certain types of irradiation, but are susceptible to others to a certain extent, and might be a suitable candidate for radiation-hardened electronic networks.

There are multiple ways radiation can affect a memristive device. Device structure, radiation-type, dose, duration, bias, area, and direction appear to play a major role in the response of memristor memory to irradiation. This section groups the observed behavior of the memristors (under radiation) in three different categories: interaction events that only change the state, those that cause ionization, and events that alter the R_{off} (off-state resistance) value of a memristor. The radiation model detailed in the latter part of the chapter is motivated by these three observed behaviors.

3.1.1 State-Altering Radiation

In this case, a radiation event will change the programmed conductive state of the device. Such radiation effects have been experimentally observed in most of the oxide-based devices. Proton irradiation in TiO_2 [141], alpha irradiation in TiO_2 [118], [149], proton irradiation in TaO_x [150], proton irradiation in HfO_2 [151] and alpha and proton irradiation in $Ge_{30}Se_{70}$ ReRAMs [153] all showed the decrease in resistance post-radiation when set in the off-state.

3.1.2 Ionization Radiation

This is the case when a radiation event will deliver the total ionization dose to the device. This happens in the case of gamma radiation exposure and memristive devices are noted to be unaffected by this irradiation [118], [150], [153]. Experimental study on TiO_2 memristors noticed no degradation in states of the device when exposed to 45 Mrad(Si) of 1 MeV gamma radiation [140].

3.1.3 Off-Resistance Change

It is also noted that radiation event changes the off-resistance (R_{off}) of the device without influencing the on-resistance, thus changing the read window of the device [118], [140], [141], [150]–[153]. Although, devices are observed to recover their initial value of off-resistance when cycled.

3.2 Adding Radiation to the Memristor Model

3.2.1 Modeling Radiation

The memristor model with radiation effects is implemented in Cadence Virtuoso using Verilog-A. The greyed-out part of the model represented in Figure 3.4 is implemented in Verilog-A (APPENDIX C). In the model, $Irad_{sc}$ i.e. a state-altering radiation current (as discussed in Section 3.1.1) is added to the auxiliary circuit (Figure 3.4) so that the current can effectively change the state of the device. Note that $Irad_{sc}$ must be added in parallel to G_x, such that both currents sum before being multiplied by the window function f(x). This will still keep the state variable $\frac{w}{D}$ bounded within limits of zero and one.

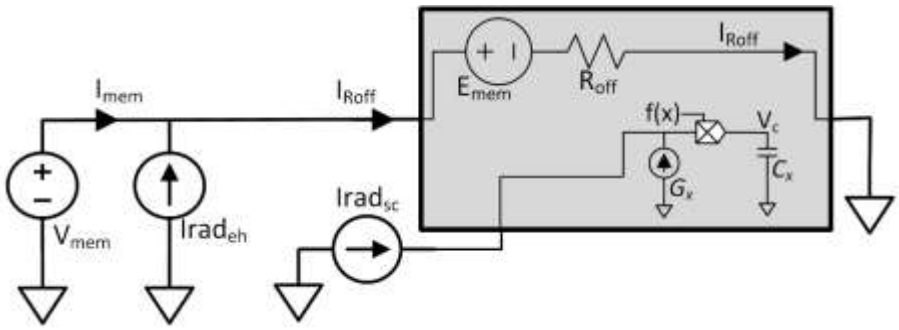

Figure 3.4 Memristor model with radiation effects is implemented in Cadence Virtuoso using Verilog-A. Ionization ($Irad_{eh}$) radiation is added in parallel with the source, thus adding to I_{mem} directly without affecting the state variable. State Change ($Irad_{sc}$) is added to the auxiliary circuit so it can modify the state of the device instantaneously. R_{off} is modified as a variable in Verilog-A. The portion inside the grey box is coded using Verilog-A (APPENDIX C).

Thus, in the radiation model, as shown in Figure 3.4, Equation (2.6) becomes:

$$\frac{dV_c}{dt} = (G_x + \text{Irad\_sc})\, f(x), \qquad \begin{matrix} \text{if } 0 < \frac{w}{D} < 1, \quad f(x) = 1 \\ \text{else,} \qquad f(x) = 0 \end{matrix} \tag{3.1}$$

On the other hand, $Irad_{eh}$ i.e. an ionization radiation current (as discussed in Section 3.1.2) is added to the main memristive circuit, as shown in Figure 3.4, so it can add up to the I_{mem} directly without affecting the state variable of the device. The resulting schematic is shown in Figure 3.4.

3.2.2 Quantifying Radiation

Current sources $Irad_{sc}$ and $Irad_{eh}$ artificially induce radiation in the circuit using pulses of 1 ms duration. The current pulse train magnitude follows a random Gaussian distribution with mean μ and standard deviation σ, and time intervals follow a Poisson process similar to radiation patterns observed in real sources. In the model, one current pulse does not necessarily represent one radiation particle or interaction event.

In the literature, experimental studies using memristors have observed 30% [141], 77% [118], [149], 90% [154], and 95% [150] change in resistance (from off-state) when bombarded with radiation of a total fluence of $7.7x10^{15}$ 350-keV proton/cm^2, $1.4x10^{11}$ 1-MeV alpha/cm^2, $4.9x10^{12}$ 14.1-MeV neutrons/cm^2, and $7.75x10^{16}$ 10-keV x-rays/cm^2 respectively. Similar changes can be induced in the designed memristor model when 10, 20, 25, and 30 $Irad_{sc}$ current pulses of magnitude $\mu = 25$ μA and $\sigma = 12.5$ μA are applied.

Thus, the model results are comparable to the experimental studies performed on TiO_2 memristors. For this work, simulation of the networks is performed at different radiation flux or intensity, obtained by modifying the pulse interval (following a random Poisson distribution) and the magnitude [120]. Synaptic weight change ($\Delta\frac{w}{D}$) of memristive synapses increases as the mean magnitude and frequency (flux) of state-altering radiation current increases. Flux calculations in the study are based on an assumed 100 nm x 100 nm interaction size for the memristive devices.

3.2.3 Simulating Radiation

This section presents the device simulation results as the state-altering, ionizing, and off-state changing radiation current interacts with the designed circuit. All the simulations are captured in Cadence Virtuoso Spectre.

3.2.3.1 Radiation-induced state alteration

State-altering radiation current ($Irad_{sc}$) is applied, under different device initial conditions and changes in the synaptic weight ($\Delta\frac{w}{D} = \frac{w}{D}_{(initial)} - \frac{w}{D}_{(final)}$) are plotted in Figure 3.5. Application of positive $Irad_{sc}$ increases $\frac{w}{D}$ and thus the $\Delta\frac{w}{D}$ ratio moves in a positive direction. Negative $Irad_{sc}$ moves the $\Delta\frac{w}{D}$ ratio in a negative direction. The state variable $\frac{w}{D}$ is normalized and limited from zero to one by the window function f(x). In the case when the device is initialized at $\frac{w}{D}$ = 0.25, $\Delta\frac{w}{D}$ is varying from +0.75 to −0.25 as expected. Similarly, in the case of initial $\frac{w}{D}$ = 0.5, $\Delta\frac{w}{D}$ is varying from +0.5 to −0.5, and in the case of initial $\frac{w}{D}$ = 0.75, $\Delta\frac{w}{D}$ is varying from +0.25 to −0.75 as expected. The initial values of 0.25, 0.5, and 0.75 were chosen simply for equal spacing between the bounds of $\frac{w}{D}$.

Figure 3.5 also plots the simulated effects of change in the pulse width of state-altering radiation current ($Irad_{sc}$). In the case of initial $\frac{w}{D}$ = 0.25 higher pulse width (longer duration of radiation $Irad_{sc}$) of 1.5 ms, the device reaches its limit at a very small $Irad_{sc}$ of less than 5 mA. On the other hand, at a smaller pulse width of 0.5 ms, higher $Irad_{sc}$ of more than 15 mA is needed to achieve saturation. Other initial conditions display similar pulse width behavior. Thus, we can conclude that the change in the state of the device is affected by both the magnitude and the duration of the radiation current $Irad_{sc}$. $\Delta\frac{w}{D}$ and $Irad_{sc}$ pulses

are varied to capture the typically observed changes. Similar experimental results were reported in TiO_x and TaO_x based memristive devices [118], [150]. $\Delta\frac{w}{D}$ will also be affected by the initial state of the device although most experimental studies present in literature are done on devices in the off-state [118], [150].

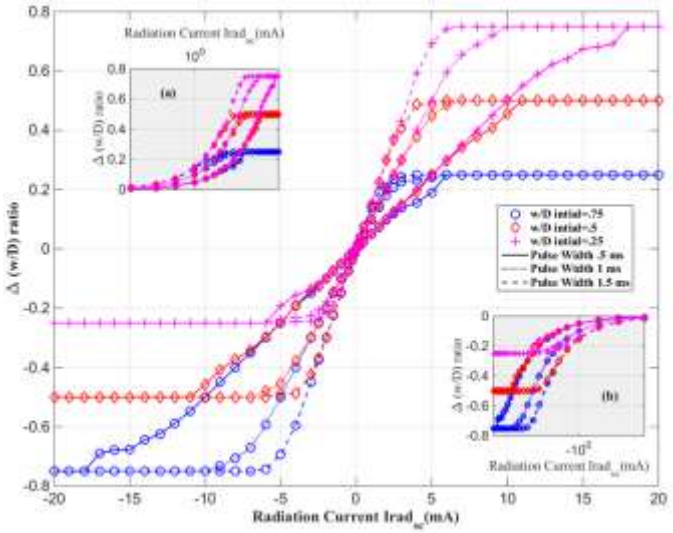

Figure 3.5 Change in the state ($\frac{w}{D}$ ratio) of the device when exposed to $Irad_{sc}$ of different magnitude and duration. The device is studied under multiple initial conditions. The initial values of 0.25, 0.5, and 0.75 were chosen simply for equal spacing between the bounds of $\frac{w}{D}$.

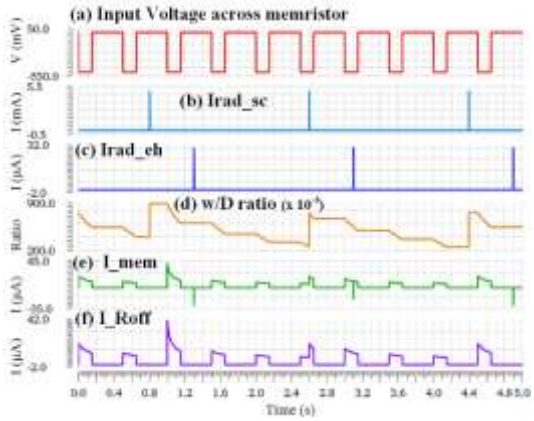

Figure 3.6 (a) Input voltage applied (Vmem) is a train of −500 mV pulses with width 150 ms. The effect of radiation that leads to device (b) state change and (c) ionization on (d) $\frac{w}{D}$ ratio. (e) The corresponding I_{mem} and (f) memristor current (I_{Roff}).

Figure 3.6 and Figure 3.7 illustrate the effect of $Irad_{sc}$ on $\frac{w}{D}$ and I_{mem} in a transient simulation. Figure 3.6 (a) shows the input V_{mem} pulse train of −500 mV with the pulse width of 150 ms, Figure 3.6 (b) shows the $Irad_{sc}$ spiking to 3 mA for 1 ms at 0.8 s, 2.6 s and 4.4 s and Figure 3.6 (c) shows $Irad_{eh}$, which is discussed in next section. Observe in Figure 3.6 (d), every time $Irad_{sc}$ occurs the state of the device switches immediately. At 0.8 s when the first $Irad_{sc}$ pulse appeared, the device was in the off-state so the state of the device changed immediately. I_{mem} in Figure 3.6 (e) did not increase until the device is turned on again at 0.9 s, whereas when the next $Irad_{sc}$ radiation pulse appears at 2.6 s, the device was in the on-state, so the state $(\frac{w}{D})$ and I_{mem} changes simultaneously. The $\frac{w}{D}$ achieved for $Irad_{sc}$ pulse at 0.8 s is higher than at 4.4 s because right before the 4.4 s device was in much lower $\frac{w}{D}$ state than right before 0.8 s pulse. Thus, for the same magnitude of radiation current pulse, the initial state of the device will affect the final magnitude of the state change due to the non-linearity of the memristive device. Further $Irad_{sc}$ radiation in itself will not be the source of any current in the device.

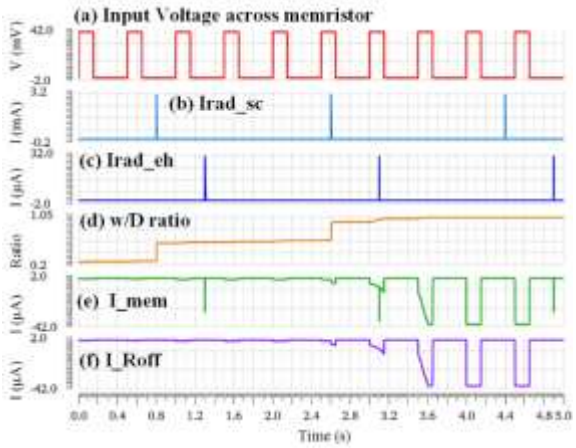

Figure 3.7 (a) Input voltage applied (Vmem) is a pulse train of 40 mV with a pulse width of 150 ms. The low negative voltage is chosen to see the changing state over time. The effect of radiation that leads to device (b) state change and (c) ionization on (d) $\frac{w}{D}$ ratio, (e) I_{mem}, and (f) I_{Roff}.

$Irad_{sc}$ shows a similar effect in Figure 3.7, where an input V_{mem} pulse train of 40 mV with a pulse width of 150 ms in Figure 3.7 (a). In Figure 3.7 (d) $\frac{w}{D}$ saturates to one very quickly after just two events of $Irad_{sc}$ radiations. This is because the radiation current ($Irad_{sc}$) and positive V_{mem} pulse train forces the device state ($\frac{w}{D}$) towards saturation and thus high I_{mem} is observed through the device in Figure 3.7 (e).

3.2.3.2 Effect of ionizing radiation

The behavior of the memristor in the presence of an ionizing radiation current pulse ($Irad_{eh}$) is also presented in Figure 3.6 and Figure 3.7. In Figure 3.6 (c) ionizing radiation (at 3 mA for 1 ms) hits the circuit at 1.3 s, 3.1 s, and 4.9 s. Both I_{mem} in Figure 3.6 (e) and I_{Roff} in Figure 3.6 (f) are not equal when $Irad_{eh}$ arrives. The active voltage source compensates for the increase in $Irad_{eh}$ thus, I_{Roff} observes no change due to the ionization event, i.e. $Irad_{eh}$ does not affect the state or the current passing through the device. $Irad_{eh}$ shows a similar effect in Figure 3.7, where the input V_{mem} pulse train is positive in Figure 3.7 (a). Even after $\frac{w}{D}$ saturates in Figure 3.7 (d), $Irad_{eh}$ radiation does not affect the I_{Roff} device in Figure 3.7 (f).

Similar results are experimentally recorded in [118] where no detectable effect of ionization is observed on the device itself. On the other hand, the experimental results in [152] indicate no changes in memristive devices at the lower x-ray radiation dose, but a higher dose rate changed the off-resistance of the device, which might be due to changes in physical structure. More simulation results for off-resistance change are presented in the following section.

3.2.3.3 Change in off-state resistance

Alpha radiation experimentally leads to a state change in TiO_2 devices in [140], but no change in R_{off} or R_{on} are reported in their devices, contrary to alpha radiation studies done on TiO_2 devices in [149], which shows the change in R_{off} due to device deterioration. Thus, we concluded the radiation event may lead to change in both R_{off} and the state of the devices at the same time, as simulated in Figure 3.8.

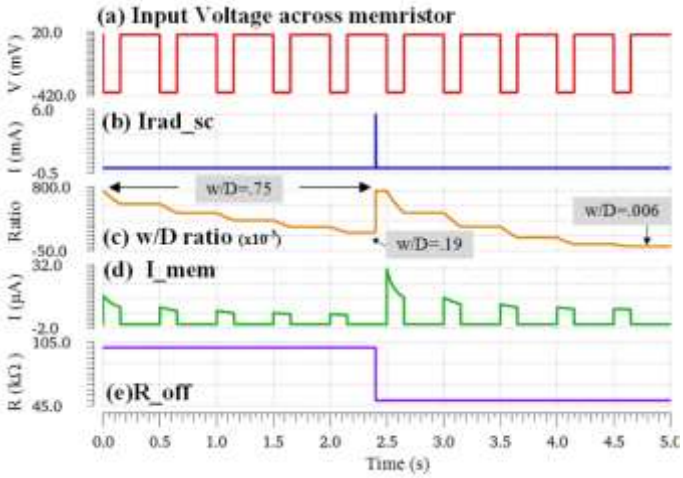

Figure 3.8 (a) Input voltage applied (V_{mem}) is a pulse train of −500 mV with a pulse width of 150 ms. Voltage is chosen as such to see the effect of changing R_{off} on the device. (b) The state-altering radiation pulse (IRad_sc) that changes the off-resistance of the device. (c) The $\frac{w}{D}$ ratio versus time. (d) Memristor current I_{mem} as radiation hits the device. (e) The decrease in the R_{off} following a radiation event.

One such event is depicted in Figure 3.8, whereas as soon as the $Irad_{sc}$ radiation event occurs, the R_{off} of the device which was set to 100 kΩ is decreased to 50 kΩ in the model. The input (V_{mem}) in Figure 3.8 (a) is a pulse train of −500 mV with a pulse width of 150 ms. It is chosen as such to observe the effect of change of resistance more clearly. In Figure 3.8 (b) $Irad_{sc}$ enters the device after 2.4 s producing 5.6 mA of current for 1 ms (the device is in off-state at 2.4 s). This instantaneously lowers the off-resistance of the device from 100 kΩ to 50 kΩ, as shown in Figure 3.8 (e). In Figure 3.8 (c), initial $\frac{w}{D}$ = 0.75 at 0 s

and as $Irad_{sc}$ hits the device at 2.4 sec, the $\frac{w}{D}$ instantaneously switches back to the initial value of 0.75 ($Irad_{sc}$ was chosen as such). Further, even though the $\frac{w}{D}$ value is the same in the simulation both at 0 s and 2.5 s, but in Figure 3.8 (d) the current I_{mem} is almost twice as much at 2.5 s. That is because the R_{off} decreases (to half from 100 kΩ to 50 kΩ) as a result of radiation. Thus, the device is letting through higher current even in the higher resistive state. Also, Figure 3.8 (d) demonstrates that the $\Delta\frac{w}{D}$ has changed considerably due to radiation event, going from 0.56 = 0.75 − 0.19) pre-radiation to 0.744 = 0.75 − 0.006 post-radiation for identical input pulses applied. This indicates that the read window has decreased for the device post-radiation. Similar results can be observed in experimental studies performed in references [149], [151]–[153].

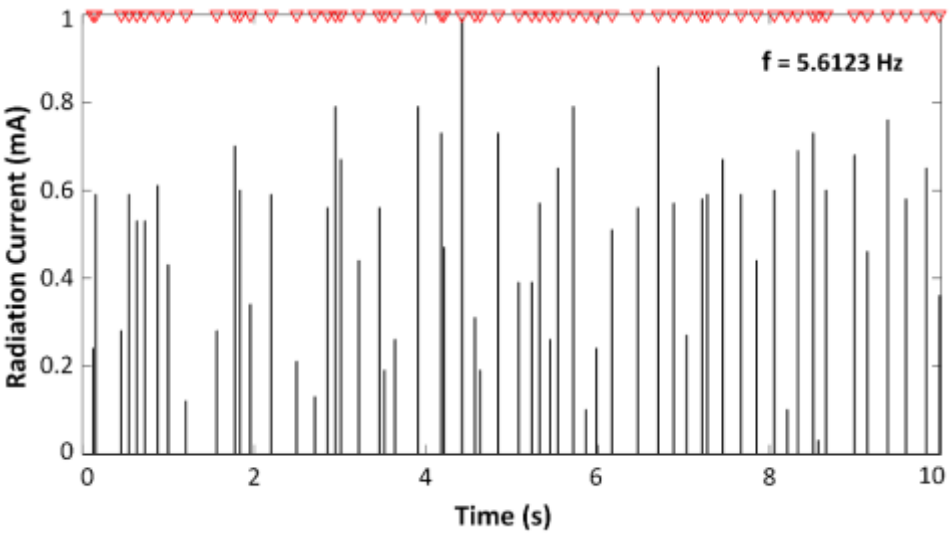

Figure 3.9 Shows the sample distribution of the radiation current spikes for 10 s at a frequency of 5.6123 Hz. The current pulse magnitude follows the random Gaussian distribution and the pulse interval follows the random Poisson distribution.

3.2.3.4 Stochastic radiation effects

Characteristically energy of emitted radioactive particles follows random Gaussian distribution and the pulse interval follows the random Poisson distribution [155], [156]. Figure 3.9 presents the radiation current spikes following Gaussian and Poisson distribution. In the example, in Figure 3.9, the memristive device will see the radiation current spikes at 5.6123 Hz frequency.

Figure 3.10 (a) plots the histogram showing the spike interval between two consecutive spikes from Figure 3.9. The histogram shows the desired Poisson distribution with $\lambda = 0.25$ s. The histogram in Figure 3.10 (a) plots the current magnitude distribution of each radiation current pulse. The histogram shows the Gaussian distribution of the magnitude. In this case, the mean and standard deviation of the current magnitude is 0.5 mA and 0.25 mA respectively. Throughout this dissertation, radiation frequency is kept at an average of 5 Hz with a standard deviation of 1 Hz, although mean and standard deviation are modified to simulate the desired effect. The radiation effects on the network are discussed in 0

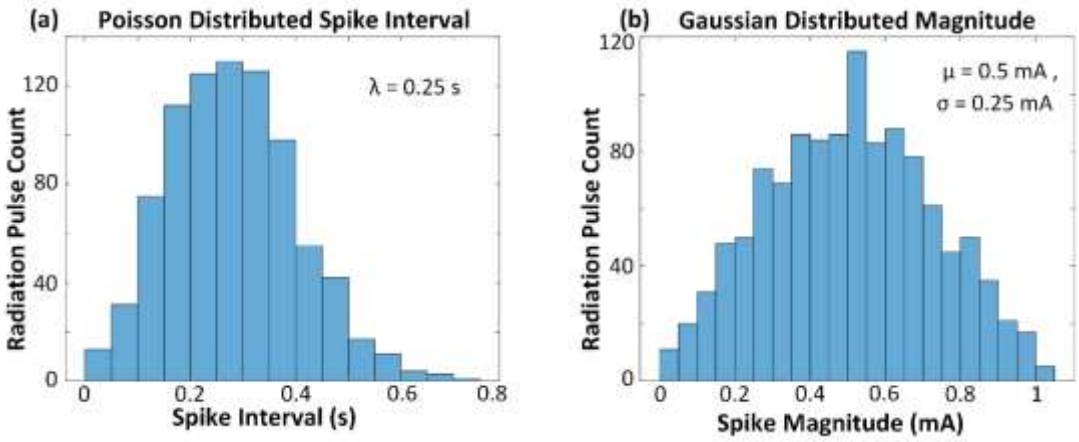

Figure 3.10 Histograms show the radiation current (a) spike interval distribution and (b) spike magnitude distribution. The pulse magnitude follows random Gaussian distribution and the pulse interval follows the random Poisson distribution.

In Figure 3.11, the effects of $Irad_{sc}$ and $Irad_{eh}$ are simulated when they are occurring simultaneously due to radiation but do not change the off-resistance of the device. The $Irad_{sc}$ in Figure 3.11 (c) and $Irad_{eh}$ in Figure 3.11 (d) are generated such that the current magnitude follows random Gaussian distribution and the pulse interval follows the random Poisson distribution.

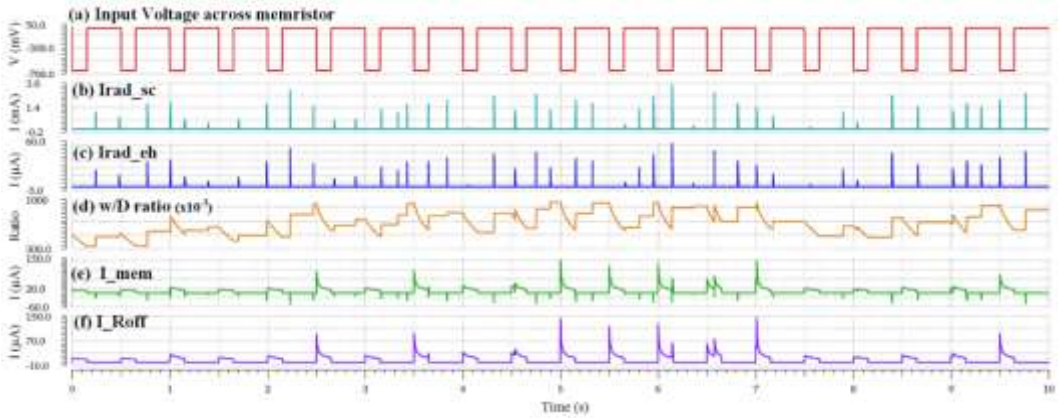

Figure 3.11 (a) Input V_{mem} applied at −650 mV amplitude and 150 ms pulse width. (b) $Irad_{sc}$, state change radiation, and (c) $Irad_{eh}$, ionization radiation. Both $Irad_{sc}$ and $Irad_{eh}$ are generated randomly, with Gaussian distributed magnitude and Poisson's distributed interval (d) $\frac{w}{D}$ ratio changes accordingly and reached to the maximum often but stays in the limit. (e) I_{mem} balances $Irad_{eh}$ and (f) $Irad_{sc}$ modifies the state of the device and I_{Roff} in proportion to its magnitude and state of the device right before the event.

Input (V_{mem}) in Figure 3.11 (a) a pulse train of −650 mV with a pulse width of 150 ms is applied to the device. The result obtained follows the similar behavior observed in Figure 3.6 and Figure 3.7. I_{mem} balances $Irad_{eh}$ during each event, so device current or state are not affected. On the other hand, $Irad_{sc}$ modifies the state of the device in proportion to its magnitude and the state of the device right before the event. Similar results can be observed in [118], [140], [150]. $\frac{w}{D}$ reached a maximum value of one at multiple places such as at 2.5 s, 4.9 s, and around 6 s but always stays bound within the limits of $0 < \frac{w}{D} < 1$.

3.3 Conclusion

To conclude, radiation interactions that generate a current which alters the state of the device would change the current flowing through the device when the device turns on, or immediately if a radiation event occurs when the device is in the on-state. On the other hand, radiation that results in ionization only does not stimulate change in the state of the device. Radiation events that change the off-resistance of the device also decrease the read

window of the device as the rate of change of $\frac{w}{D}$ changes considerably. Thus, post-radiation more current passes through the device as compared to pre-radiation for the same voltage across it in the same state.

The modified memristor model presented in this chapter was able to mimic the experimental behavior of the memristors under radiation. The transient simulations included waveforms generated during the events that would change the state of the memristive device or increase the current in the device or both at the same instance. Instantaneous changes in memristor current and resistance state and behavior of the model in the presence of stochastic radiation events were also demonstrated in this chapter.

CHAPTER 4: NEURAL NETWORK DESIGN

This chapter discusses the design, structure, and components of the memristor-based neural networks used in this dissertation. Neural networks have three basic components: pre-synaptic neurons, post-synaptic neurons, and memristive synapses, connecting afferents to the output layer. Memristive synapses modeled in Verilog-A have been discussed in detail in CHAPTER 2:. For simulation purposes, piecewise linear independent voltage supplies are used to mimic the pre-synaptic neuron behavior. The post-synaptic neuron was designed using a leaky integrate-and-fire (LIF) circuit to simulate the biphasic spiking behavior similar to the pre-synaptic neurons.

The LIF circuit used in this dissertation is discussed in the first section of the chapter. This study uses two types of network topologies that are both feed-forward and fully connected, also discussed in this chapter. Both networks follow spike-timing-dependent plasticity (STDP), biological Hebbian learning, where the conductivity of the memristive synapse (the connection between two neurons) is modified interdependently, due to the presence of pre- and post-synaptic neuron firing time. The chapter also presents the simulations discussing the factors that affect the pair-based STDP learning rule in the network. Later parts of the chapter discuss the learning capabilities of the network. The effect of radiation on the learning abilities of the memristor-based neural networks is discussed in 0. The contributions from this chapters are published in [120], [121].

4.1 The Leaky Integrate-and-Fire (LIF) Post-Synaptic Neuron

The post-synaptic neuron used in the biphasic spiking neural network is designed in Verilog-A (APPENDIX D) and represents a leaky integrate-and-fire (LIF) circuit behavior governed by the Hodgkin-Huxley equations. The LIF neuron behavior is implemented in the literature using a single opamp and MOSFETS [157]–[159]. This dissertation uses the behavioral model of the LIF designed in Verilog-A (APPENDIX D) to increase the speed and efficiency of the simulated circuit. The LIF circuit fires a bidirectional biphasic spike toward the dendritic and axonic synapses when a certain threshold is reached. The schematic depiction of the LIF circuit is presented in Figure 0.1 (a). The input of the circuit, V_{PostIn}, is the node connected to the output of all the memristors in the fully connected network presented in Figure 0.3. V_{PostIn} changes with the change in the conductivity of the memristors and the spike timing of the pre-synaptic afferents in the neural network.

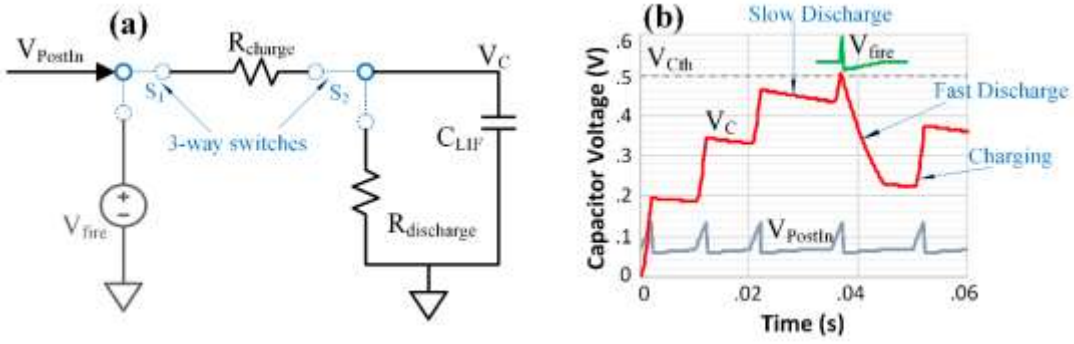

Figure 0.1 (a) Leaky integrate-and-fire (LIF) post-synaptic neuron circuit. The circuit is designed in Verilog-A. The voltage source V_{fire} produces the desired shape of post-synaptic biphasic spike. C_{LIF}, R_{charge}, and $R_{discharge}$ are responsible to mimic the leakiness of the biological synapse. (b) The plot shows the increase in the voltage across capacitor C_{LIF} as the circuit sees the input spikes over time (V_{PostIn}). V_{fire} sends out the output spike as V_C reaches threshold voltage V_{Cth} (= 0.5 V in this case).

In Figure 0.1 (a), the switches S_1 and S_2 are initially connected to R_{charge} (1 GΩ), thus charging C_{LIF}. If at any point, V_{PostIn} is less than the voltage across C_{LIF}, S_2 flips and C_{LIF} starts discharging via $R_{discharge}$ at 20 GΩ for a slow leak. As soon as V_{PostIn} is larger than the voltage across C_{LIF}, S_2 flips back and C_{LIF} starts charging again via R_{charge} at 1 GΩ. At times when the voltage across C_{LIF} becomes greater than a certain threshold (discussed in Section 0), S_2 connects to $R_{discharge}$ and S_2 connects to V_{fire} and the circuit fires a desired biphasic spike, designed in the Verilog-A code. In this condition, $R_{discharge}$ is at 1 GΩ for quick C_{LIF} discharge or reset, and V_{fire} produces a biphasic spike traveling toward the memristors (axonic synapses), thus updating their weight via the STDP learning rule. The charging and discharging states of the capacitor are shown in Figure 0.1 (b). As the input spike arrives the capacitor charges and discharges slowly in the absence of a positive spike. The charging and discharging process continues until just before 40 ms, in Figure 0.1 (b), when the capacitor reaches a threshold (V_{Cth} = 0.5 V in this case). At this point, V_{fire} fires a bidirectional biphasic spike, which is sent towards the present and the next layer of memristors (dendritic synapse) in the network (not used in this dissertation). The capacitor discharges rapidly during the time V_{fire} is firing the biphasic spike, as shown in Figure 0.1 (b). Please see the Verilog-A code in APPENDIX D.

The threshold (V_{Cth}) for the voltage across C_{LIF} in Figure 0.1, which would lead to the post-synaptic afferent fire, depends on various factors. These factors include and are not limited to the number of afferents used in the network, the charging, and discharging time constants, the pre-synaptic pulse width, the frequency, and the amplitude. Too low of a threshold may make the network unstable by changing the weights too fast. On the other

hand at too high of a threshold, the network weights may not change much or at all and thus the network would be unable to learn.

4.2 Neural Network Topology

This work uses two types of network topologies, as shown in Figure 0.2 and Figure 0.3. Both memristor-based neural networks are fully connected, where all the pre-synaptic afferents are connected to all the post-synaptic afferents via memristors. The networks are also unsupervised and are feed-forward i.e. the connections between the nodes are not cyclic, unlike recurrent neural networks. The networks also use multiple memristors acting as synapses. Each pre-synaptic afferent is connected to each post-synaptic afferent via one memristor. The synaptic memristors define the conductivity of the connection between the two afferents. The conductivity of the synapse follows STDP, which is modified continuously depending on the activities noted by the two connected afferents.

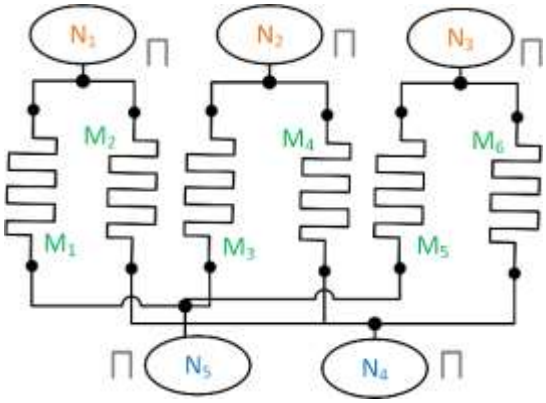

Figure 0.2 The memristor-based electronic Pulsed Neural Network used in this dissertation. Three pre-synaptic neurons are each connected to two post-synaptic neurons via memristors used as synapses. This network uses randomly occurring digital square pulses to modify the synaptic weights.

The pulsed neural network shown in Figure 0.2 has all three pre-synaptic neurons (N_1, N_2, and N_3) electrically connected to two post-synaptic neurons (N_4 and N_5) via six

memristors (M_1 to M_6). This network uses square digital pulses as the action potentials and is used for preliminary simulations.

The second topology is represented by a spiking neural network in Figure 0.3 and is a single layer perceptron network with either 25 or 100 pre-synaptic afferents (N_1 to $N_{25/100}$), each connected to a single post-synaptic neuron (LIF post N) via single memristors (M_1 to $M_{25/100}$). This network is used in this dissertation to learn the desired 25-pixel or 100-pixel pattern.

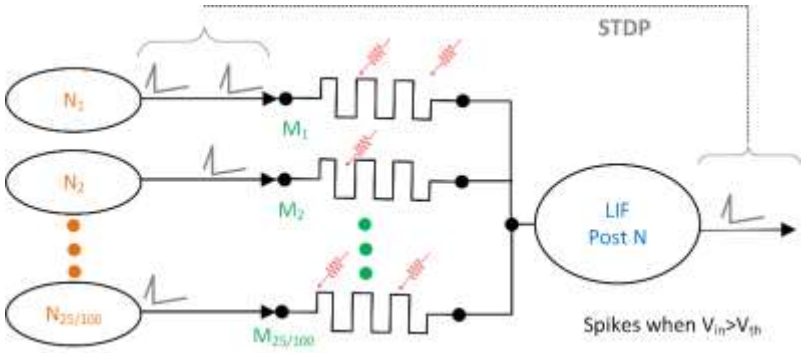

Figure 0.3 The memristor-based electronic Spiking Neural Network used in this dissertation for spatio-temporal pattern recognition. 25 or 100 pre-synaptic neurons are connected to one post-synaptic leaky integrate-and-fire (LIF) neuron via single memristors. The network uses biphasic shaped pulses to achieve pair-based STDP for pattern learning.

4.3 Neural Network Simulations

This section discusses the simulations performed using the two neural networks that were discussed in the last section. All networks and experimental conditions are simulations and captured in Cadence Virtuoso Spectre. No radiation effects are discussed in this chapter.

4.3.1 Pair Based STDP

As mentioned in Section 0, STDP is a biological process that changes the strength of the connection between two neurons based on pre- and post-synaptic neuron firing time. STDP is also deemed responsible for the brain's ability to form memories, locate sounds, and respond to threats [160], [161]. Many varieties of STDP are biologically observed in different areas of the brain in different species. The STDP followed in this research is closest to one observed in the neocortex layer of the hippocampus region in the human brain [160], [161]. In memristive devices, different shapes of pre- and post-synaptic neuron spikes can be used to obtain the desired STDP shape [162]–[165] Often, a simple pair-based STDP implementation is used, although frequency-dependent effects are typically observed in neuroscience experiments, as in [166]. This section discusses the effects of various factors on the STDP learning curve.

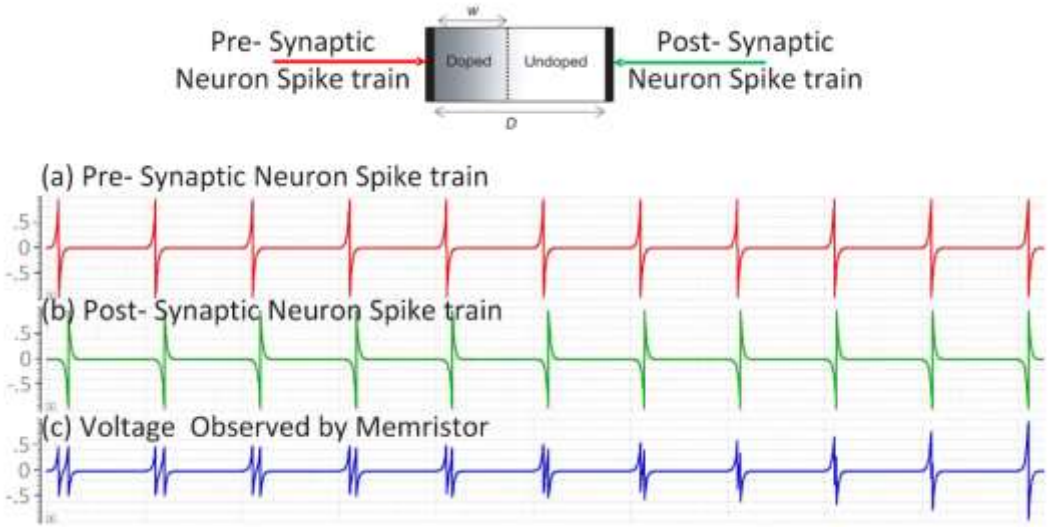

Figure 0.4 The two terminals of a Memristor are connected to the pre- and post-synaptic neuron inputs. Spike trains in (a) show the pre-synaptic neuron spike produced and (b) shows the post-synaptic neuron spike observed by the memristor terminal. The magnitude and shape of both are the same, except there is a difference in their arrival times. Due to the difference in arrival time, the memristor observes the voltage given in (c) across it. Thus, the synaptic weight change would be different at each pre-post pairs' arrival, resulting in the STDP curve.

Figure 0.4 shows the test structure used to capture the spike-timing-dependent plasticity (STDP) curve. The memristor is connected to a source of pre-synaptic and post-synaptic biphasic spikes entering into the two terminals. The pre- and post-synaptic 10 ms biphasic spikes arrive at different time intervals as in Figure 0.4 (a) and (b). Due to this time difference, the memristor sees varying potential across it as shown in Figure 0.4 (c). This varying potential across the memristor, combined with the memristor threshold (discussed in later sections) changes its conductivity. Therefore, every pre-post pair arriving within a certain time window (called learning window) leads to the change in the magnitude of the synaptic weight.

4.3.1.1 Initial $\frac{w}{D}$ and pulse-shape

STDP in Figure 0.5 (a) is obtained using an exponential biphasic spike, and Figure 0.5 (b) uses a triangular biphasic spike, as shown in the respective insets. It can be noted in Figure 0.5, the magnitude of change in synaptic weight ($\Delta\frac{w}{D}$) at any given time will depend on the initial synaptic state of the device and the shape of the pre- and post-synaptic pulses.

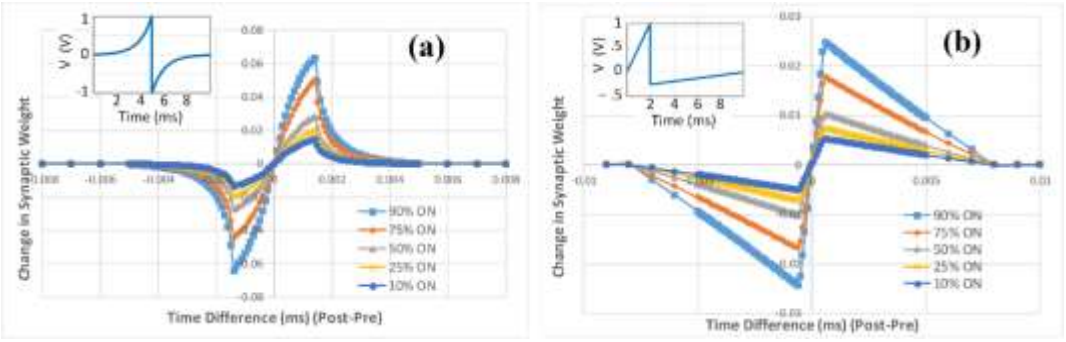

Figure 0.5 Different STDP shapes obtained using (a) exponential and (b) triangular biphasic pulses as seen in the respective insets. The magnitude of change in synaptic weight ($\Delta\frac{w}{D}$) also increases if the device was initially in the lower conductive state that is due to the non-linearity of the memristor model.

In Figure 0.5 when the device was initially in a less conductive state, i.e at lower $\frac{w}{D}$ (10%), it saw about a six to ten times larger change in synaptic weight when compared to when the device was initially at 90% $\frac{w}{D}$, i.e. in a highly conductive state. This was due to the non-linearity present in the device, as discussed in CHAPTER 2:. Also, the difference in the shape of the STDP curve can be noted in Figure 0.5 (a) and Figure 0.5 (b). The triangular spikes in Figure 0.5 (b) give more distinct and sharper changes in the $\Delta\frac{w}{D}$. On the other hand, the exponential input in Figure 0.5 (a) provides a gradual larger change in $\Delta\frac{w}{D}$ with up to 6% as compared to 2% due to the triangular spikes. This is due to non-linearity in the potentiation of the exponential curve.

4.3.1.2 Memristor threshold

The STDP curve in Figure 0.6 is collected using exponential biphasic spikes, as shown in the inset. In this case, the threshold, V_{th}, of the synaptic memristor device is changed from 0.25 V to 1 V, observing the change in STDP. In the case when the threshold is set to 0.5 V, the memristor will not change its state until the voltage drop across it is equal to or greater than 0.5 V (the threshold).

In Figure 0.6, as the magnitude of V_{th} decreases, the read window increases for the same 100 ms pulse. The read window is the duration where a memristive device will see the change in the weight ($\Delta\frac{w}{D} > 0$) due to the arrival of pre- and post- synaptic spike. In the case of V_{th} equal to the 0.5 V, the learning window is 120 ms because $\Delta\frac{w}{D}$ is not zero for $-60\ ms < \Delta t > 60\ ms$. On the other hand, in the case of V_{th} equal to the 1 V learning window is only 70 ms because $\Delta\frac{w}{D}$ is not zero for $-35\ ms < \Delta t > 35\ ms$.

Lower threshold (V_{th}) values result in a larger read window and the magnitude of the $\Delta\frac{w}{D}$ is severely affected. In Figure 0.6, at Δt = 10 ms, if the device V_{th} is set at 0.25 V it observes 50% less change in $\frac{w}{D}$ ($\Delta\frac{w}{D}$ = 1%) as compared to when device V_{th} is set at 0.75 V ($\Delta\frac{w}{D}$ = 2%). At 0.25 V_{th}, the network will be unable to distinguish between the pre- and post-synaptic pair arriving between 5 ms and 40 ms (−5 ms and −40 ms). Thus, the network would be unable to lower or increase the synaptic weights correctly and will not learn any certain pattern.

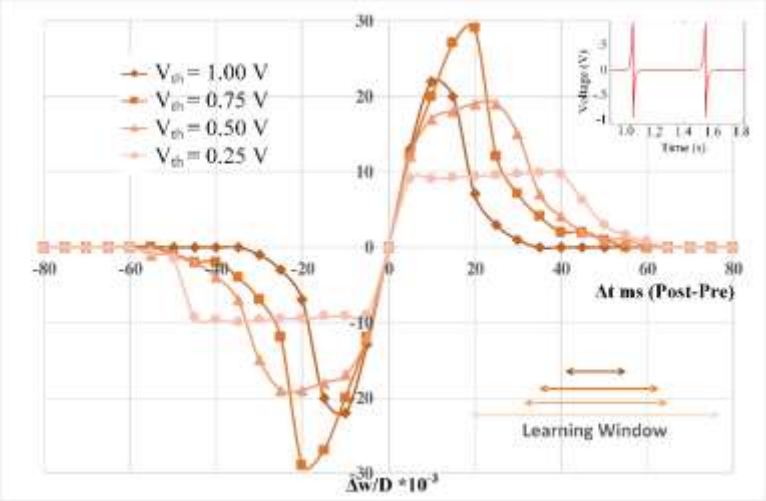

Figure 0.6 Change in the STDP learning rule as the threshold of the memristor changes. Input spikes, in this case, are 100 ms, 1V exponential biphasic pulses, as shown in the inset. As the threshold decreases, the learning window increases, but the magnitude of change in the synaptic weight ($\Delta\frac{w}{D}$) decreases and becomes undesirably flat.

4.3.1.3 Effect of pulse width

The STDP curve in Figure 0.7 is collected using exponential and triangular biphasic spikes, as shown in the inset. In this case, the width of the triangular and the exponential spikes is changed to observe the change in STDP.

Similar to Figure 0.5, Figure 0.7 also shows that the change in the synaptic weight ($\Delta\frac{w}{D}$) is higher in the case of the exponential spikes when compared to their triangular counterparts. Figure 0.7 also shows that as the pulse width decreases, the read window decreases. The read window for 50 ms pulse width spikes is about 60 ms, and the read window for 100 ms pulse width spikes is about 120 ms. The read window is independent of the pulse shape. The decrease in the read window with pulse width is simply due to the reason that the duration of the spike is small. If the 50 ms pre-synaptic spike will arrive 60 ms before or after the 50 ms post-synaptic spike, they will be too far apart to add up to pass the desired threshold to make any change in the STDP (as depicted by earlier spikes in Figure 0.4).

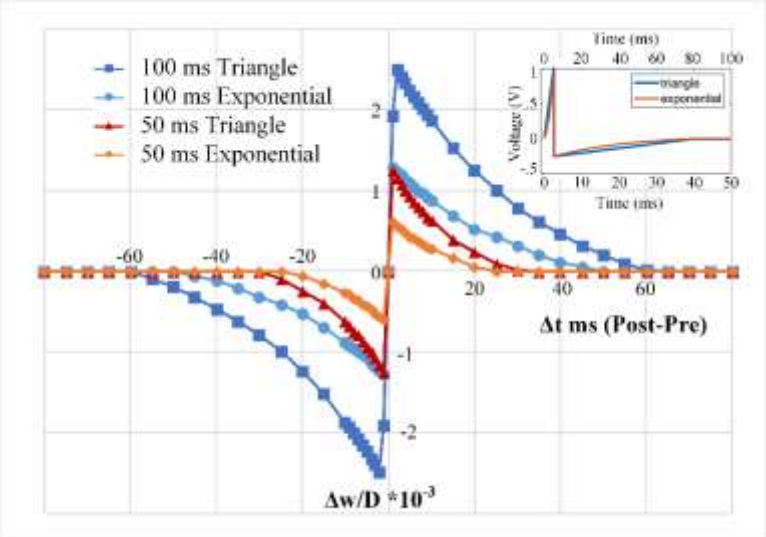

Figure 0.7 Change in the STDP learning rule as the shape and width of the input biphasic spike changes. Input spikes, in this case, are either a triangular or an exponential biphasic pulse of 50 ms or 100 ms, as shown in the inset. As the pulse width decreases, the learning window decreases. It is also noted that the magnitude of change in synaptic weight ($\Delta\frac{w}{D}$) decreases with a decrease in pulse width and pulse shape.

4.3.2 Pattern Learning

Pre-synaptic afferents (N_1 to $N_{25/100}$), in the biphasic spiking neural network in Figure 0.3, are firing at an average rate of 5 Hz for the 100 s simulation time. Afferents that are part of the pattern (a 10-pixel 'B'), as shown by Figure 0.8 (b) (light color), are firing mutually correlated spikes at a regular interval, as shown in Figure 0.8 (a), N_{12} and N_{13} [167], [168]. Conversely, non-participating afferents in Figure 0.8 (b) (dark color), fire uncorrelated spikes with Poisson distributed intervals as shown by N_{14} and N_{15} in Figure 0.8 (a). This same firing pattern is used in generating a 100-pixel 'B' pattern in the larger 100 afferent networks of the next chapter.

Pre- and post-synaptic afferents fire a biphasic triangular spike for 10 ms, which potentiates to a peak voltage of +1 V and the depression tail reaches a maximum of −0.25 V, as shown in the inset in Figure 0.9. All of the memristors in the spiking neural networks are initially kept in a conductive state with a resistance distribution varying from 20 kΩ and 35 kΩ, as can be noted in Figure 0.8 (b) (Initial State).

Figure 0.8 (b) shows the synaptic weight evolution of all the memristors (M_1 to M_{25}) as the network tries to learn a 25-pixel letter 'B'. Starting around 30 s, the network was able to depress most of the uncorrelated neurons by decreasing the conductivity of their corresponding memristors and the desired pattern is very recognizable. At 60 s, the network is in a stable state with post-synaptic neurons firing at a constant rate, as the un-correlated neurons are completely depressed and thus not contributing any current to the LIF circuit of the post-synaptic neuron. Figure 0.8 (c) shows the synaptic weight distribution of the memristor and a decrease in the weight of the uncorrelated synapses can be noted at 30 s.

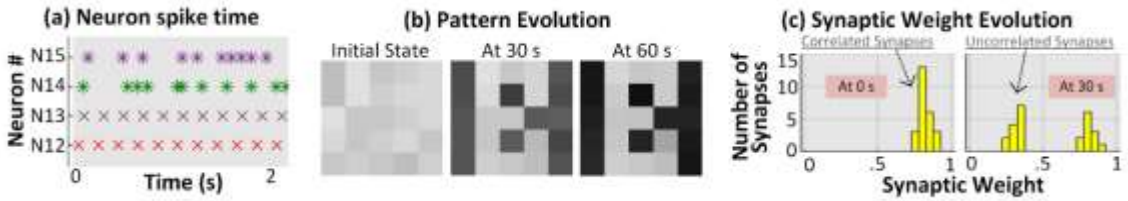

Figure 0.8 (a) Scatter plot of the spike times of two correlated afferents N12 and N13 (participating in the pattern) and two non-participating, uncorrelated afferents (N14 and N15). (b) The initial synaptic weight distribution and evolution of the pattern over time as the system is in the process of learning a 25-pixel letter 'B'. (c) A histogram of the synaptic weight distributions in weight bins that are 0.05 wide. After 30 s, uncorrelated neurons are separated and moved to a lower weight.

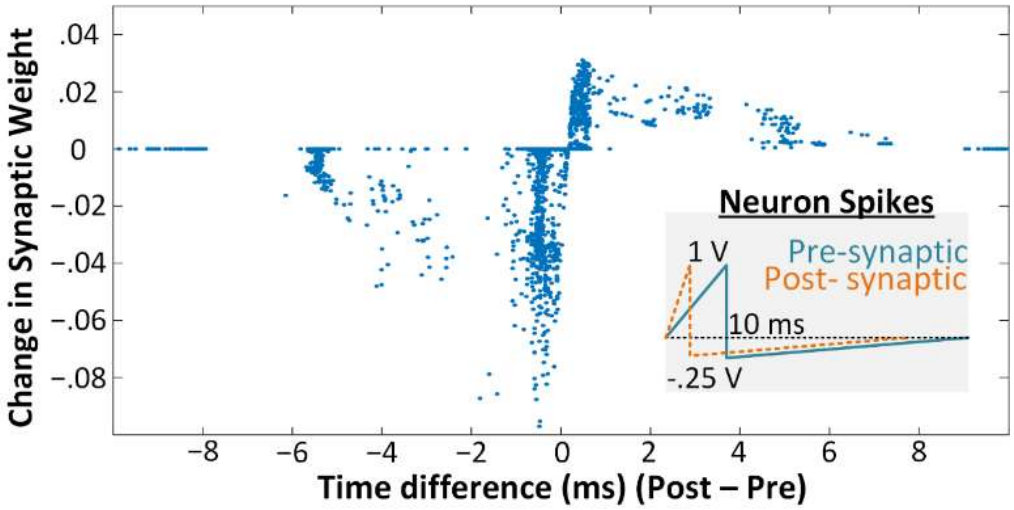

Figure 0.9 STDP plot obtained from weight changes due to nearest-neighbor pairs in the 100 s simulation of the network with 25 pre-synaptic biphasic spiking neurons of Figure 0.3. Inset shows the pre- and post-synaptic neuron inputs used. STDP has much stronger depression than potentiation, generally leading to faster learning in the network.

The STDP learning curve in Figure 0.9 shows changes in the synaptic weights of all 25 memristors for 100 s as a function of the time difference between post- and pre-synaptic spike firing. When a post-synaptic neuron fires after a pre-synaptic neuron (time difference > 0 ms), the network considers them correlated and the synaptic weight of the respective memristor increases, making the synaptic connection more conductive (and vice-versa). The STDP curve shows much stronger depression than potentiation, meaning

the network can depress the uncorrelated afferents faster. Asymmetrical STDP curves are obtained using different potentiation for pre- and post-synaptic spikes, as shown in the inset in Figure 0.9.

4.4 Conclusion

This chapter discussed the design, topology, and learning behavior of the memristor-based spiking neural networks, which are used in the next chapter to investigate radiation effects. The leaky integrate-and-fire (LIF) circuit that was used as a post-synaptic neuron in the spatio-temporal pattern learning neural network was discussed in detail. The pulsed neural network and the spiking neural network were discussed which were using the pair-based STDP learning rule.

Factors that affect the neural network's learning ability were discussed in this chapter. It was demonstrated that overall STDP was affected by multiple factors such as memristor threshold, input spike pulse shape, pulse width, and the initial conductive state of the network. STDP, in turn, affects the learning ability of the network. The number of afferents used in a network, LIF charging and discharging time constants, pre-synaptic pulse width, frequency, and amplitude are a few other factors that affected the network's learning ability.

CHAPTER 5: NEURAL NETWORK UNDER RADIATION

In this chapter, memristor-based spiking neural networks are used to analyze the effect of radiation on the spatio-temporal pattern recognition (STPR) capability of the networks. The radiation effects discussed in CHAPTER 3: are simulated on the memristor-based neural networks discussed in 0; the modified non-linear memristor drift model used is discussed in CHAPTER 2:. All the simulations are captured in Cadence Virtuoso Spectre.

Networks with 5, 25, and 50 neurons are simulated to observe the effect of radiation at different intensities, flux, and duration. The chapter starts by discussing the effects of state-altering radiation on the spike-timing-dependent plasticity (STDP) curve, thus observing the effects of radiation on the expected learning rule. In the pulsed neural network, in the absence of any pattern, the cumulative effect of radiation events is observed leading to an unstable network. Later sections of the chapter discuss the effects of radiation on the spatio-temporal pattern learning ability of the network. Changes in network learning capability and system stability are statistically analyzed as well. The contributions from this chapters are published in [120]–[122] and are under peer review.

5.1 Radiation and STDP

Figure 0.1 shows the test structure used to capture the spike-timing-dependent plasticity (STDP) curve. It is similar to the STDP test structure discussed in Section 0. The memristor is connected to a source of pre-synaptic and post-synaptic biphasic spikes which are 10 ms biphasic spikes arriving at different time intervals as shown in Figure 0.1 (a) and

(b). Due to this time difference, the memristor sees varying potential across it as shown in Figure 0.1 (c). As mentioned in Section 0, varying the potential in combination with the memristor threshold of 1 V leads to the desired STDP shape. In this case, state-altering radiation current at different magnitude is induced in the memristor before the arrival of the pre- and post-synaptic pulses, and the change in the synaptic state is noted. Radiation interaction leads to a change in the STDP curve.

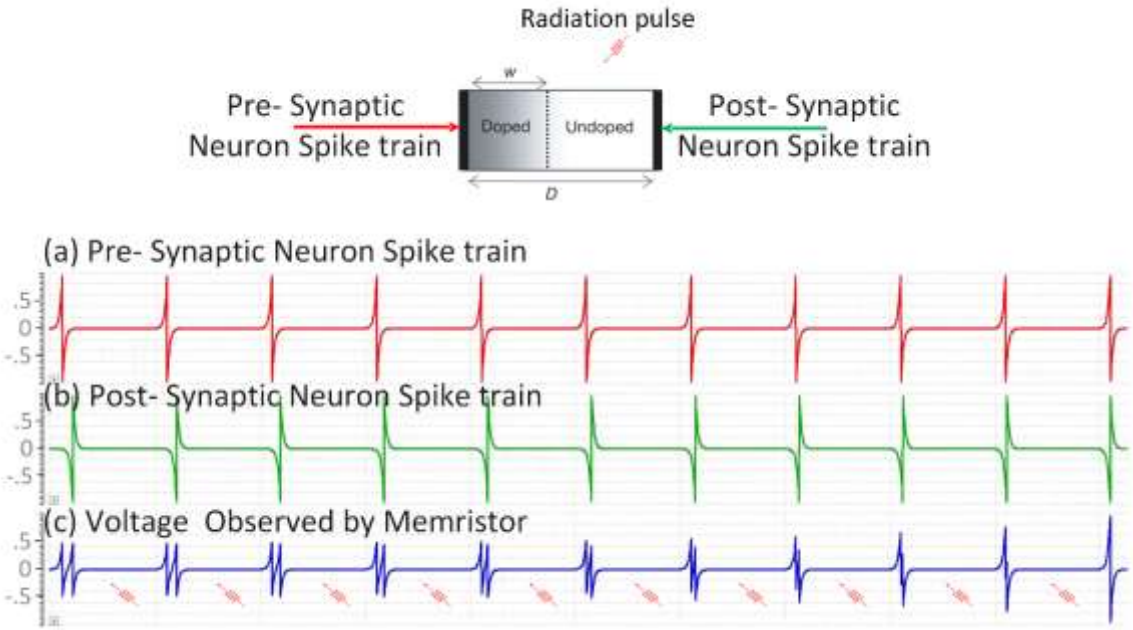

Figure 0.1 The two terminals of the memristor are connected to the pre- and post-synaptic neuron inputs. Spike trains in (a) show the pre-synaptic neuron spike produced and (b) show the post-synaptic neuron spike observed by the memristor terminal. Both are the same in magnitude and shape except there is a difference in their arrival times. Due to the difference in arrival time, the memristor observes the voltage given in (c) across it. Thus, the synaptic weight change would be different at each pre-post pairs' arrival, resulting in the changes to the STDP curve. The radiation effect is observed by the added radiation current pulse to the network before the pre-post pairs' arrival (marked by red arrows).

Figure 0.2 shows the change in the STDP learning curve as the memristive device is exposed to an event of state-altering radiation before the pre- and post-synaptic afferent biphasic pulses arrive. Figure 0.2 (a) shows the STDP curve resulting from the exponential

biphasic spike and Figure 0.2 (b) results from a triangular biphasic spike, as shown in their respective insets. Radiation is observed to shift the whole curve upward, making it asymmetric. Thus, the system will undesirably favor a stronger correlation and might make the system unstable. The STDP curve is noted at the varying intensities of the state-altering radiation current, the curve shifts more as the radiation intensity increases, indicating that the neural network will be overwhelmed at a higher magnitude of radiation current.

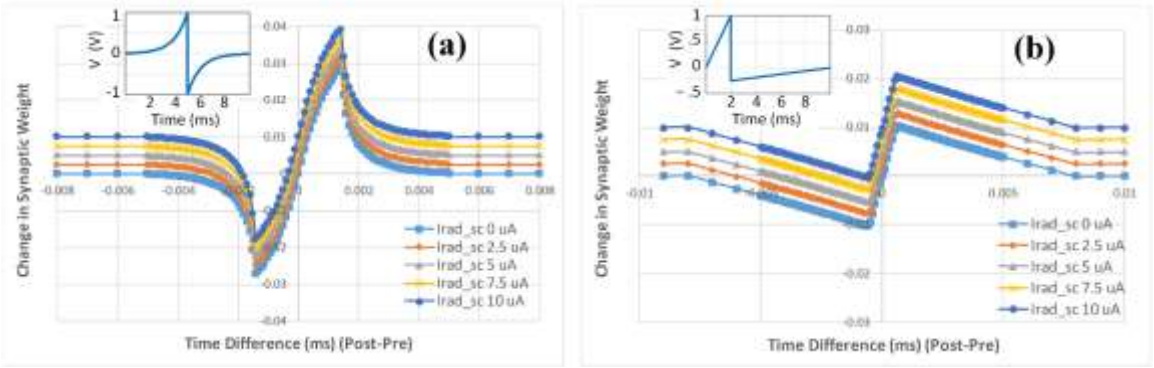

Figure 0.2 STDP plot after a state-altering radiation event for (a) exponential and (b) triangular biphasic pulses. The STDP curve shifts upward due to radiation that brings asymmetry into the STDP curve and thus tends to favor an increase in synaptic weight.

5.2 Radiation Effects on the Pulsed Neural Network: without a Pattern

This section discusses the effects of state-altering radiation current on a memristor-based pulsed neural network discussed in Section 0. The network is not in the process of learning any pattern. In this case, the pre-and post-synaptic neurons are not firing any specific pattern, the spikes just present randomly distributed Poisson noise.

The network shown in Figure 0.2 is used to study the effect of radiation events on the pulsed neural network. In Figure 0.2, N_1, N_2, and N_3 are pre-synaptic neurons (afferents) and N_4 and N_5 represent post-synaptic (output) afferents. Memristors (M_1 to M_6) in the network represent the synapses electrically connecting neurons, with the numbering

scheme shown in Figure 0.2. For simulation purposes, five independent voltage sources mimic the behavior of the neurons. Each voltage source generates 500 mV pulses such that the pulse interval follows the random Poisson distribution as shown in Figure 0.3 (a). Due to the presence of these pre- and post-synaptic voltage pulses, the state or weight ($\frac{w}{D}$) of all six memristive devices will changes interdependently, as shown in Figure 0.3 (b).

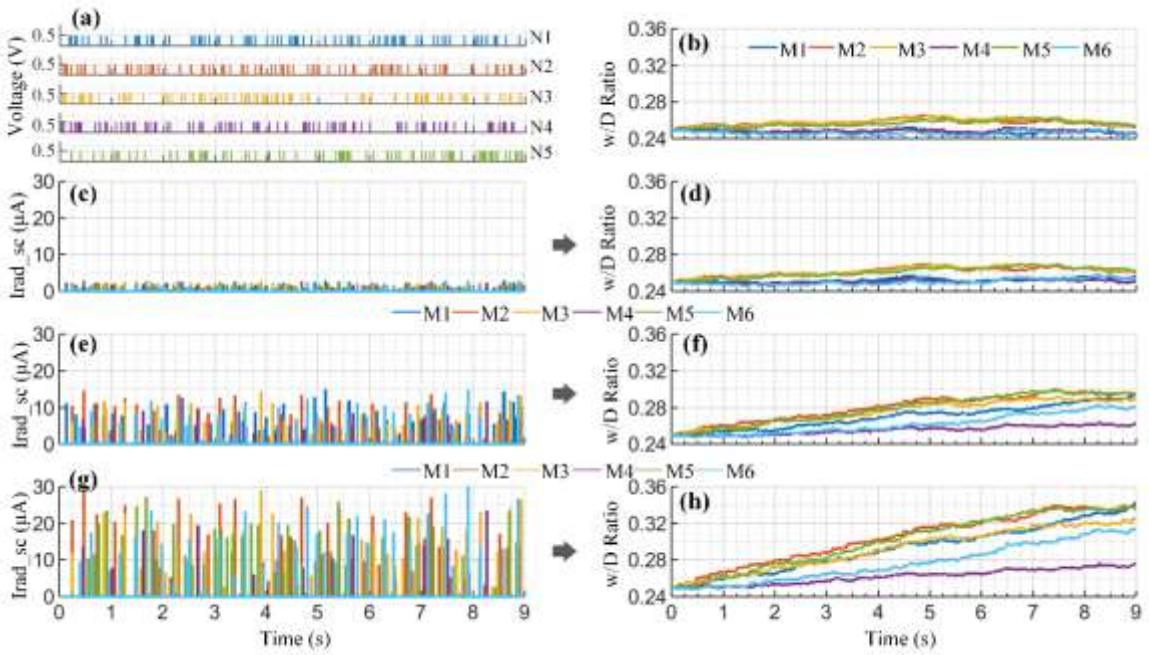

Figure 0.3 Simulation of the network in Figure 0.2 (a). Randomly Poisson distributed voltage pulses depicting the behavior of randomly spiking neurons. (b) Synaptic weight evolution with no radiation. The network is exposed to randomly Poisson (interval) and Gaussian (amplitude) distributed radiation events, and then the synaptic weight of each memristor is observed. (c) Low radiation, μ = 1.5 μA, and σ = 0.75 μA. (d) Low radiation increased the weights, making the devices more resistive. (e) Medium radiation, μ = 7.5 μA, and σ = 3.75 μA. (f) Medium radiation increases the weights further and (g) higher radiation, μ = 15 μA, and σ = 7.5 μA. (h) At higher radiation levels the neuromorphic effect is almost negligible and the radiation events drive the weights considerably higher, making the devices more conductive.

Each synaptic memristive device is exposed to a different state-altering radiation pattern. The radiation current $Irad_{sc}$ pulse interval follows the random Poisson's distribution and the magnitude follows the random Gaussian distribution with mean μ and

standard deviation σ. Figure 0.3 (c), (e) and (g) represent the radiation pattern used on the memristors, but at different intensities. These radiation events follow the same pattern, but their mean is 1.5 μA, 7.5 μA, and 15 μA and the standard deviation is 0.75 μA, 3.75 μA and 7.5 μA for Figure 0.3 (c), (e) and (g) respectively. Plots in Figure 0.3 (d), (f), and (h) respectively represent the resulting weights of the memristor during the three radiation events.

It is noted that at the stronger radiation flux, the synaptic weights deviate farther away from their ideal values, making synapses more and more conductive. In Figure 0.3 (g) stronger radiation almost overtakes the effect of the input from the neurons, contrary to the Figure 0.3 (d) effect which saw much less intense radiation flux, and thus still follows the input of the neuron with much less deviation. For an expected memristor device size of 100 nm x 100 nm, the radiation flux in this example is $4.685 \times 10^{10}\ cm^{-2}\ s^{-1}$. This is a large value, but certainly, one that is observable in many different situations.

Figure 0.4 represents the simulation results obtained using the same fully connected pulsed neural network shown in Figure 0.2. Each afferent in the network generates a train of 500 mV (1 ms) square pulses at Poisson distributed interspike intervals representing pure noise (no patterns or correlations). The system is also irradiated for the first 10 s with state-altering radiation of different magnitude (μ = 1 μA to 100 μA, and σ = 0.5 μA to 50 μA) and flux (up to $5x10^{10}\ cm^{-2}s^{-1}$). Figure 0.4 plots the $\frac{w}{D}$ of each memristor (M_1 to M_6) after 50 s of simulation. Although the system is irradiated only for the first 10 s, the radiation effects accumulate over time, and at higher radiation intensity, the weights have considerably diverted. Some will even saturate, as is the case of M_4, M_5, and M_6 at the

higher flux of $5x10^{10}$ $cm^{-2}s^{-1}$. This cumulating behavior of the effect of radiation could lead to pattern learning and recognition challenges in neural networks [120].

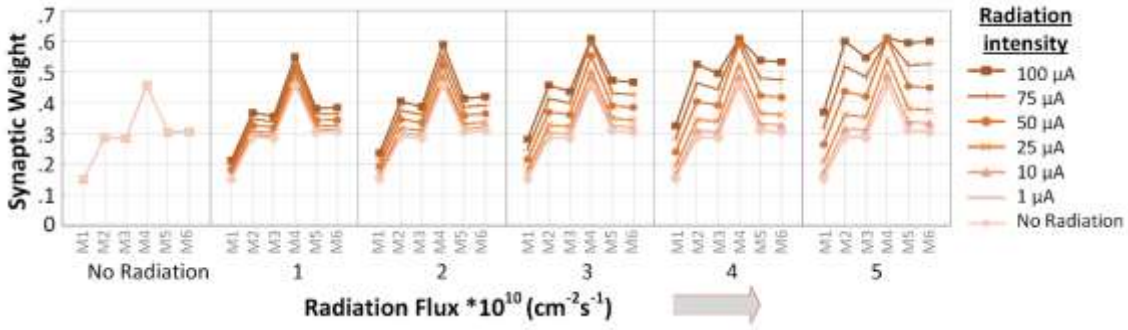

Figure 0.4 The synaptic weight ($\frac{w}{D}$) of memristor (M_1 to M_6) of the fully connected pulsed neural network represented in Figure 0.2. The network is simulated using 0.5 V, 1 ms square pulses, radiated for 10 s with state-altering radiation of different mean magnitude and flux, with $\frac{w}{D}$ values noted after 50 s of simulation. The radiation effects seem to accumulate over time, especially from stronger radiation events.

5.3 Radiation Effects on the Spiking Neural Network: with a Pattern

This section discusses the effects of state-altering radiation current on a memristor-based neural network, which is in the process of learning a pattern. In this case, few of the pre-synaptic neurons that are firing at specific intervals are part of the given pattern. On the other hand, the pre-synaptic neurons that are not part of the pattern present randomly distributed Poisson noise.

The network shown in Figure 0.3 is used to study the effect of radiation in this section. In Figure 0.3, N_1 to $N_{25/100}$ are pre-synaptic afferents and the post-synaptic afferent is represented by a leaky integrator circuit, as noted in Section 0. Memristors (M_1 to $M_{25/100}$) in the circuit represent the synapses electrically connecting the pre-synaptic neurons with the post-synaptic LIF neuron. For simulation purposes, voltage sources mimic the behavior of the pre-synaptic afferents generating biphasic spikes.

5.3.1 Subjected to Radiation with Limited Duration

In this section, the memristor-based neural network that has partially learned the pattern is exposed to the state-altering radiation for a limited duration such as 10 to 40 s. The network's ability to keep learning or recovering the pattern post radiation is analyzed.

5.3.1.1 Changing the flux of radiation exposure

Figure 0.5 shows the change in the state of the 25-memristive devices in the neural network. The network is exposed to the state-altering radiation for 10 s after 30 s of learning the pattern representing the 25-pixel letter 'B'. The memristors were exposed to radiation flux of (b) $1x10^{10}$ $cm^{-2}s^{-1}$, (c) $3x10^{10}$ $cm^{-2}s^{-1}$ and (d) $5x10^{10}$ $cm^{-2}s^{-1}$ at a magnitude $\mu = 25$ μA and $\sigma = 12.5$ μA for 10 s.

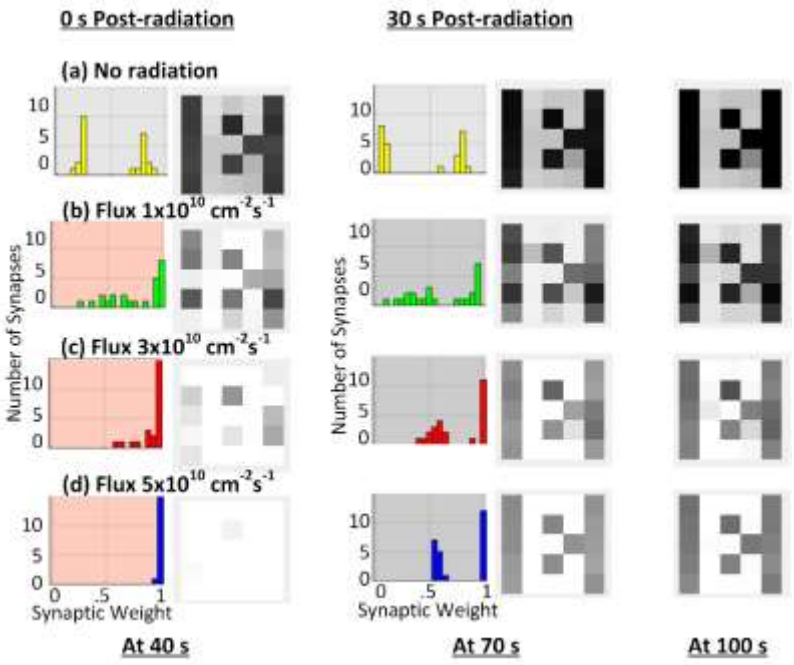

Figure 0.5 Memristors were exposed to 10 s of state-altering radiation (magnitude of 50 μA) at different flux after 30 s of learning is complete. As the flux increased, the pattern distorts and more saturation was observed in (d) at 40 s. The network was able to resolve the pattern but took a long time to stabilize at higher flux.

In Figure 0.5, the synaptic weight distribution is recorded right at the end of the radiation events (at 40 s) and at 70 s and 100 s as learning continued. It is observed that as the flux increases to $5x10^{10}$ $cm^{-2}s^{-1}$, the pattern completely disappears (at 0 s post-radiation). As pattern learning continues after the end of radiation, the system was able to relearn the pattern even in the case of intense radiation flux (Figure 0.5 (d)). Although it did take much longer for the system to depress the non-participating afferents, the difference in synaptic weight distribution can be noted at 70 s and 100 s. At the end of the radiation events (at 40 s) most of the synaptic weight seems to be biased towards $\frac{w}{D} = 1$ (more in Figure 0.5 (d) than Figure 0.5 (b)) but as learning progresses at 70 s and 100 s the network was successfully able to depress the non-participating afferents and the system stabilizes again.

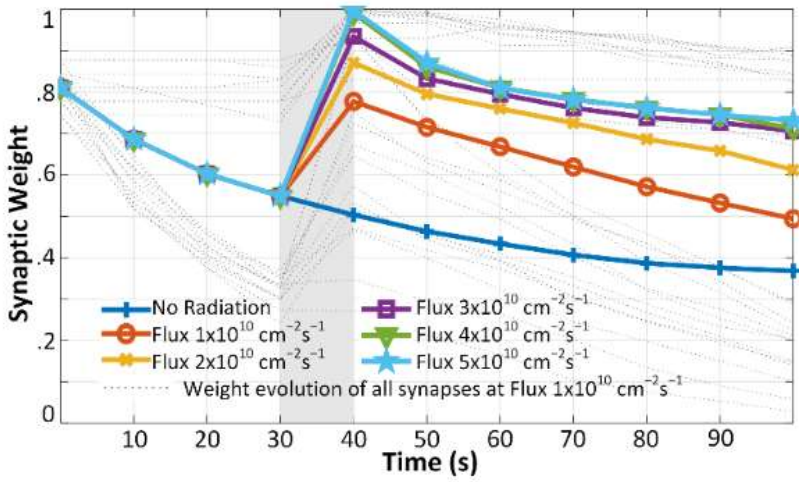

Figure 0.6 Evolution of the average synaptic-weight of all memristors at different flux. The network was exposed to state-altering radiation (magnitude 50 μA) for 10 s (grey area) after 30 s of learning. Post-radiation weights evolve toward the non-radiated weight curve as the network tries to resolve the pattern.

The evolution of the average synaptic weight of all 25 memristors is plotted in Figure 0.6. the simulated irradiation of the system for 10 s starts at 30 s (grey region) at different flux with a mean magnitude $\mu = 25$ μA and $\sigma = 12.5$ μA. As expected, during the

radiation events, the weights were climbing towards $\frac{w}{D} = 1$. At higher flux of $5x10^{10}\,cm^{-2}s^{-1}$, all weights saturate post-radiation and the network is unable to recognize the pattern, as seen in Figure 0.5 (d) at 40 s. At the end of radiation at 40 s, the mean weights start to evolve towards the non-radiated trace as the network tries to relearn the pattern. This indicates that the system is stabilizing itself by decreasing the average conductivity of the network, which was artificially increased due to the state-altering radiation event.

Figure 0.7 shows the synaptic weight distribution and pattern evolution, as the spiking neural network is in the process of learning a 100-pixel spatio-temporal pattern letter 'B'. Again, the network is exposed to 10 s of state-altering radiation (magnitude μ = 25 μA and σ = 12.5 μA, starting at 30 s) at increasing flux.

It is observed that as the flux increases, the pattern distortion also increases. This is because radiation is changing the state of the memristive synaptic devices and forcing them to be more conducive, as indicated by the STDP curve in Section 0. As the weights move toward more conductive states, the LIF post-synaptic neuron observes a stronger correlation and the system becomes unstable. For a neural network to be stable, synaptic weight distributions should look more like Figure 0.7 (a) at 100 s, where the correlated weights are not completely saturated and therefore not over-simulating the LIF post-synaptic neurons, but contributing to the pattern.

At 40 s, after the end of the 10 s state-altering radiation event, the system tries to relearn the pattern, but the recovery does not necessarily result in the same pattern or a stable system. In the case of Figure 0.7 (d), at $5x10^{10}$ $cm^{-2}s^{-1}$ at 40 s, the pattern is indistinguishable and post-radiation recovery left the system with a slightly different pattern and a relatively unstable synaptic weight balance.

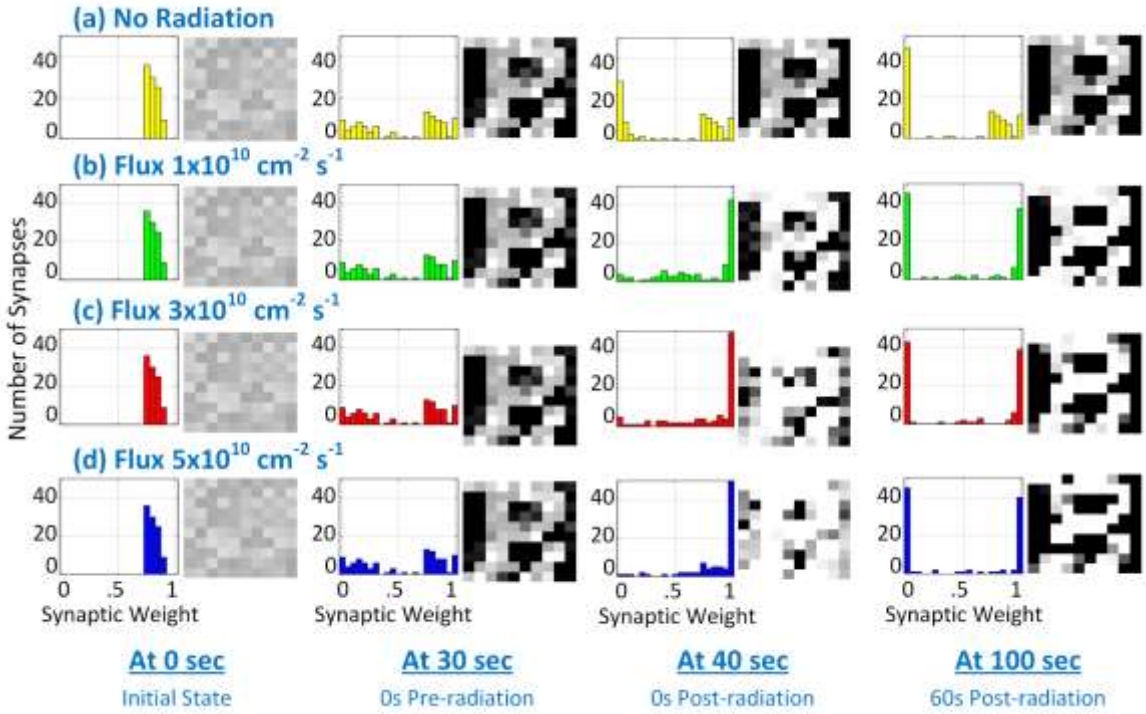

Figure 0.7 The synaptic weight distribution and pattern evolution over time as the system is exposed to 10 s (starting at 30 s) state-altering radiation (magnitude μ = 25 μA and σ = 12.5 μA) at increasing flux. The spiking neural network is in the process of learning a 100-pixel spatio-temporal pattern letter 'B'. As the flux increases, pattern distortion also increases. At $5x10^{10}$ $cm^{-2}s^{-1}$ flux, the pattern is completely indistinguishable at 40 s. Although the system tries to relearn the pattern after the end of radiation exposure, the recovery does not result in the same pattern or a stable system.

Figure 0.8 shows a detailed analysis of data obtained from the 100 pre-synaptic neuron network simulation. Figure 0.8 (a) plots the average synaptic weight evolution of all correlated and uncorrelated synapses separately over the 100 s period. During the radiation event (salmon color), uncorrelated synapses saw more deviation than correlated synapses. This effect is due to the non-linearity of the device as discussed in Section 0 and Figure 2.4. When it is less conductive, there is a larger change in synaptic weight compared to a highly conductive state.

It is also observed that the system became stable only after the average weight (calculated using Equation (0.1)) of the uncorrelated afferents slid lower than 0.1 $\frac{w}{D}$ (note

dashed vertical lines in Figure 0.8 (a)). Due to this, all the correlated synapses do not average out at the same value and result in a slightly different pattern as noted in Figure 0.7 at 100 s. This observation is clearer in Figure 0.8 (b) where the cumulative variance (calculated using the Equation (0.2)) in a change of synaptic weight of correlated synapses stabilized after the vertical dashed lines confirming the system stability. As expected, the cumulative variance in weight change is higher for uncorrelated synapses at higher flux.

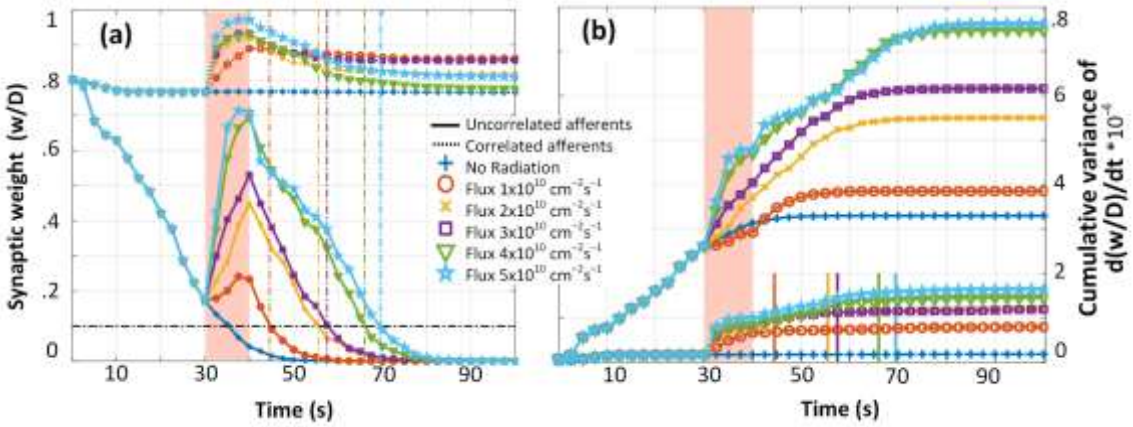

Figure 0.8 Network stability analysis of the simulation in Figure 0.7. (a) Average and (b) Cumulative variance in the change of synaptic weight evolution of all correlated and uncorrelated synapses over 100 s period. In (a) during the radiation event (salmon color), uncorrelated synapses saw more deviation than correlated synapses and the system became stable only after the average weight of uncorrelated afferent slid lower than 0.1 value of $\frac{w}{D}$ (dashed vertical lines). This observation can be made more clearly in (b) where the cumulative variance in synaptic weight of correlated synapses stabilized after the vertical dashed lines.

The formulas used in the calculations are given as:

$$\text{Average weight}(n) = \frac{1}{n}\sum_{i=1}^{n}\left(\left(\frac{w}{D}\right)_i\right) \tag{0.1}$$

$$\text{Cumulative Variance of } \frac{d\left(\frac{w}{D}\right)}{dt}(n) = \sum_{i=1}^{n}\left(\left|\left(\frac{w}{D}\right)_i - (p)_i\right|\right) \tag{0.2}$$

$$\text{Mean Squared Error (n)} = \frac{1}{n}\sum_{i=1}^{n}\left(\left(\frac{w}{D}\right)_i - (p)_i\right)^2 \quad \textbf{(0.3)}$$

where n is the total number of synaptic memristors under analysis (uncorrelated, correlated or all) and p is the desired weight of the corresponding synaptic device.

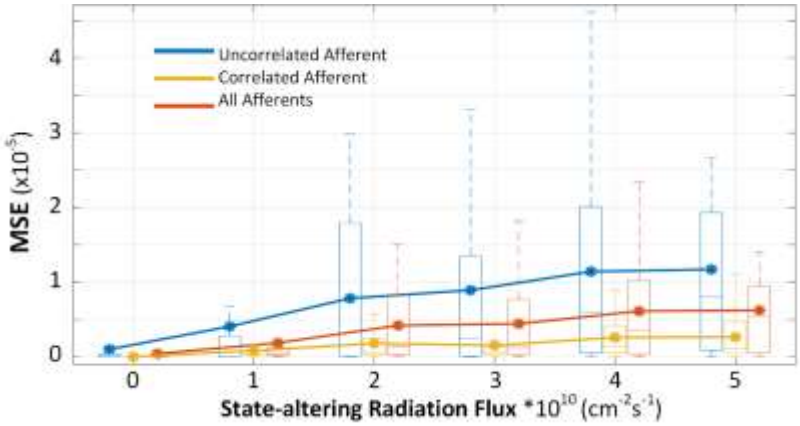

Figure 0.9 Error analysis of the network from the simulation in Figure 0.7. Box plot of mean squared error post-radiation (after 40 s) of uncorrelated, correlated, and all synaptic weights. Note the increase in the average MSE and spread, as the radiation flux increases. The spread is more notable in uncorrelated synapses.

A box plot of mean squared error (MSE) of the post-radiation data (after 40 s) obtained from the same memristor-based 100 pre-synaptic Neuron network simulation is plotted in Figure 0.9. The MSE is calculated using Equation (0.3). The plot presents the simulations at different radiation flux for the synaptic weight of uncorrelated, correlated, and all memristors (M_1 to M_{100}). As expected, the average MSE increases as the radiation increases, and the box-whisker spread are significantly noticeable in the uncorrelated data set because it saw the most deviation during radiation, as seen in Figure 0.8 (a). Notably, the median of the radiated correlated data set is much closer to zero because this data set did not see much deviation during radiation due to the STDP $\frac{w}{D}$ non-linearity.

5.3.1.2 Changing the duration of radiation exposure

Figure 0.10 represents the behavior of the 25 pre-synaptic neurons neural network when irradiated for a longer period (20 s and 40 s, starting at time 30 s) with Gaussian distributed pulses of average magnitude $\mu = 5$ μA and $\sigma = 2.5$ μA at $3x10^{10}$ $cm^{-2}s^{-1}$ flux. The weight distribution was recorded right at the end of radiation events (at 50 s/70 s) and after 30 s (at 80 s/100 s).

Figure 0.5 (d) at 40 s shows more distortion in the pattern than Figure 0.10 (c) at 70 s even though Figure 0.10 (c) saw a longer period of exposure. That distortion is due to the lower flux radiation used in Figure 0.10 (c) simulation. Thus, the network depressed the synapses and relearned the pattern more rapidly.

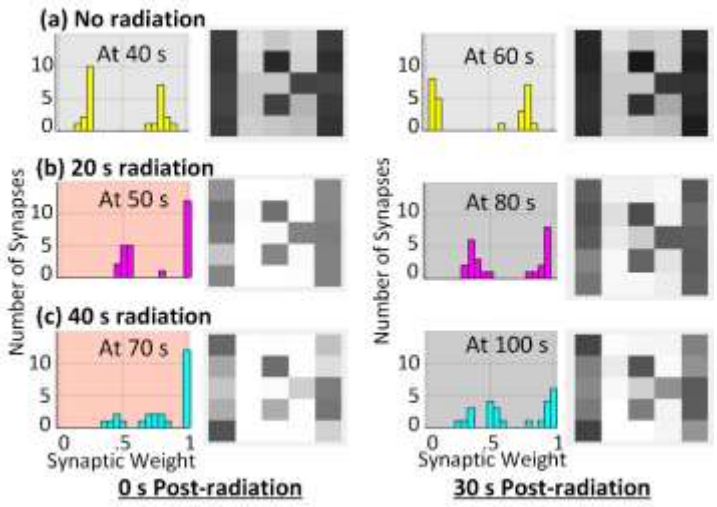

Figure 0.10 The left column shows the synaptic weight distribution after the end of the state-altering radiation event ($3x10^{10}$ $cm^{-2}s^{-1}$ flux, magnitude $\mu = 5$ μA and $\sigma = 2.5$ μA) for (b) 20 s and (c) 40 s, after 30 s of uninterrupted learning. The right column shows the weight distribution 30 s after the end of radiation. In (c), the network is still in an early stage of learning as radiation effects accumulated over time and delay the learning process.

Figure 0.11 plots the evolution of average synaptic weight when the system is irradiated for longer periods (colored region) with pulse magnitude $\mu = 5$ μA and $\sigma = 2.5$

μA each at $3x10^{10}$ $cm^{-2}s^{-1}$ flux. After the end of the radiation events, the mean weights start to evolve towards the non-irradiated trace. Even when exposed to radiation for 40 s, the weights do not saturate, unlike the effect observed in Figure 0.5 at higher flux. Once again representing the ability of the continually evolving and learning neural network to recover from the lower intensity and flux radiation.

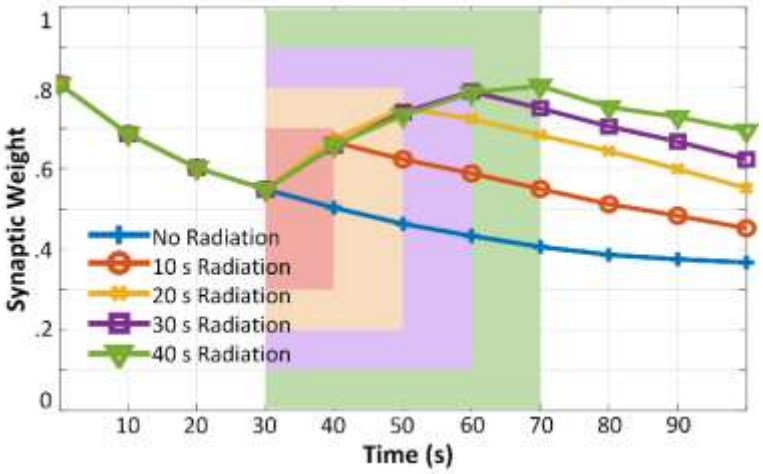

Figure 0.11 Average synaptic-weight evolution of all memristors as state-altering radiation ($3x10^{10}$ $cm^{-2}s^{-1}$ flux, magnitude μ = 5 μA and σ = 2.5 μA) time increases from 10 s to 40 s (colored area). After the end of the radiation event as the network tries to relearn the pattern, the average synaptic weight of radiated memristors evolves towards the non-radiated weight curve.

5.3.2 Learning in the Presence of Constant Radiation

The simulation results shown in this section demonstrate the learning ability and the average synaptic weight evolution of the network in the presence of radiation of pulse magnitude μ = 0.5 μA and σ = 0.25 μA at different flux intensities. In these cases, radiation events started at 0 s when the network weight distribution was in its initial state as seen in Figure 0.8 (b). The goal of this experiment was to determine if the network can learn a pattern at all in the presence of radiation, or whether the weight evolutions are inevitably altered.

Figure 0.12 shows that until 40 s there was no major disruption in the network's ability to learn the pattern. Figure 0.12 (b) at a lower flux of $1x10^{10}$ $cm^{-2}s^{-1}$ shows no change in the pattern recognition capability of the network at 100 s. It can be observed from Figure 0.12 (c, d, and e) that as radiation flux increases, the network quickly becomes unstable sooner as radiation accumulates. It is interesting to note that in both Figure 0.12 (d) and Figure 0.12 (e), the network consistently and stably starts recognizing a different pattern again at 80 s (several pixels are incorrect).

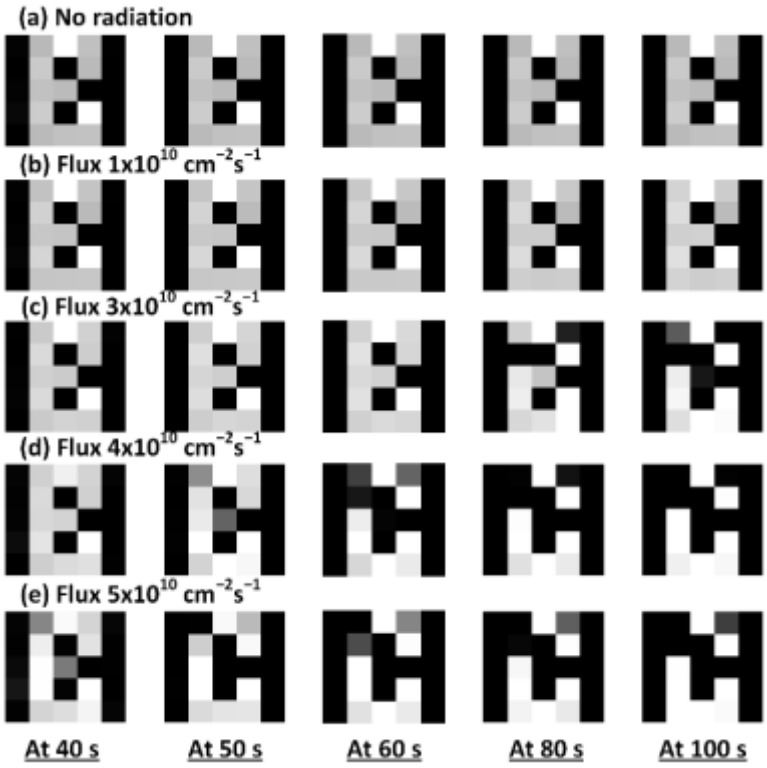

Figure 0.12 Memristors were exposed to state-altering radiation (flux magnitude μ = 0.5 μA and σ = 0.25 μA) throughout the learning process (for 100 s starting at 0 s). In each case, the network was able to resolve the pattern in 40 s. Although, at higher flux (c), (d), and (e), the network became unstable at 80 s, 60 s, and 50 s. The network maintained stability in (b) at the lower flux value.

A similar evolution can be noted in Figure 0.13, which plots the total average weight (calculated using Equation (0.1)) of all the synapses versus time. In this plot, the

weight evolution is similar until the flux reaches over $1x10^{10}$ $cm^{-2}s^{-1}$. Here, the flux weight evolution is similar to the no radiation curve, but higher flux causes a sudden decrease in total weight after 70 s, 50 s, and 40 s in the case of $3x10^{10}$ $cm^{-2}s^{-1}$, $4x10^{10}$ $cm^{-2}s^{-1}$, and $5x10^{10}$ $cm^{-2}s^{-1}$ state-altering radiation flux. As observed in Figure 0.12 (d) and (e), Figure 0.13 also notes the stable evolution of weight after 70 s in both cases when the flux is at $4x10^{10}$ $cm^{-2}s^{-1}$, and $5x10^{10}$ $cm^{-2}s^{-1}$.

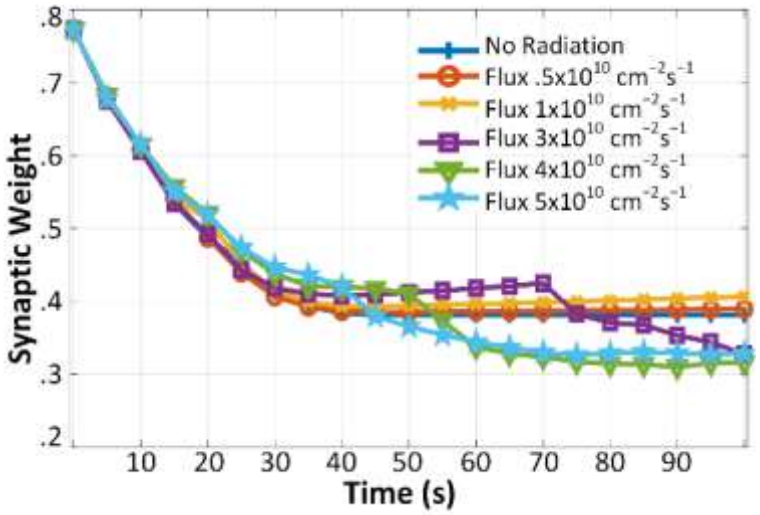

Figure 0.13 The average synaptic-weight evolution of all memristors as the network tries to learn the pattern in presence of state-altering radiation (for 100 s starting at 0 s) at different flux (pulse magnitude with μ = 0.5 μA and σ = 0.25 μA). The network tries to resolve the pattern but becomes unstable sooner as the flux increases. At a lower flux network was successfully able to recognize the pattern throughout the time.

Figure 0.14 shows the synaptic weight distribution and pattern evolution, as the spiking neural network is the process of learning the 100-pixel spatio-temporal pattern letter 'B'. The network is exposed to state-altering radiation (magnitude μ = 0.5 μA and σ = 0.25 μA) at increasing flux up to $5x10^{10}$ $cm^{-2}s^{-1}$ throughout the learning process of 100 s. It can be noted in Figure 0.14 at $5x10^{10}$ $cm^{-2}s^{-1}$ flux at 100 s, correlated weights are pushed to the extreme, $\frac{w}{D} = 1$. Thus, LIF post-synaptic neuron starts over firing and the

system becomes unstable and does not recognize the expected pattern. On the other hand, at $0.5x10^{10}$ $cm^{-2}s^{-1}$ flux, the system is very stable as the correlated weights are not saturated (LIF post-synaptic neuron is not over-stimulated) and the changes due to radiation are absorbed by the network.

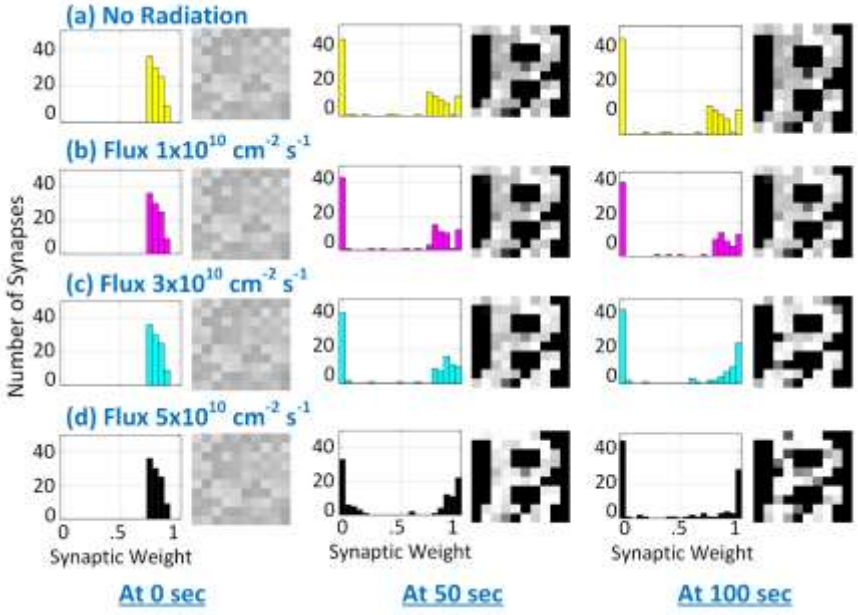

Figure 0.14 Synaptic weight distribution and pattern evolution over time as the system is exposed to state-altering radiation (magnitude μ = 0.5 μA and σ = 0.25 μA) at increasing flux throughout the learning process of 100 s. The spiking neural network is in the process of learning a 100-pixel spatio-temporal pattern letter 'B'. As the flux increases, the system instability increases but at lower flux, the system was able to maintain stability.

Figure 0.15 shows the detailed analysis of data obtained from the network simulation shown in Figure 0.14. Figure 0.15 (a) plots the average synaptic weight evolution of all correlated synapses over the 100 s period. At higher radiation, a deflection point can be observed (represented by the dotted horizontal black line). As the average correlated synaptic weight evolves to this point, the system becomes unstable. This observation can also be verified when the cumulative variance (calculated using Equation (0.2)) in the change of synaptic weight of the correlated afferent is plotted in Figure 0.15

(a). Note that the cumulative variance in weight keeps increasing after the deflection-point even though the system was relatively stable for flux $3x10^{10}$ $cm^{-2}s^{-1}$ and $4x10^{10}$ $cm^{-2}s^{-1}$ before the deflection.

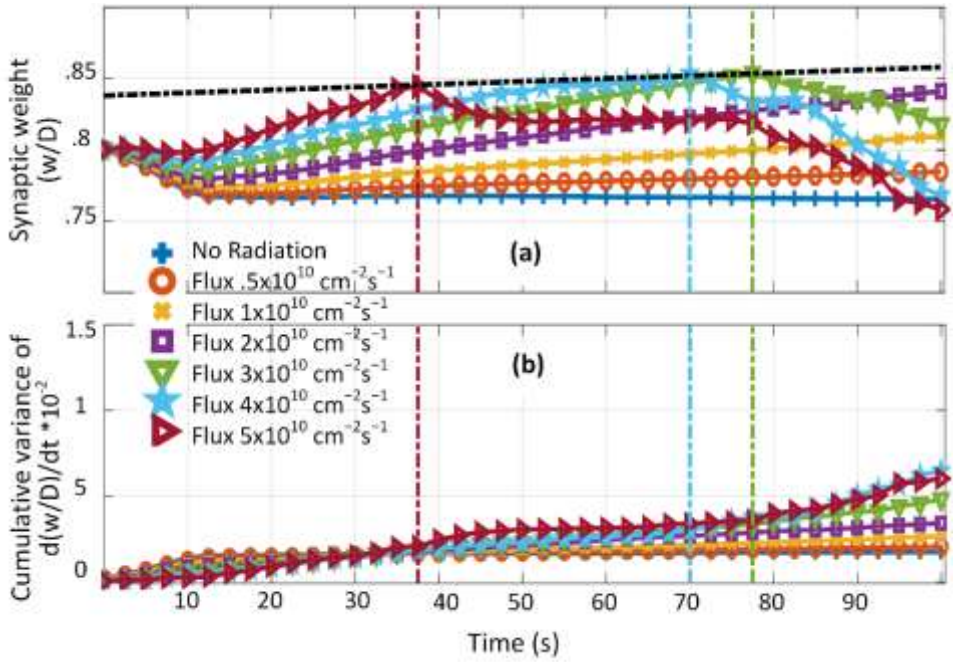

Figure 0.15 Stability analysis of simulated data captured in Figure 0.14. (a) Average synaptic weight and (b) Cumulative variance in the change of the synaptic weight of correlated synapses over 100 s period. In (a) at higher radiation, a deflection point can be observed around $\frac{w}{D} = 0.84$, represented by the dotted horizontal black line, where the system becomes unstable. This observation is clearer in (b) where the cumulative variance in weight of correlated synapses destabilizes after the vertical dashed lines representing the respective deflection-points.

The MSE of $\frac{w}{D}$ data obtained from the network simulation in Figure 0.14 is plotted in Figure 0.16 at different radiation flux for synaptic weights of uncorrelated, correlated, and all memristors. Figure 0.16 plots the evolution of MSE overtime calculated using Equation (0.3). As discussed in Section 0, all synapses are initialized to a high conductance, thus the uncorrelated synapses (Figure 0.16 (a)) started with the most error (MSE = 0.7) and as the network suppressed them the MSE approached zero. On the other hand,

correlated synapses (Figure 0.16 (c)) started with nearly zero MSE that increased over time as the system depressed and potentiated a few of the correlated synapses to attain stability. On average (Figure 0.16 (b)), MSE decreased from 0.35 to 0.5 stably at lower radiation flux. On the other hand, as radiation flux increased, correlated synapses became unstable and MSE increased (Figure 0.16 (c)).

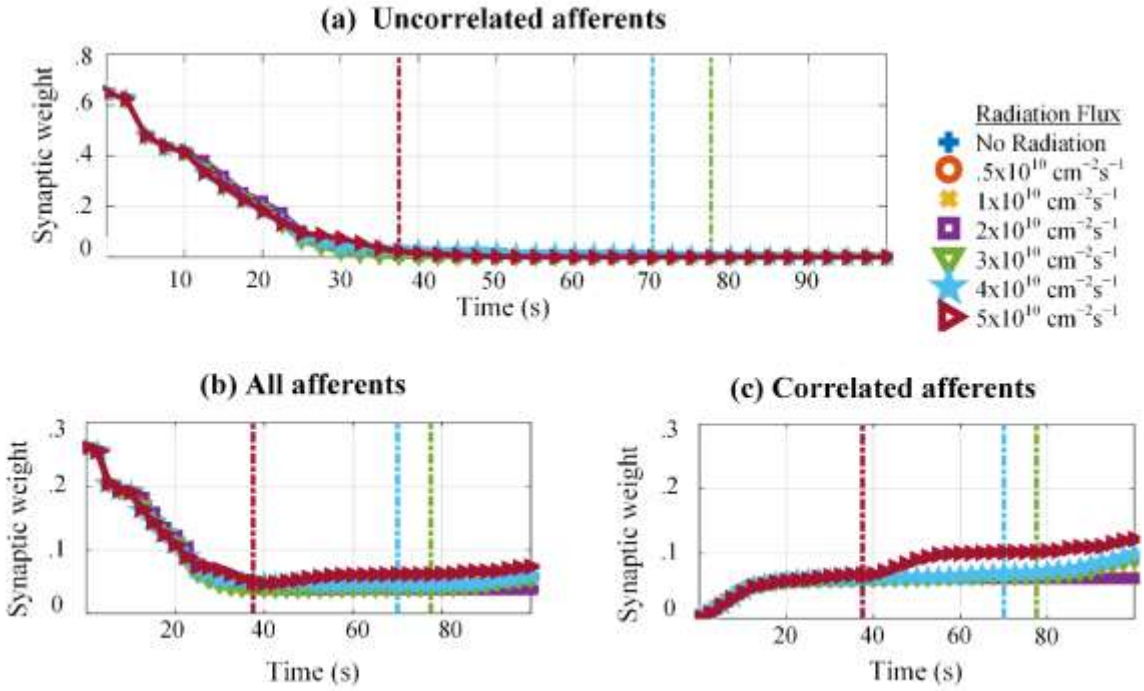

Figure 0.16 Mean Squared Error (MSE) analysis of network from the simulated data captured in Figure 0.14. MSE of (a) uncorrelated afferents, (b) all afferents, and (c) correlated afferents that are part of the pattern. On average MSE decreases at lower radiation flux but as radiation flux increases correlated synapses became unstable and MSE increases.

Figure 0.17 compares the distribution of MSE as the state-altering radiation flux increases from no radiation to $5x10^{10}$ $cm^{-2}s^{-1}$. As expected, the MSE increases as the radiation increases, and the box-whisker spread is significantly noticeable at $4x10^{10}$ $cm^{-2}s^{-1}$ and $5x10^{10}$ $cm^{-2}s^{-1}$ as the system becomes more unstable due to weight saturation and LIF over-simulation. Notably, the mean of the radiated correlated data set is almost stable until

$3x10^{10}$ $cm^{-2}s^{-1}$, meaning the system was able to absorb the effects of radiation for 100 s until that flux.

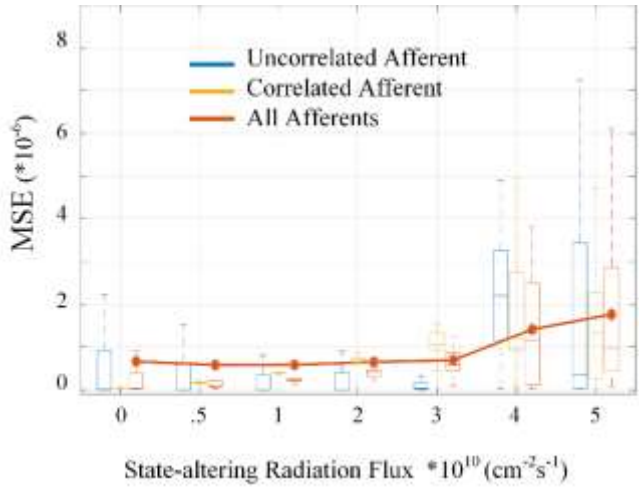

Figure 0.17 Box plot of MSE for 100 s of uncorrelated, correlated, and all synaptic weights of the network from the simulated data captured in Figure 0.14. Note the average MSE does not increase for the lower flux and the spread increases only at much higher radiation flux.

5.4 Conclusion

In this chapter, networks with 5, 25, and 100 neurons were simulated to observe the effect of radiation in different conditions like intensity, flux, and period. Although networks with only one or a few output neurons and two layers are not generally useful, the results are broadly relevant. In particular, these results can provide insight into the operation and response of filters within hidden layers of deep convolutional neural networks to radiation [169].

It was observed that radiation events bring asymmetry to the STDP curve, artificially forcing the network to favor a stronger correlation between the afferents. If the network was exposed to higher state-altering radiation flux, $4x10^{10}$ $cm^{-2}s^{-1}$, or $5x10^{10}$ $cm^{-2}s^{-1}$ for example, even for a shorter period such as 10 s, the network destabilized and

took a long time to stabilize and relearn the pattern. In such cases, the system suppressed a few of the correlated synapses, thus resulting in a slightly different learned pattern. When exposed to smaller flux ($1x10^{10}$ $cm^{-2}s^{-1}$), the system was very quickly (within 20 to 30 s) able to relearn the expected pattern and cope with the effect of radiation. In the absence of a pattern (input is random Poisson noise), radiation effects accumulate over time and the network was never able to overcome them. At the same time, the system was able to learn and separate the uncorrelated afferents when a pattern was presented but the network was subjected to state-altering radiation at low flux.

Thus, the primary result was that when the network was not undergoing training, the effects of radiation build up because the deposited energy was not dissipated and the network becomes less stable. On the other hand, the network could overcome larger amounts of radiation exposure when undergoing continuous on-line training.

CHAPTER 6: NEURON DEATH IN SPIKING NEURAL NETWORKS

Neuron death occurs in biological neural networks (the brain) due to various reasons like aging, natural death during migration and differentiation, head injuries, spinal cord injuries, or neurodegenerative diseases. The cognitive function of the human brain gradually declines with age, leading to memory loss, learning slowdown, motor incoordination, and attention impairment [170], [171]. Neurodegenerative diseases also cause a considerable decline in neuron numbers. Parkinson's and Huntington's diseases lead to neuron death in the basal ganglia region of the brain and Alzheimer's affects the neurons in the neocortex and the hippocampus parts of the brain [170], [172], [173]. It generally takes about 60 years before people notice any measurable memory loss or become susceptible to develop neurodegenerative diseases [172]. Thus, the human brain demonstrates a remarkable ability to compensate for neuron losses over time, forestalling any noticeable effect until the losses become profound [171], [174]. According to one study from 1998, about 11 million people in the US experienced a stroke, of whom only approximately 0.77 million (7%) were symptomatic [175]. A vast majority of strokes are 'silent', although they can kill large numbers of cells rapidly [175]. Presently, the network-level effects of neuron death in electronic circuits is not addressed in the literature. This chapter contributes to filling that gap in the neuromorphic computing literature by analyzing the effect of neuron death in spiking neural networks (SNNs).

Industry pioneers are implementing neural networks for solar radiation forecasting, object classification and matching, event filtering, facial recognition, combat automation,

target identification, and weapon optimization [11]–[15]. In the future, SNNs are expected to use pulses or spikes instead of analog signals to communicate and transfer information. Customized hardware implementations will make these spiking neural networks (SNNs) highly efficient, robust, and fault-tolerant. SNNs are expected to find applications in harsh, radiation-filled environments such as space or at nuclear and military installations. Presently, shielding and hardening are common practices to protect devices and circuits from radiation, but these techniques are unable to block all particles from interacting with underlying electronics [16], [17]. Radiation in such cases can lead to neuron death due to circuit failure (CMOS threshold shift, oxide breakdown, gate rupture, displacement damage [176], [177]) in the SNN.

In this chapter, a memristor-based SNN is designed to learn a spatio-temporal pattern. The changes in the learning ability of the networks due to the death of the neurons are analyzed. In the neural network, synapses are realized using a memristor behavioral model. Although the presented network uses a single layer, the results can provide insight into the operation and response of the hidden layers within deep convolutional neural networks [169].

Section 0 in the chapter discusses the SNN design and topology of the neural networks used. This section also discusses the experimental setup used to analyze neuron death. Section 0 details the results obtained from the simulations. Section 0 concludes the report and discusses the significance of the results and the future implications and applications of the work.

6.1 Simulating Neuron Death

The configuration of the network design used for simulations of neuron death is detailed in Section 0. Section 0 describes the experimental setup used to analyze neuron death.

6.1.1 Network Design

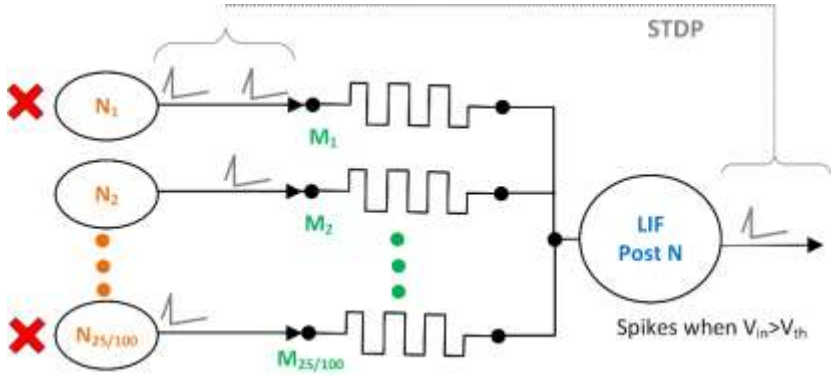

Figure 0.1 The memristor-based electronic Spiking Neural Network used in this work for spatio-temporal pattern recognition. 25 or 100 pre-synaptic neurons are connected to one post-synaptic leaky integrate-and-fire (LIF) neuron, each via a single memristor. The network uses biphasic shaped pulses to achieve pair-based STDP for pattern learning. Random neuron death is simulated by disconnecting pre-synaptic neurons after 30 s of partial learning.

The neural network shown in Figure 0.1 consists of multiple pre-synaptic neurons, a post-synaptic neuron, and memristive synapses, similar to one discussed in 0. The synapses act as the memory element and create a connection between the initial and the final layer of the network. This network mimics a single-layer perceptron network with 100 pre-synaptic afferents (N_1 to N_{100}), each connected to a single post-synaptic afferent via a single memristor (M_1 to M_{100}), (Figure 0.1). The network uses biphasic shaped pulses to achieve pair-based spike time-dependent plasticity (STDP) for pattern learning. Neuron death in the network is imitated by disabling pre-synaptic neurons randomly during the

learning process. The memristor design was discussed in CHAPTER 2: and the LIF post-synaptic neuron circuit design was discussed in 0.

6.1.2 Experimental Setup

The network analyzed in this chapter uses 100 pre-synaptic afferents, that have 60 participating/correlated (forming the part of letter B, brighter pixel, firing correlated spikes) and 40 non-participating/uncorrelated (not the part of letter B, darker pixel, firing uncorrelated spikes) afferents. Different percentages (up to 50%) of participating, non-participating, or random pre-synaptic neurons are turned off (killed) during the training to analyze the learning ability of the network.

In the initial setups, three neuron death cases are designed. The first case ("participating neuron dead") observes the changes in the pattern learning ability of the network when the random neurons that fail are all from the set of 60 participating neurons. The second ("non-participating neuron dead") is the case when the random neurons that fail are all from the set of 40 non-participating neurons. In the third case ("random neuron dead") failed neurons are picked randomly from the set of all 100 neurons. Neuron death is initiated at 30 s (instantaneous neuron death) when the network is in a partially trained state as discussed in Section 0. In each case, five sets of randomly chosen afferents are killed to improve the statistical validity of the conclusion.

Section 0 discusses the specific cases of "random neuron dead". It compares the differences in the learning ability of the network in the case when a given percentage of neurons die instantaneously at 30 s (instantaneous neuron death) vs slowly over time (gradual neuron death). Instantaneous death would occur in the case when a strong radiation flare may kill certain afferents all at the same time. On the other hand, if the

radiation events are not strong but are distributed over time like in the case of war zones and radiation accidents, the afferent will fail slowly and randomly for 30 s.

6.2 Neuron Death Simulation Results

The following section presents the simulated characteristics of the neural network and changes in its learning ability in the case of neuron death. Section 0 discusses the spatio-temporal pattern learning ability of the neural network in the absence of any neuron death. Section 0 discusses the changes in the pattern learning ability of the network as a certain percentage of neurons die instantaneously during learning. Section 0 compares the learning ability of the network in the case of instantaneous vs gradual neuron death.

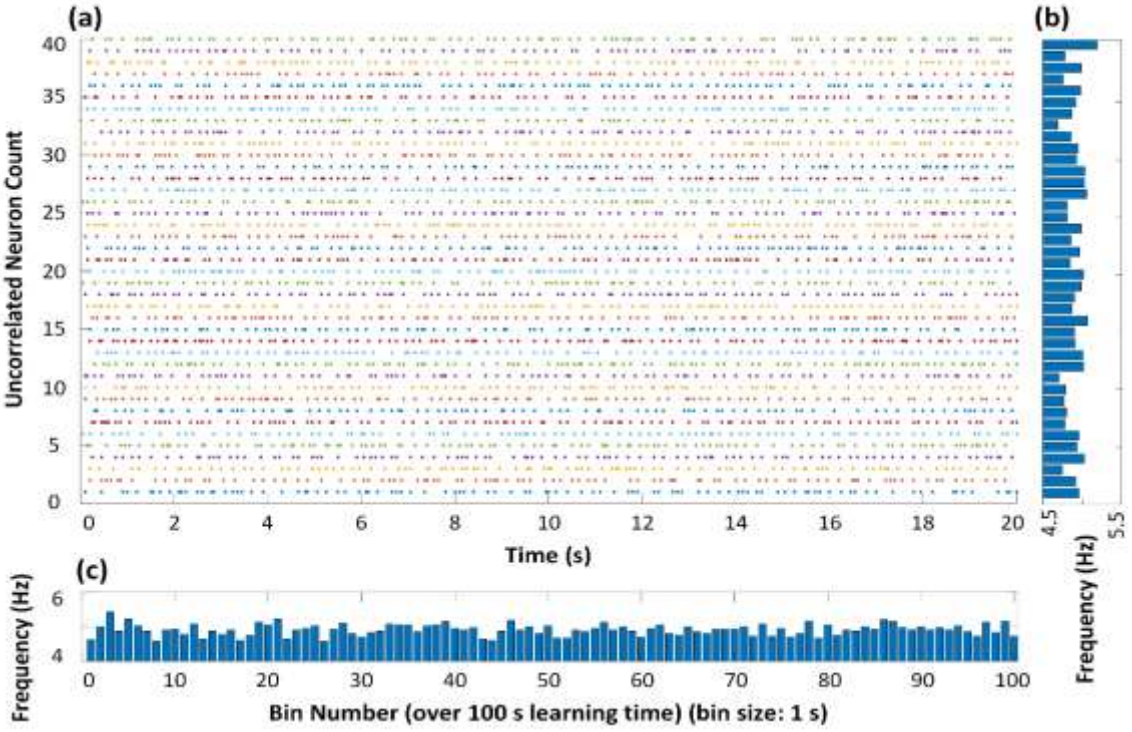

Figure 0.2 Scatter plot of the random behavior of the 40 non-participating afferents. (a) A 20 s snapshot of firing times of 40 afferents. (b) Random distribution of firing frequency of each of the 40 uncorrelated afferents with mean of 5 Hz. (c) Firing frequency of all 40 non-participating afferents over 100 s of stimulation, frequency is measured over 1 s period (bin size).

6.2.1 No Neuron Death

The neural network used for this dissertation has 100 pre-synaptic neurons with 60 participating (firing mutually correlated spikes) and 40 non-participating (firing Poisson distributed uncorrelated spikes) afferents. Figure 0.2 shows the spiking characteristics of the 40 uncorrelated/non-participating pre-synaptic afferents individually and collectively over time. Figure 0.2 (a) represents the firing times of 40 afferents for the first 20 s, random distribution is notable here. Figure 0.2 (b) shows the random distribution of firing frequency of each 40 uncorrelated afferents with a mean of 5 Hz. Figure 0.2 (c) captures the firing frequency of all 40 non-participating over 100 s of stimulation, the frequency is measured over 1 s period (bin size).

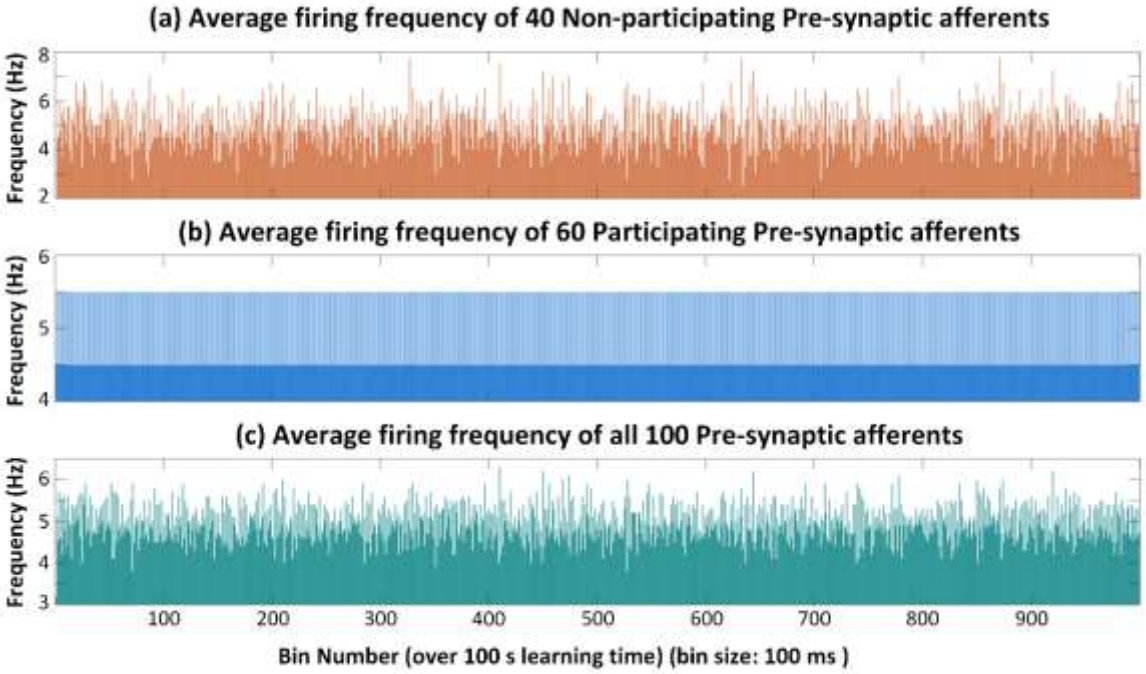

Figure 0.3 (a) Frequency distribution 40 non-participating afferents as they as fire Poisson distributed noise. (b) The frequency distribution of 60 participating afferents is not random as they are firing mutually correlated spikes. (c) Frequency distribution of the whole network over 100 s of the simulation.

Figure 0.3 presents the firing frequency of the network over 100 s of stimulation. In this case, the frequency is measured over reduced 100 ms bins to observe the finer distribution. 40 non-participating afferents in Figure 0.3 (a) show random frequency distribution as they are firing Poisson distributed noise. On the other hand, the frequency distribution of 60 participating afferents in Figure 0.3 (b) is not random because they are firing mutually correlated spikes at 5 Hz but just starting randomly as shown by N_{12} and N_{13} in Figure 0.8 (a). Figure 0.3 (c) shows the frequency distribution of the whole network over 100 s of the simulation. It can be noted that on average, the afferents are firing at a rate of 5 Hz.

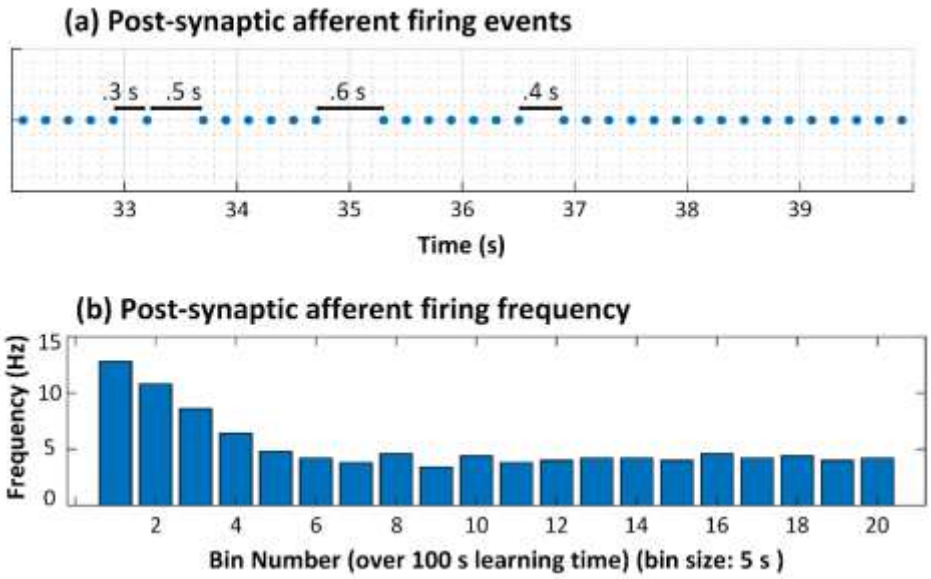

Figure 0.4 (a) The post-synaptic afferent is firing periodically every 0.2 s after 30 s except at a few misses (b) frequency response of the post-synaptic afferent over 100 s of simulation with a bin size of 5 s presenting the stabilized network over time to about 5 Hz, as non-participating afferents are suppressed.

Figure 0.4 shows the response of the post-synaptic LIF neuron during the 100 s learning period. As can be seen in Figure 0.4 (a) the post-synaptic afferent is firing periodically every 0.2 s after 30 s except at a few misses of 0.3 s, 0.5 s, and 0.6 s. Figure

0.4 (b) shows the frequency response over 100 s of simulation with a bin size of 5 s. Initially, the post-synaptic LIF neuron was overexcited due to high synaptic connectivity, but stabilized over time to about 5 Hz, as the network suppresses the non-participating afferents.

6.2.2 Instantaneous Neuron Death

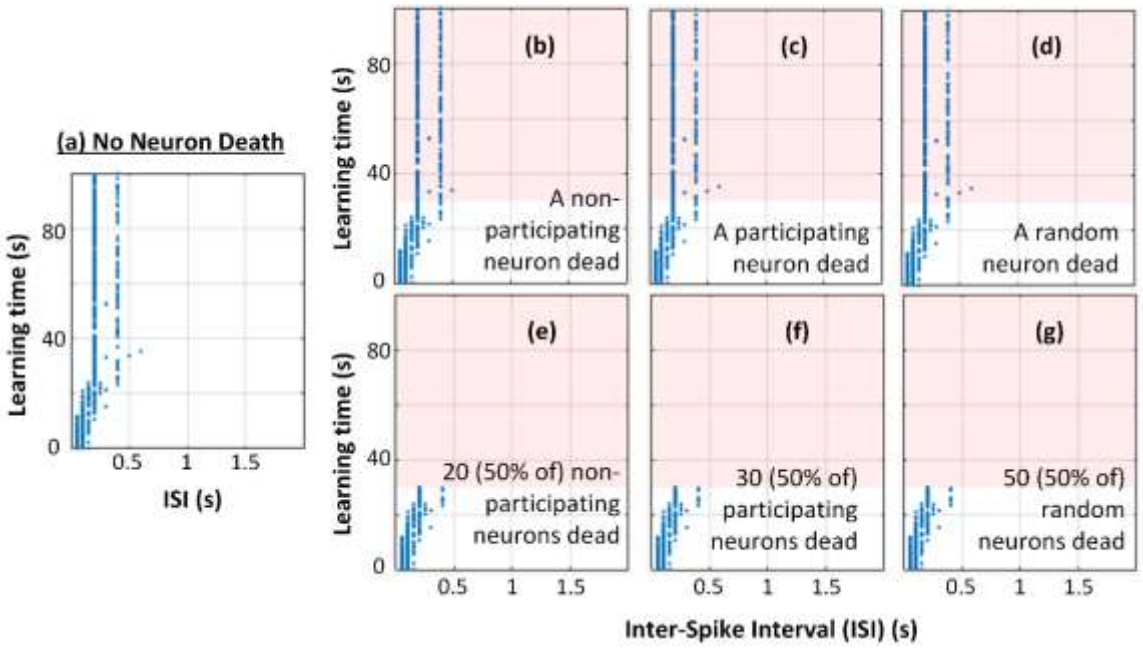

Figure 0.5 The post-synaptic neuron Interspike Interval (ISI) over the learning period. (a) ISI is about 0.2 s and 0.4 s in the case when no neuron death occurs. (b), (c) and (d) show the ISI when one neuron (in each case non-participating, participating and random) failed, but the network shows no degradation. (e), (f) and (g) present the ISI overtime when 50% of randomly selected afferents are dead and the network presents no post-synaptic neuron activity, thus resulting in complete network failure.

Figure 0.5 (a) shows the Interspike Interval (ISI), i.e. time between two spikes fired by the post-synaptic neuron, in the case when no neuron death occurs; the ISI is about 0.2 s and 0.4 s. Figure 0.5 (b), (c) and (d) show the ISI when one neuron in each case of non-participating, participating, and random failed. ISI is still about 0.2 s and 0.4 s in each of the cases and no change in the pattern learning behavior of the network is observed. Figure

0.5 (e), (f), and (g) presents the ISI overtime when 50% of randomly selected afferents failed in each case of the non-participating, participating, and random. After the neuron death at 30 s, no spiking in the post-synaptic neuron is noted and the network was not able to learn the pattern in any of the cases.

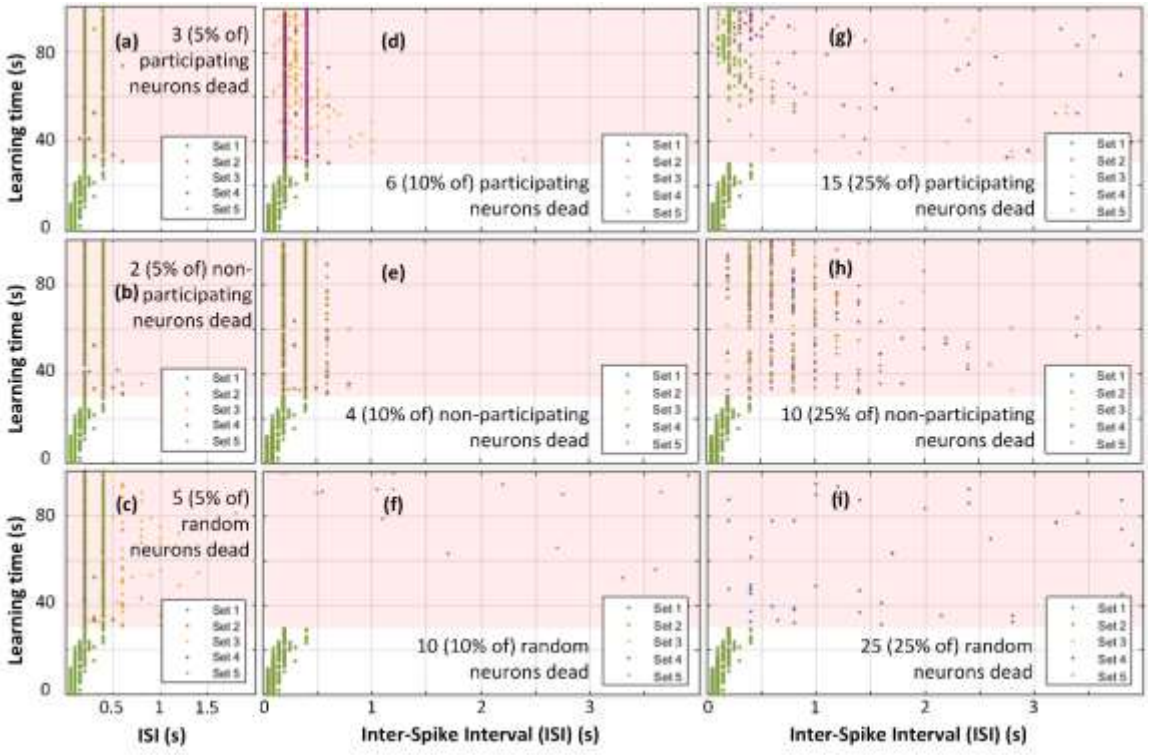

Figure 0.6 Post-synaptic neuron Interspike Interval (ISI) over the learning period. (a), (b), and (c) show the ISI when 5% of randomly selected neurons (in each case of the non-participating, participating, and random). The network was able to recover in the case of (a) and (b) but in the case of the random death, (c), the network recovery was not successful. (d), (e) and (f) presents the ISI overtime when 10% of the randomly selected afferents are dead. (d), (e), and (f) ((g), (h), and (i)) presents the ISI overtime when 10% (25%) of the randomly selected afferents are dead. The increase in network instability increases as the afferent death percentage increases, although random neuron death adds the most instability to the network.

Figure 0.6 (a), (b), and (c) shows the ISI when 5% of the afferents in each case of the participating, non-participating, and random failed. Interestingly both Figure 0.6 (a) and (b) where participating and non-participating neurons failed did not destabilize the system like a random failure in Figure 0.6 (c), where the network instability is notable.

Figure 0.6 (d), (e), and (f) show the ISI when 10% of the afferents in each case of the participating, non-participating, and random failed. It is observed that in Figure 0.6 (e), the non-participating afferent death keeps the system relatively stable. In the case of random neuron death, in Figure 0.6 (f), after 30 s, the post-synaptic neuron is not learning the pattern as the system becomes unstable and the ISI is randomly distributed. Similarly, Figure 0.6 (g), (h) and (i) shows the ISI of a post-synaptic neuron when 25% of the pre-synaptic afferents in each case of the participating, non-participating, and random failed. Random neuron death shows the most instability in this case too. In each case, 5 different sets of randomly selected afferents are disabled (set 1 to set 5).

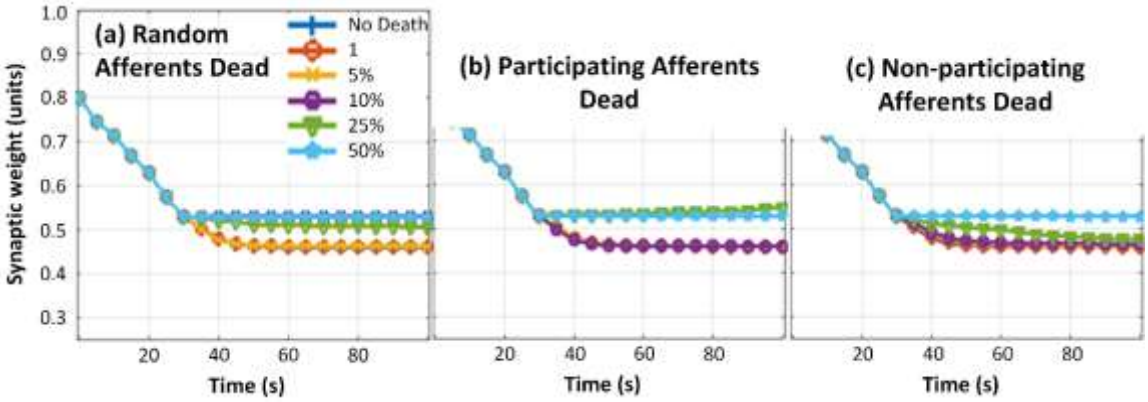

Figure 0.7 Normalized average synaptic weight evolution of all the 100 synaptic memristors in the network. (a) In the case of random afferent death, 10%, 25%, and 50% death cases show the deviation from the no-death case. (b) In the case of participating afferent death, 25% and 50% death cases show deviation from the no-death case. (c) In the case of non-participating afferent death, only a 50% death case shows deviation from the no-death case, and 25% recovers after an initial deviation, as the system tries to recover and regain stability.

Figure 0.7 shows the normalized average synaptic weight evolution of all the 100 synaptic memristors in the network. The deviation of weights was observed in the case of random afferent death (Figure 0.7 (a)) as all 10%, 25%, and 50% evolutions show deviation from the no-death case. On the other hand, non-participating afferent death (Figure 0.7 (c))

seems to destabilize the system the least, since even the 25% death marker evolves towards the more stable state to relearn the desired pattern.

6.2.3 Comparing Instantaneous and Gradual Neuron Death

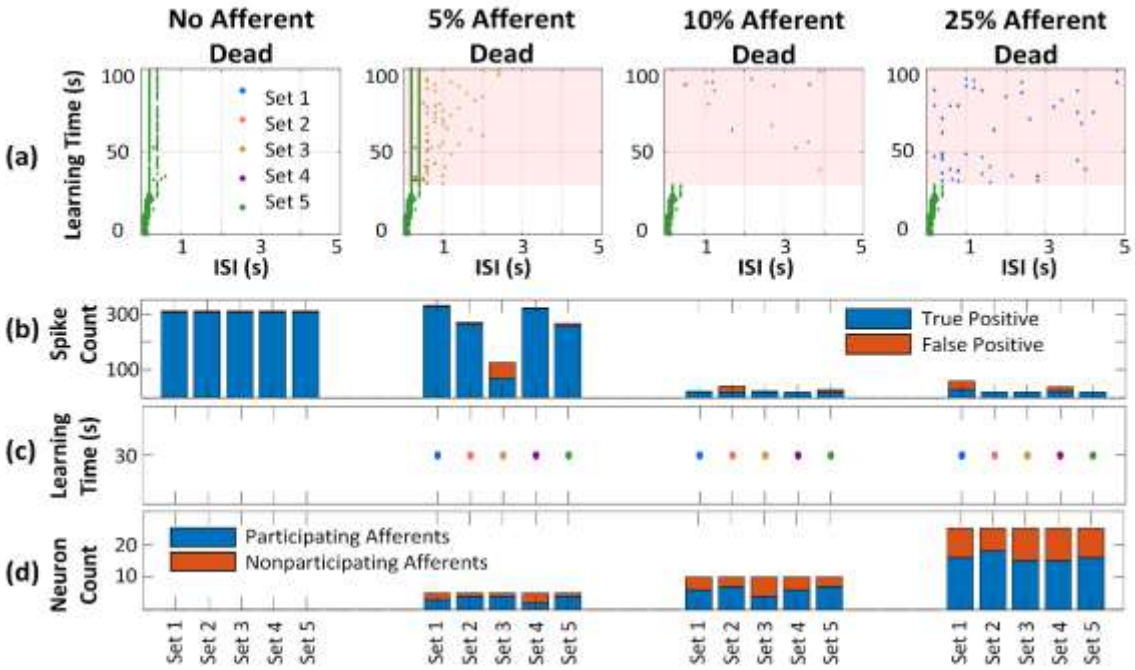

Figure 0.8 (a) Post-synaptic afferent interspike interval (ISI) over time. As the % of dead neurons increases, the network loses the pattern recognition capabilities. (b) The number of true positive and false positives recognized by the network, the network stops recognizing the pattern, and the post-synaptic afferent stops firing as neuron death increases. (c) Scatter plot showing the time of afferent death. All afferents are dead instantaneously at 30 s. (d) The distribution of dead participating and non-participating afferents in each of the five sets in each case.

Figure 0.8 shows the analysis of the network when random neurons die at the same time after 30 s of learning. Figure 0.8 (a) presents the post-synaptic afferent inter spiking interval over time, and as expected, as the percentage of dead neurons increases the network loses the pattern recognition capabilities. Figure 0.8 (b) presents the number of true positive and false positives recognized by the network. As expected, as the percentage of dead neurons increases the network stops recognizing the pattern, and the post-synaptic afferent

stops firing. Figure 0.8 (c) shows that the afferents are dead at 30 s and Figure 0.8 (d) shows the distribution of dead participating and non-participating afferents in each of the five sets in each case.

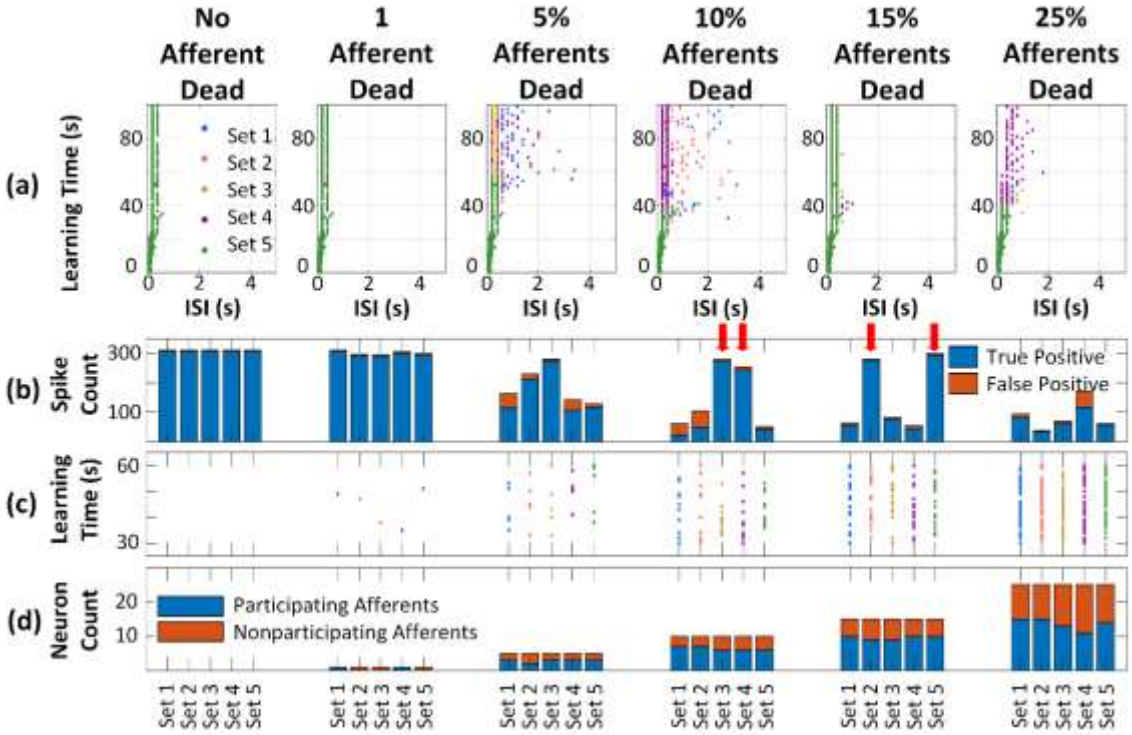

Figure 0.9 (a) Post-synaptic afferent interspike interval (ISI) over time. As the % of dead neurons increases the network loses the pattern recognition capabilities. (b) The number of true positives and false positives recognized by the network. The network stops recognizing the pattern and post-synaptic afferent stops firing as neuron death increases. (c) Scatter plot showing the timing of afferent death. Afferents are dying randomly between 60 s and 30 s. (d) The distribution of dead participating and non-participating afferents in each of the five sets in each case.

Figure 0.9 shows a similar analysis of the network as Figure 0.8 except in this case the pre-synaptic neuron death time is randomly occurring, starting at 30 s until 60 s, as shown in Figure 0.9 (c). Figure 0.9 (a) presents the post-synaptic afferent inter spiking interval over time and similarly shows the loss in the pattern recognition capabilities of the network as the percentage of dead neurons increases. Figure 0.9 (d) shows the distribution of dead participating and non-participating afferents in each of the five sets in each case.

Figure 0.9 (b) presents the number of true positive and false positives recognized by the network.

Unlike in Figure 0.8, where instantaneous afferent death completely disabled the network, in Figure 0.9 a few sets (marked by red arrows) were able to recover even in the case of high neuron death. Figure 0.9 (b) shows a 10% neuron death, the network spiked well for set 3 and set 4, and even at 25% neuron death set 2 and set 5 did not harm the network strongly. On the other hand, in Figure 0.8 (b), the network did not perform well in the case of any of the simulated sets. Overall, the network learning performed better when the afferents failed gradually as compared to sudden death.

6.3 Conclusion

This chapter discussed the pattern learning ability of a memristor-based electronic spiking neural network as the afferents in the network failed/died due to radiation, circuit failure, or other unforeseen events. A feed-forward perception network with 25 to 100 pre-synaptic neurons were connected to a post-synaptic LIF neuron via 25 to 100 memristors. The memristor acted as a synaptic bridge between the initial and the outer layer afferents, enforcing the STDP learning rule implemented using the biphasic pulses generated by the neurons.

The simulations were designed to observe the effect on the learning ability of the network for three cases when selectively only participating neurons were affected, non-participating neurons were disabled, or random/non-selective neuron death occurred after 30 s into learning in the network. As expected, the network learning ability was least affected in the case when the non-participating afferents were disabled selectively. In this case, the network shows the capacity to recover even when 25% (10) of the non-

participating afferents were disabled. On the other hand, when random/non-selective neuron death occurred in the network, the pattern learning ability degraded rapidly as 10% (10) of the total afferents were disabled and the network becomes unstable at 5% (5) neuron death. The chapter also simulated the case when neuron death is occurred gradually (instead of instantaneously at 30 s) between 30 s and 60 s of learning. The comparison shows that the network's learning ability was not as seriously deteriorated in the case of gradual neuron death as in the case of instantaneous death at 30 s. As the simulations show, in some of the cases of the gradual neuron death, the network was not affected by the neuron death. On the other hand, when all afferents die simultaneously at 30 s, the network did not recover.

The results conclude that the non-participating afferents contribute to improving the learning ability of the network even when partial learning is completed, emphasizing the importance of the non-participating neurons during the learning process. Instantaneous neuron death (due to radiation flare or a strong radiation event) will degrade the network's pattern recognition capability more than gradual neuron death (in the case of low but continuous radiation events, like in war zones, or post-nuclear accident sites). Thus, the electronic spiking networks do present the capability to recover/retain their learning capability even in the case of random neuron death. Such cases of neuron death can be observed in radiation prone areas like space and war zones when electronic neurons might experience a failure due to one or more radiation events.

CHAPTER SEVEN: CONCLUSIONS AND FUTURE WORK

This chapter outlines the conclusions derived from the body of work discussed throughout this dissertation. The chapter also talks about the implications of the work and suggests future studies and directions for the research.

7.1 Synaptic Modifications

A synaptic modification happens in the electronic SNNs when a radiation interaction event modifies the state of the memristive synapse. The effects of synaptic modification on the spatio-temporal pattern learning ability of the network are primarily discussed in 0.

The STDP rule governs the learning capability of SNNs and is influenced by factors such as memristive synaptic device threshold, the initial state of the synaptic device, and the shape, size, and magnitude of the biphasic pulse across the memristor. Radiation events add asymmetry to the STDP curve forcing stronger potentiation and thus, adding instability in the network. It was concluded that when the network was not undergoing training, the radiation effects build up and accumulates in the network over time. On the other hand, the network can overcome the radiation effects when in the learning/training phase. Thus, hardware-based SNNs that are continuously learning such as in [178]–[180] will survive better when exposed to radiation. The SNNs discussed in this dissertation consist of one layer, designed to learn one feature. They are observed to be radiation resilient with minimal (if any) feature loss at the stronger flux of $3x10^{10}$ $cm^{-2}s^{-1}$ or higher. The larger multilayer deep neural networks that convolve multiple features and do not rely completely

on one feature for object classification and identification should be more resilient to the effects of radiation, such as pixel upsets. Thus, future studies involving application-specific deep neural networks will help to understand the radiation effects in more detail. Further studies on different network architectures and topology will also provide more insight into the effects of radiation events on SNNs

7.2 Neuron Death

Neuron death occurs in electronic SNNs when one or more neurons in the network fail and become inactive due to degradation caused by radiation or general device/circuit failure. The effects of neuron death on the spatio-temporal pattern learning ability of the network are discussed in this dissertation in 0.

The chapter concludes that SNNs do have the ability to recover/retain their learned/trained pattern in case of neuron death. In the larger multi-layer SNNs, every neuron is connected to multiple synapses. The network in this study shows that the instantaneous neuron death is more deteriorating for an SNN than gradual neuron death overtime. Thus, an optimally connected network will be able to survive multiple gradual neuron deaths. Simulations also show that the non-participating afferents contribute to improving the learning ability of the network. More analysis is needed to understand the contribution of non-participating afferents. The study would help estimate the percentage of non-participating afferents needed for optimal learning and will also optimize the connection complexity in the larger networks.

REFERENCES

[1] A. R. Damasio, *The Scientific American book of the brain*. Lyons Press, 1999.

[2] "Computation Power: Human Brain vs Supercomputer," *Foglets.com*, 2019. [Online]. Available: https://foglets.com/supercomputer-vs-human-brain/. [Accessed: 20-May-2020].

[3] S. Ji, W. Xu, M. Yang, and K. Yu, "3D Convolutional Neural Networks for Human Action Recognition," *IEEE Trans. Pattern Anal. Mach. Intell.*, vol. 35, no. 1, pp. 221–231, Jan. 2013.

[4] D. C. Cireşan, U. Meier, L. M. Gambardella, and J. Schmidhuber, "Deep, Big, Simple Neural Nets for Handwritten Digit Recognition," *Neural Comput.*, vol. 22, no. 12, pp. 3207–3220, Dec. 2010.

[5] G. Hinton *et al.*, "Deep Neural Networks for Acoustic Modeling in Speech Recognition: The Shared Views of Four Research Groups," *IEEE Signal Process. Mag.*, vol. 29, no. 6, pp. 82–97, Nov. 2012.

[6] Z. Haider Khan, T. Sharmin Alin, and A. Hussain, "Price Prediction of Share Market Using Artificial Neural Network 'ANN,'" *Int. J. Comput. Appl.*, vol. 22, no. 2, pp. 42–47, May 2011.

[7] M. Bojarski *et al.*, "End to End Learning for Self-Driving Cars," Apr. 2016.

[8] F. M. Dias, A. Antunes, and A. M. Mota, "Artificial neural networks: A review of commercial hardware," *Eng. Appl. Artif. Intell.*, vol. 17, no. 8, pp. 945–952, 2004.

[9] H. Kim, M. P. Sah, C. Yang, T. Roska, and L. O. Chua, "Memristor bridge synapses," *Proc. IEEE*, vol. 100, no. 6, pp. 2061–2070, 2012.

[10] S. P. Adhikari, Changju Yang, Hyongsuk Kim, and L. O. Chua, "Memristor Bridge Synapse-Based Neural Network and Its Learning," *IEEE Trans. Neural Networks*

Learn. Syst., vol. 23, no. 9, pp. 1426–1435, Sep. 2012.

[11] V. S. Kumar, J. Prasad, V. L. Narasimhan, and S. Ravi, "Application of artificial neural networks for prediction of solar radiation for Botswana," in *2017 International Conference on Energy, Communication, Data Analytics and Soft Computing (ICECDS)*, 2017, pp. 3493–3501.

[12] A. Dmitriev, Y. Minaeva, Y. Orlov, I. Persiantsev, A. Suvorova, and I. Veselovsky, "Artificial Neural Network Applications to the Space Radiation Environment Modelling and Forcasting."

[13] "Artificial Intelligence and the Military | RealClearDefense." [Online]. Available: https://www.realcleardefense.com/articles/2017/09/07/artificial_intelligence_and_the_military_112240.html. [Accessed: 08-Mar-2019].

[14] "Kalashnikov develops fully automated neural network-based combat module — RT World News." [Online]. Available: https://www.rt.com/news/395375-kalashnikov-automated-neural-network-gun/. [Accessed: 08-Mar-2019].

[15] T. V. Santosh, G. Vinod, R. K. Saraf, A. K. Ghosh, and H. S. Kushwaha, "Application of artificial neural networks to nuclear power plant transient diagnosis," *Reliab. Eng. Syst. Saf.*, vol. 92, no. 10, pp. 1468–1472, Oct. 2007.

[16] A. S. Keys, J. H. Adams, J. D. Cressler, R. C. Darty, M. A. Johnson, and M. C. Patrick, "High-performance, radiation-hardened electronics for space and lunar environments," *AIP Conf. Proc.*, vol. 969, pp. 749–756, 2008.

[17] P. E. Dodd, M. R. Shaneyfelt, J. R. Schwank, and J. A. Felix, "Current and future challenges in radiation effects on CMOS electronics," *IEEE Trans. Nucl. Sci.*, vol. 57, no. 4 PART 1, pp. 1747–1763, 2010.

[18] K. H. Grace-Dutton, *Exploring the brain*, vol. 275, no. 7365. 2005.

[19] M. F. Bear, B. W. Connors, and M. A. Paradiso, "the Generation of an Action Potential," in *Neuroscience : exploring the brain*, Wolters Kluwer, 2015, p. 975.

[20] D. Iberri, "Action potential." [Online]. Available: https://commons.wikimedia.org/wiki/File:Action_potential.svg. [Accessed: 06-Jun-

2018].

[21] D. H. Hubel, *Eye, brain, and vision*. Scientific American Library, 1988.

[22] T. Splettstoesser, "SynapseSchematic," *Wikimedia commons*, 2015. [Online]. Available: https://commons.wikimedia.org/w/index.php?curid=41349083. [Accessed: 06-Jun-2018].

[23] P. L. McGeer, J. C. Eccles, and E. G. McGeer, "Synaptic Transmission in the Central Nervous System," in *Molecular Neurobiology of the Mammalian Brain*, Boston, MA: Springer US, 1978, pp. 101–140.

[24] A. Marzvanyan and A. F. Alhawaj, *Physiology, Sensory Receptors*. StatPearls Publishing, 2019.

[25] W. Maass, "Networks of spiking neurons: The third generation of neural network models," *Neural Networks*, vol. 10, no. 9, pp. 1659–1671, Dec. 1997.

[26] T. Masquelier, R. Guyonneau, and S. J. Thorpe, "Spike Timing Dependent Plasticity Finds the Start of Repeating Patterns in Continuous Spike Trains," *PLoS One*, vol. 3, no. 1, p. e1377, Jan. 2008.

[27] A. Waibel, T. Hanazawa, G. Hinton, K. Shikano, and K. J. Lang, "Phoneme recognition using time-delay neural networks," *IEEE Trans. Acoust.*, vol. 37, no. 3, pp. 328–339, Mar. 1989.

[28] H. Rowley, S. Baluja, and T. Kanade, "Neural Network-Based Face Detection," *Proc. IEEE Conf. Comput. Vis. Pattern Recognit.*, vol. 20, no. January, pp. 203–207, 1996.

[29] Y. LeCun *et al.*, "Backpropagation Applied to Handwritten Zip Code Recognition," *Neural Comput.*, vol. 1, no. 4, pp. 541–551, Dec. 1989.

[30] R. Fierro and F. L. Lewis, "Control of a nonholonomic mobile robot using neural networks.," *IEEE Trans. Neural Netw.*, vol. 9, no. 4, pp. 589–600, 1998.

[31] D. Baptista, F. Freitas, R. Vasconcelos, and F. Morgado-Dias, "Artificial Neural Netwroks: A Survey about Hardware and Software Use," *10th Port. Conf. Autom. Control*, no. July, pp. 286–291, 2012.

[32] J. Misra and I. Saha, “Artificial neural networks in hardware: A survey of two decades of progress,” *Neurocomputing*, vol. 74, no. 1–3, pp. 239–255, Dec. 2010.

[33] M. Laiho, E. Lehtonen, A. M. T. Russell, and P. Dudek, *Memristive synapses are becoming reality*. 2010.

[34] J. J. Yang, D. B. Strukov, and D. R. Stewart, “Memristive devices for computing,” *Nat. Nanotechnol.*, vol. 8, no. 1, pp. 13–24, Jan. 2013.

[35] E. Chicca, G. Indiveri, and R. Douglas, “An adaptive silicon synapse,” in *Proceedings of the 2003 International Symposium on Circuits and Systems, 2003. ISCAS ’03.*, 2003, vol. 1, pp. I-81-I–84.

[36] G. Indiveri, E. Chicca, and R. Douglas, “A VLSI array of low-power spiking neurons and bistable synapses with spike-timing dependent plasticity,” *IEEE Trans. Neural Networks*, vol. 17, no. 1, pp. 211–221, 2006.

[37] T. Asai, Y. Kanazawa, T. Hirose, and Y. Amemiya, “A MOS circuit for depressing synapse and its application to contrast-invariant pattern classification and synchrony detection,” *Neural Networks, 2004. Proceedings. 2004 IEEE Int. Jt. Conf.*, vol. 4, pp. 2619--2624 vol.4, 2004.

[38] R. C. Ivans, K. D. Cantley, and J. L. Shumaker, “A CMOS synapse design implementing tunable asymmetric spike timing-dependent plasticity,” in *Midwest Symposium on Circuits and Systems*, 2017, vol. 2017-August, pp. 1125–1128.

[39] J. M. Cruz-Albrecht, M. W. Yung, and N. Srinivasa, “Energy-efficient neuron, synapse and STDP integrated circuits,” *IEEE Trans. Biomed. Circuits Syst.*, vol. 6, no. 3, pp. 246–256, 2012.

[40] M. Ziegler and H. Kohlstedt, “Mimic synaptic behavior with a single floating gate transistor: A MemFlash synapse,” *J. Appl. Phys.*, vol. 114, no. 19, p. 194506, Nov. 2013.

[41] C. Diorio, P. Hasler, B. A. Minch, and C. A. Mead, “Single-transistor silicon synapse,” *IEEE Trans. Electron Devices*, vol. 43, no. 11, pp. 1972–1980, 1996.

[42] C. Diorio, “A floating-gate mos learning array with locally computed weight

updates," *IEEE Trans. Electron Devices*, vol. 44, no. 12, pp. 2281–2289, 1997.

[43] S. C. Liu and R. Möckel, "Temporally learning floating-gate VLSI synapses," *Proc. - IEEE Int. Symp. Circuits Syst.*, pp. 2154–2157, 2008.

[44] S. Ramakrishnan, P. E. Hasler, and C. Gordon, "Floating gate synapses with spike-time-dependent plasticity," *IEEE Trans. Biomed. Circuits Syst.*, vol. 5, no. 3, pp. 244–252, 2011.

[45] V. Kornijcuk *et al.*, "Scalable excitatory synaptic circuit design using floating gate based leaky integrators," *Sci. Rep.*, vol. 7, no. 1, p. 17579, 2017.

[46] F. Tenore, R. Vogelstein, R. Etienne-Cummings, G. Cauwenberghs, and P. Hasler, "A floating-gate programmable array of silicon neurons for central pattern generating networks," *Circuits Syst. 2006. ISCAS 2006. Proceedings. 2006 IEEE Int. Symp.*, pp. 4–3160, 2006.

[47] P. Hasler, C. Diorio, and B. A. Minch, "A four-quadrant floating-gate synapse," *Iscas `98 - Proc. 1998 Int. Symp. Circuits Syst. Vols 1-6*, vol. 00, no. c, pp. B29–B32, 1998.

[48] R. Douglas, "Neuromorphic Analogue VLSI," *Annu. Rev. Neurosci.*, vol. 18, no. 1, pp. 255–281, 1995.

[49] G. Q. Bi and M. M. Poo, "Synaptic modifications in cultured hippocampal neurons: dependence on spike timing, synaptic strength, and postsynaptic cell type.," *J. Neurosci.*, vol. 18, no. 24, pp. 10464–10472, 1998.

[50] W. Cai, F. Ellinger, and R. Tetzlaff, "Neuronal synapse as a memristor: Modeling pair- and triplet-based STDP rule," *IEEE Trans. Biomed. Circuits Syst.*, vol. 9, no. 1, pp. 87–95, 2015.

[51] I. Boybat *et al.*, "Neuromorphic computing with multi-memristive synapses," *Nat. Commun.*, vol. 9, no. 1, pp. 1–12, 2018.

[52] A. Adamatzky and L. Chua, Eds., *Memristor Networks*. Cham: Springer International Publishing, 2014.

[53] S. H. Jo, T. Chang, I. Ebong, B. B. Bhadviya, P. Mazumder, and W. Lu, "Nanoscale

memristor device as synapse in neuromorphic systems," *Nano Lett.*, vol. 10, no. 4, pp. 1297–1301, 2010.

[54] G. W. Burr *et al.*, "Neuromorphic computing using non-volatile memory," *Adv. Phys. X*, vol. 2, no. 1, pp. 89–124, 2017.

[55] S. Mandal and A. Saha, "Memristors act as synapses in neuromorphic architectures," in *2016 International Conference on Communication and Electronics Systems (ICCES)*, 2016, no. 3, pp. 1–5.

[56] T. D. Dongale, N. D. Desai, K. V. Khot, C. K. Volos, P. N. Bhosale, and R. K. Kamat, "An Electronic Synapse Device Based on TiO 2 Thin Film Memristor," *J. Nanoelectron. Optoelectron.*, vol. 13, no. 1, pp. 68–75, Jan. 2018.

[57] L. O. Chua, "Memristor—The Missing Circuit Element," *IEEE Trans. Circuit Theory*, vol. 18, no. 5, pp. 507–519, 1971.

[58] L. Chua, "Resistance switching memories are memristors," *Appl. Phys. A*, vol. 102, no. 4, pp. 765–783, Mar. 2011.

[59] L. O. Chua, "The fourth element," *Proc. IEEE*, vol. 100, no. 6, pp. 1920–1927, 2012.

[60] L. Chua, "Everything you wish to know about memristors but are afraid to ask," *Radioengineering*, vol. 24, no. 2, pp. 319–368, 2015.

[61] L. O. Chua, "Nonlinear circuit foundations for nanodevices, part I: the four-element torus," *Proc. IEEE*, vol. 9, no. 11, pp. 1830–1859, Nov. 2003.

[62] L. O. Chua and S. M. Kang, "Memristive Devices and Systems," *Proc. IEEE*, vol. 64, no. 2, pp. 209–223, 1976.

[63] L. Chua, "If it's pinched it's a memristor," *Memristors Memristive Syst.*, vol. 9781461490, pp. 17–90, 2014.

[64] D. B. Strukov, G. S. Snider, D. R. Stewart, and R. S. Williams, "The missing memristor found.," *Nature*, vol. 453, no. 7191, pp. 80–3, 2008.

[65] S. P. Adhikari, M. P. Sah, H. Kim, and L. O. Chua, "Three fingerprints of memristor," *IEEE Trans. Circuits Syst. I Regul. Pap.*, vol. 60, no. 11, pp. 3008–3021, 2013.

[66] Y. N. Joglekar and S. J. Wolf, “The elusive memristor: Properties of basic electrical circuits,” *Eur. J. Phys.*, vol. 30, no. 4, pp. 661–675, Jul. 2009.

[67] P. S. Georgiou, M. Barahona, S. N. Yaliraki, and E. M. Drakakis, “On memristor ideality and reciprocity,” *Microelectronics J.*, vol. 45, no. 11, pp. 1363–1371, Nov. 2014.

[68] C. Zuo and H. Cao, “One of signatures of a memristor,” *Commun. Nonlinear Sci. Numer. Simul.*, vol. 30, no. 1–3, pp. 128–138, 2016.

[69] M. A. Zidan, A. Chen, G. Indiveri, and W. D. Lu, “Memristive computing devices and applications,” *J. Electroceramics*, vol. 39, no. 1–4, pp. 4–20, 2017.

[70] Y. Yang, P. Gao, S. Gaba, T. Chang, X. Pan, and W. Lu, “Observation of conducting filament growth in nanoscale resistive memories,” *Nat. Commun.*, vol. 3, p. 732, 2012.

[71] C. Wang, H. Wu, B. Gao, T. Zhang, Y. Yang, and H. Qian, “Conduction mechanisms, dynamics and stability in ReRAMs,” *Microelectron. Eng.*, vol. 187–188, pp. 121–133, 2018.

[72] Y. Gonzalez-Velo, H. J. Barnaby, and M. N. Kozicki, “Review of radiation effects on ReRAM devices and technology,” *Semicond. Sci. Technol.*, vol. 32, no. 8, 2017.

[73] W. Guan, S. Long, Q. Liu, M. Liu, and W. Wang, “Nonpolar nonvolatile resistive switching in Cu doped ZrO2,” *IEEE Electron Device Lett.*, vol. 29, no. 5, pp. 434–437, 2008.

[74] K. Krishnan, T. Tsuruoka, C. Mannequin, and M. Aono, “Mechanism for Conducting Filament Growth in Self-Assembled Polymer Thin Films for Redox-Based Atomic Switches,” *Adv. Mater.*, vol. 28, no. 4, pp. 640–648, 2016.

[75] C. Chen, S. Gao, G. Tang, C. Song, F. Zeng, and F. Pan, “Cu-embedded AlN-based nonpolar nonvolatile resistive switching memory,” *IEEE Electron Device Lett.*, vol. 33, no. 12, pp. 1711–1713, 2012.

[76] S. J. Choi *et al.*, “In situ observation of voltage-induced multilevel resistive switching in solid electrolyte memory,” *Adv. Mater.*, vol. 23, no. 29, pp. 3272–3277,

2011.

[77] W. A. Hubbard *et al.*, “Nanofilament Formation and Regeneration during Cu/Al2O3Resistive Memory Switching,” *Nano Lett.*, vol. 15, no. 6, pp. 3983–3987, 2015.

[78] Z. Wang *et al.*, “Electrochemical metallization switching with a platinum group metal in different oxides,” *Nanoscale*, vol. 8, no. 29, pp. 14023–14030, 2016.

[79] S. Liu *et al.*, “Eliminating Negative-SET Behavior by Suppressing Nanofilament Overgrowth in Cation-Based Memory,” *Adv. Mater.*, vol. 28, no. 48, pp. 10623–10629, 2016.

[80] C. Schindler, S. C. P. Thermadam, R. Waser, and M. N. Kozicki, “Bipolar and unipolar resistive switching in cu-doped SiO2,” *IEEE Trans. Electron Devices*, vol. 54, no. 10, pp. 2762–2768, 2007.

[81] K. H. Kim, S. Hyun Jo, S. Gaba, and W. Lu, “Nanoscale resistive memory with intrinsic diode characteristics and long endurance,” *Appl. Phys. Lett.*, vol. 96, no. 5, pp. 5–8, 2010.

[82] Y. Yang *et al.*, “Electrochemical dynamics of nanoscale metallic inclusions in dielectrics,” *Nat. Commun.*, vol. 5, no. 1, p. 4232, Sep. 2014.

[83] J. P. Strachan *et al.*, “Direct identification of the conducting channels in a functioning memristive device,” *Adv. Mater.*, vol. 22, no. 32, pp. 3573–3577, 2010.

[84] U. Russo, D. Ielmini, C. Cagli, and A. L. Lacaita, “Filament Conduction and Reset Mechanism in NiO-Based Resistive-Switching Memory (RRAM) Devices,” *IEEE Trans. Electron Devices*, vol. 56, no. 2, pp. 186–192, Feb. 2009.

[85] S. Yu, Y. Wu, and H.-S. P. Wong, “Investigating the switching dynamics and multilevel capability of bipolar metal oxide resistive switching memory,” *Appl. Phys. Lett.*, vol. 98, no. 10, p. 103514, Mar. 2011.

[86] J. Y. Chen *et al.*, “Dynamic evolution of conducting nanofilament in resistive switching memories,” *Nano Lett.*, vol. 13, no. 8, pp. 3671–3677, 2013.

[87] J. Kwon *et al.*, “Transient Thermometry and High-Resolution Transmission

Electron Microscopy Analysis of Filamentary Resistive Switches," *ACS Appl. Mater. Interfaces*, vol. 8, no. 31, pp. 20176–20184, 2016.

[88] G. Niu *et al.*, "Electron holography on HfO_2/HfO_{2-x} bilayer structures with multilevel resistive switching properties," *Nanotechnology*, vol. 28, no. 21, p. 215702, 2017.

[89] U. Celano *et al.*, "Direct Probing of the Dielectric Scavenging-Layer Interface in Oxide Filamentary-Based Valence Change Memory," *ACS Appl. Mater. Interfaces*, vol. 9, no. 12, pp. 10820–10824, 2017.

[90] M. Sowinska *et al.*, "Hard x-ray photoelectron spectroscopy study of the electroforming in Ti/HfO2-based resistive switching structures," *Appl. Phys. Lett.*, vol. 100, no. 23, 2012.

[91] D. Ielmini, "Modeling the universal set/reset characteristics of bipolar RRAM by field- and temperature-driven filament growth," *IEEE Trans. Electron Devices*, vol. 58, no. 12, pp. 4309–4317, 2011.

[92] D. B. Strukov, F. Alibart, and R. Stanley Williams, "Thermophoresis/diffusion as a plausible mechanism for unipolar resistive switching in metal-oxide-metal memristors," *Appl. Phys. A Mater. Sci. Process.*, vol. 107, no. 3, pp. 509–518, 2012.

[93] C. Nail *et al.*, "Understanding RRAM endurance, retention and window margin trade-off using experimental results and simulations," *Tech. Dig. - Int. Electron Devices Meet. IEDM*, pp. 4.5.1-4.5.4, 2017.

[94] A. Pirovano, A. L. Lacaita, A. Benvenuti, F. Pellizzer, and R. Bez, "Electronic Switching in Phase-Change Memories," *IEEE Trans. Electron Devices*, vol. 51, no. 3, pp. 452–459, 2004.

[95] J. Secco, F. Corinto, and A. Sebastian, "Flux–Charge Memristor Model for Phase Change Memory," *IEEE Trans. Circuits Syst. II Express Briefs*, vol. 65, no. 1, pp. 1–1, 2017.

[96] A. Sebastian, M. Le Gallo, and D. Krebs, "Crystal growth within a phase change memory cell," *Nat. Commun.*, vol. 5, pp. 1–9, 2014.

[97] D. J. Wouters, R. Waser, and M. Wuttig, “Phase-Change and Redox-Based Resistive Switching Memories,” *Proc. IEEE*, vol. 103, no. 8, pp. 1274–1288, 2015.

[98] M. Gill, T. Lowrey, and J. Park, “ISSCC 2002 / SESSION 12 / TD : DIGITAL DIRECTIONS / 12 . 4 Ovonic Unified Memory - A High-Performance Nonvolatile Memory Technology for Stand-Alone,” *Current*, pp. 8–10, 2002.

[99] S. J. Ahn *et al.*, “Highly manufacturable high density phase change memory of 64Mb and beyond,” *IEDM, Tech. Dig. - Int. Electron Devices Meet.*, pp. 907–910, 2004.

[100] F. Pellizzer *et al.*, “A 90nm Phase Change Memory Technology for Stand-Alone Non-Volatile Memory Applications,” *Symp. VLSI Technol.*, pp. 122–123, 2006.

[101] M. Wuttig and N. Yamada, “Phase-change materials for rewriteable data storage,” *Nat. Mater.*, vol. 6, no. 11, pp. 824–832, 2007.

[102] S. Raoux, F. Xiong, M. Wuttig, and E. Pop, “Phase change materials and phase change memory,” *MRS Bull.*, vol. 39, no. 8, pp. 703–710, 2014.

[103] A. L. Lacaita and A. Redaelli, “The race of phase change memories to nanoscale storage and applications,” *Microelectron. Eng.*, vol. 109, pp. 351–356, 2013.

[104] F. Xiong, A. Liao, and E. Pop, “Inducing chalcogenide phase change with ultra-narrow carbon nanotube heaters,” *Appl. Phys. Lett.*, vol. 95, no. 24, pp. 1–5, 2009.

[105] Y.-M. Chang, P.-C. Hsiu, Y.-H. Chang, C.-H. Chen, T.-W. Kuo, and C.-Y. M. Wang, “Improving PCM Endurance with a Constant-Cost Wear Leveling Design,” *ACM Trans. Des. Autom. Electron. Syst.*, vol. 22, no. 1, pp. 1–27, Jun. 2016.

[106] K. A. Campbell, “Self-directed channel memristor for high temperature operation,” *Microelectronics J.*, vol. 59, no. August 2016, pp. 10–14, 2017.

[107] E. J. Fuller *et al.*, “Li-Ion Synaptic Transistor for Low Power Analog Computing,” *Adv. Mater.*, vol. 29, no. 4, p. 1604310, Jan. 2017.

[108] Y. Van De Burgt *et al.*, “A non-volatile organic electrochemical device as a low-voltage artificial synapse for neuromorphic computing,” *Nat. Mater.*, vol. 16, no. 4, pp. 414–418, 2017.

[109] M. T. Sharbati, Y. Du, J. Torres, N. D. Ardolino, M. Yun, and F. Xiong, "Low-Power, Electrochemically Tunable Graphene Synapses for Neuromorphic Computing," *Adv. Mater.*, vol. 30, no. 36, p. 1802353, Sep. 2018.

[110] L. Sun *et al.*, "Synaptic Computation Enabled by Joule Heating of Single-Layered Semiconductors for Sound Localization," *Nano Lett.*, vol. 18, no. 5, pp. 3229–3234, 2018.

[111] M. D. Levi, E. Markevich, and D. Aurbach, "The effect of slow interfacial kinetics on the chronoamperometric response of composite lithiated graphite electrodes and on the calculation of the chemical diffusion coefficient of Li Ions in graphite," *J. Phys. Chem. B*, vol. 109, no. 15, pp. 7420–7427, 2005.

[112] W. Bao *et al.*, "Approaching the limits of transparency and conductivity in graphitic materials through lithium intercalation," *Nat. Commun.*, vol. 5, no. May, pp. 1–9, 2014.

[113] H. Jang, Y. J. Park, X. Chen, T. Das, M.-S. Kim, and J.-H. Ahn, "Graphene-Based Flexible and Stretchable Electronics," *Adv. Mater.*, vol. 28, no. 22, pp. 4184–4202, Jun. 2016.

[114] M. H. Bae *et al.*, "Ballistic to diffusive crossover of heat flow in graphene ribbons," *Nat. Commun.*, vol. 4, 2013.

[115] "What is Radiation? – Mission to Mars." [Online]. Available: https://sites.duke.edu/missiontomars/the-mission/radiation/what-is-radiation/. [Accessed: 01-Feb-2020].

[116] "Radiation Basics | Radiation Protection | US EPA." [Online]. Available: https://www.epa.gov/radiation/radiation-basics. [Accessed: 01-Feb-2020].

[117] R. C. Lacoe, "Improving Integrated Circuit Performance Through the Application of Hardness-by-Design Methodology," *IEEE Trans. Nucl. Sci.*, vol. 55, no. 4, pp. 1903–1925, Aug. 2008.

[118] E. DeIonno, M. D. Looper, J. V. Osborn, H. J. Barnaby, and W. M. Tong, "Radiation effects studies on thin film TiO2 memristor devices," in *2013 IEEE Aerospace Conference*, 2013, pp. 1–8.

[119] Y. Gonzalez-Velo *et al.*, “Total-ionizing-dose effects on the resistance switching characteristics of chalcogenide programmable metallization cells,” *IEEE Trans. Nucl. Sci.*, vol. 60, no. 6, pp. 4563–4569, 2013.

[120] S. G. Dahl, R. Ivans, and K. D. Cantley, “Modeling Memristor Radiation Interaction Events and the Effect on Neuromorphic Learning Circuits,” in *Proceedings of the International Conference on Neuromorphic Systems - ICONS ’18*, 2018, pp. 1–8.

[121] S. G. Dahl, R. C. Ivans, and K. D. Cantley, “Learning Behavior of Memristor-Based Neuromorphic Circuits in the Presence of Radiation,” in *Proceedings of the International Conference on Neuromorphic Systems - ICONS ’19*, 2019, pp. 1–7.

[122] S. G. Dahl, R. C. Ivans, and K. D. Cantley, “Radiation Effect on Learning Behavior in Memristor-Based Neuromorphic Circuit,” in *2019 IEEE 62nd International Midwest Symposium on Circuits and Systems (MWSCAS)*, 2019, vol. 2019-Augus, pp. 53–56.

[123] Á.́ Rak and G. Cserey, “Macromodeling of the memristor in SPICE,” *IEEE Trans. Comput. Des. Integr. Circuits Syst.*, vol. 29, no. 4, pp. 632–636, 2010.

[124] S. Kvatinsky, E. G. Friedman, A. Kolodny, and U. C. Weiser, “TEAM: Threshold adaptive memristor model,” *IEEE Trans. Circuits Syst. I Regul. Pap.*, vol. 60, no. 1, pp. 211–221, 2013.

[125] C. Yakopcic, T. M. Taha, G. Subramanyam, R. E. Pino, and S. Rogers, “A memristor device model,” *IEEE Electron Device Lett.*, vol. 32, no. 10, pp. 1436–1438, 2011.

[126] H. Abdalla and M. D. Pickett, “SPICE modeling of memristors,” *Proc. - IEEE Int. Symp. Circuits Syst.*, pp. 1832–1835, 2011.

[127] M. D. Pickett *et al.*, “Switching dynamics in titanium dioxide memristive devices,” *J. Appl. Phys.*, vol. 106, no. 7, pp. 1–6, 2009.

[128] Y. V. Pershin and M. Di Ventra, “SPICE model of memristive devices with threshold,” *Radioengineering*, vol. 22, no. 2, pp. 485–489, 2013.

[129] S. Benderli and T. A. Wey, “On SPICE macromodelling of TiO2 memristors,”

Electron. Lett., vol. 45, no. 7, p. 377, 2009.

[130] S. Shin, K. Kim, and S. M. Kang, "Compact models for memristors based on charge-flux constitutive relationships," *IEEE Trans. Comput. Des. Integr. Circuits Syst.*, vol. 29, no. 4, pp. 590–598, 2010.

[131] D. Batas and H. Fiedler, "A memristor SPICE implementation and a new approach for magnetic flux-controlled memristor modeling," *IEEE Trans. Nanotechnol.*, vol. 10, no. 2, pp. 250–255, 2011.

[132] R. Kozma, R. E. Pino, and G. E. Pazienza, *Advances in neuromorphic memristor science and applications*. Springer, 2012.

[133] J. T. Diao and X. B. Tian, "A Simulation Method for Memristor Based Dopant Drift Model," *Appl. Mech. Mater.*, vol. 239–240, no. December 2012, pp. 915–920, Dec. 2012.

[134] Y. Chen and X. Wang, "Compact modeling and corner analysis of spintronic memristor," *2009 IEEE/ACM Int. Symp. Nanoscale Archit. NANOARCH 2009*, pp. 7–12, 2009.

[135] (Helen) Hai Li and M. Hu, "Compact model of memristors and its application in computing systems," *Des. Autom. Test Eur. Conf. Exhib. (DATE), 2010*, pp. 673–678, 2010.

[136] M. Hu, H. Li, Y. Chen, X. Wang, and R. E. Pino, "Geometry variations analysis of TiO2thin-film and spintronic memristors," *Proc. Asia South Pacific Des. Autom. Conf. ASP-DAC*, pp. 25–30, 2011.

[137] Z. Kolka, V. Biolkova, and D. Biolek, "Simplified SPICE model of TiO 2 memristor," in *2015 International Conference on Memristive Systems (MEMRISYS)*, 2015, no. 3, pp. 1–2.

[138] C. Yakopcic, T. M. Taha, G. Subramanyam, and R. E. Pino, "Generalized memristive device SPICE model and its application in circuit design," *IEEE Trans. Comput. Des. Integr. Circuits Syst.*, vol. 32, no. 8, pp. 1201–1214, 2013.

[139] R. E. Pino *et al.*, "Compact method for modeling and simulation of memristor

devices: Ion conductor chalcogenide-based memristor devices," *Proc. 2010 IEEE/ACM Int. Symp. Nanoscale Archit. NANOARCH 2010*, pp. 1–4, 2010.

[140] W. M. Tong *et al.*, "Radiation Hardness of TiO2 Memristive Junctions," *IEEE Trans. Nucl. Sci.*, vol. 57, no. 3, pp. 1640–1643, Jun. 2010.

[141] E. Deionno, M. D. Looper, J. V. Osborn, and J. W. Palko, "Displacement damage in Tio2 Memristor devices," *IEEE Trans. Nucl. Sci.*, vol. 60, no. 2, pp. 1379–1383, 2013.

[142] K. D. Cantley, A. Subramaniam, H. J. Stiegler, R. A. Chapman, and E. M. Vogel, "Hebbian learning in spiking neural networks with nanocrystalline silicon TFTs and memristive synapses," *IEEE Trans. Nanotechnol.*, vol. 10, no. 5, pp. 1066–1073, 2011.

[143] K. D. Cantley, A. Subramaniam, H. J. Stiegler, R. A. Chapman, and E. M. Vogel, "Neural Learning Circuits Utilizing Nano-Crystalline Silicon Transistors and Memristors," *IEEE Trans. Neural Networks Learn. Syst.*, vol. 23, no. 4, pp. 565–573, Apr. 2012.

[144] N. R. McDonald *et al.*, "Analysis of Dynamic Linear and Non-linear Memristor Device," *2010 Int. Jt. Conf. Neural Networks*, pp. 1–5, Jul. 2010.

[145] T. Prodromakis, B. P. Peh, C. Papavassiliou, and C. Toumazou, "A versatile memristor model with nonlinear dopant kinetics," *IEEE Trans. Electron Devices*, vol. 58, no. 9, pp. 3099–3105, 2011.

[146] Z. Biolek, D. Biolek, and V. Biolková, "SPICE model of memristor with nonlinear dopant drift," *Radioengineering*, vol. 18, no. 2, pp. 210–214, 2009.

[147] J. Yu, X. Mu, X. Xi, and S. Wang, "A Memristor Model with Piecewise Window Function," 2013.

[148] Q. Wan *et al.*, "(Bi0.2Sb0.8)2Te3 based dynamic synapses with programmable spatio-temporal dynamics," *APL Mater.*, vol. 7, no. 10, Oct. 2019.

[149] H. J. Barnaby *et al.*, "Impact of alpha particles on the electrical characteristics of TiO 2 memristors," *IEEE Trans. Nucl. Sci.*, vol. 58, no. 6 PART 1, pp. 2838–2844,

2011.

[150] M. J. Marinella *et al.*, “Initial Assessment of the Effects of Radiation on the Electrical Characteristics of TaOx Memristive Memories,” *IEEE Trans. Nucl. Sci.*, vol. 59, no. 6, pp. 2987–2994, Dec. 2012.

[151] B. Butcher *et al.*, “Proton-based total-dose irradiation effects on Cu/HfO2:Cu/Pt ReRAM devices,” *Nanotechnology*, vol. 21, no. 47, 2010.

[152] M. L. McLain *et al.*, “The susceptibility of TaOx-based memristors to high dose rate ionizing radiation and total ionizing dose,” *IEEE Trans. Nucl. Sci.*, vol. 61, no. 6, pp. 2997–3004, 2014.

[153] J. L. Taggart *et al.*, “Ionizing radiation effects on nonvolatile memory properties of programmable metallization cells,” *IEEE Trans. Nucl. Sci.*, vol. 61, no. 6, pp. 2985–2990, 2014.

[154] J. L. Taggart *et al.*, “Effects of 14 MeV neutron irradiation on the DC characteristics of CBRAM cells,” *2016 16th Eur. Conf. Radiat. Its Eff. Components Syst.*, pp. 1–4, Sep. 2016.

[155] B. Buczyk, “Poisson Distribution of Radioactive Decay,” pp. 6–9, 2009.

[156] S. L. Campbell and J. M. G. Duarte, “Poisson statistics of radioactive decay,” *Prepr. MIT Dep. Phys.*, pp. 3–6, 2008.

[157] S. Dutta, V. Kumar, A. Shukla, N. R. Mohapatra, and U. Ganguly, “Leaky Integrate and Fire Neuron by Charge-Discharge Dynamics in Floating-Body MOSFET,” *Sci. Rep.*, vol. 7, no. 1, Dec. 2017.

[158] M. J. Rozenberg, O. Schneegans, and P. Stoliar, “An ultra-compact leaky-integrate-and-fire model for building spiking neural networks,” *Sci. Rep.*, vol. 9, no. 1, p. 11123, Jul. 2019.

[159] X. Wu, V. Saxena, K. Zhu, and S. Balagopal, “A CMOS Spiking Neuron for Brain-Inspired Neural Networks with Resistive Synapses and in Situ Learning,” *IEEE Trans. Circuits Syst. II Express Briefs*, vol. 62, no. 11, pp. 1088–1092, Nov. 2015.

[160] L. F. Abbott and S. B. Nelson, “Synaptic plasticity: Taming the beast,” *Nat.*

Neurosci., vol. 3, no. 11s, pp. 1178–1183, 2000.

[161] G. Bi and M. Poo, "S YNAPTIC M ODIFICATION BY C ORRELATED A CTIVITY : Hebb ' s Postulate Revisited," *Annu. Rev. Neurosci.*, vol. 24, pp. 139–166, 2001.

[162] K. A. Campbell, K. T. Drake, and E. H. Barney Smith, "Pulse Shape and Timing Dependence on the Spike-Timing Dependent Plasticity Response of Ion-Conducting Memristors as Synapses," *Front. Bioeng. Biotechnol.*, vol. 4, no. December, p. 97, Dec. 2016.

[163] B. Linares-Barranco and T. Serrano-Gotarredona, "Exploiting Memristance in Adaptive Asynchronous Spiking Neuromorphic Nanotechnology Systems," *Nanotechnol. (IEEE-NANO), 2009 9th IEEE Conf.*, vol. 06, pp. 601–604, 2009.

[164] T. Serrano-Gotarredona, T. Masquelier, T. Prodromakis, G. Indiveri, and B. Linares-Barranco, "STDP and sTDP variations with memristors for spiking neuromorphic learning systems," *Front. Neurosci.*, vol. 7, no. 7 FEB, pp. 1–15, 2013.

[165] N. Panwar, B. Rajendran, and U. Ganguly, "Arbitrary Spike Time Dependent Plasticity (STDP) in memristor by analog waveform engineering," *IEEE Electron Device Lett.*, vol. 38, no. 6, pp. 740–743, 2017.

[166] J. Lisman and N. Spruston, "Questions about STDP as a General Model of Synaptic Plasticity," *Front. Synaptic Neurosci.*, vol. 2, p. 140, 2010.

[167] K. D. Cantley, R. C. Ivans, A. Subramaniam, and E. M. Vogel, "Spatio-temporal pattern recognition in neural circuits with memory-transistor-driven memristive synapses," in *2017 International Joint Conference on Neural Networks (IJCNN)*, 2017, pp. 4633–4640.

[168] S. Wozniak, T. Tuma, A. Pantazi, and E. Eleftheriou, "Learning spatio-temporal patterns in the presence of input noise using phase-change memristors," in *2016 IEEE International Symposium on Circuits and Systems (ISCAS)*, 2016, vol. 2016-July, pp. 365–368.

[169] S. R. Kheradpisheh, M. Ganjtabesh, S. J. Thorpe, and T. Masquelier, "STDP-based

spiking deep convolutional neural networks for object recognition," *Neural Networks*, vol. 99, pp. 56–67, Mar. 2018.

[170] J. H. Morrison and P. R. Hof, "Life and death of neurons in the aging brain," *Science (80-.).*, vol. 278, no. 5337, pp. 412–419, Oct. 1997.

[171] D. G. T. Barrett, S. Denève, and C. K. Machens, "Optimal compensation for neuron loss," *Elife*, vol. 5, no. DECEMBER2016, Dec. 2016.

[172] V. Castelli *et al.*, "Neuronal cells rearrangement during aging and neurodegenerative disease: Metabolism, oxidative stress and organelles dynamic," *Frontiers in Molecular Neuroscience*, vol. 12. Frontiers Media S.A., p. 132, 27-May-2019.

[173] R. D. Terry *et al.*, "Physical basis of cognitive alterations in alzheimer's disease: Synapse loss is the major correlate of cognitive impairment," *Ann. Neurol.*, vol. 30, no. 4, pp. 572–580, Oct. 1991.

[174] N. Li, K. Daie, K. Svoboda, and S. Druckmann, "Robust neuronal dynamics in premotor cortex during motor planning," *Nature*, vol. 532, no. 7600, pp. 459–464, Apr. 2016.

[175] M. C. Leary and J. L. Saver, "Annual Incidence of First Silent Stroke in the United States: A Preliminary Estimate," *Cerebrovasc. Dis.*, vol. 16, no. 3, pp. 280–285, 2003.

[176] R. A. Burghard and C. W. Gwyn, "Radiation failure modes in CMOS integrated circuits," *IEEE Trans. Nucl. Sci.*, vol. 20, no. 6, pp. 300–306, 1973.

[177] A. Paccagnella, A. Cester, and G. Cellere, "Ionizing radiation effects on MOSFET thin and ultra-thin gate oxides," in *Technical Digest - International Electron Devices Meeting, IEDM*, 2004, pp. 473–476.

[178] N. Qiao *et al.*, "A reconfigurable on-line learning spiking neuromorphic processor comprising 256 neurons and 128K synapses," *Front. Neurosci.*, vol. 9, no. APR, p. 141, Apr. 2015.

[179] S. Sayyaparaju, G. Chakma, S. Amer, and G. S. Rose, "Circuit techniques for online

learning of memristive synapses in CMOS-memristor neuromorphic systems," in *Proceedings of the ACM Great Lakes Symposium on VLSI, GLSVLSI*, 2017, vol. Part F127756, pp. 479–482.

[180] A. Wyer *et al.*, "Evaluating online-learning in memristive neuromorphic circuits," in *ACM International Conference Proceeding Series*, 2017, vol. 2017-July, pp. 1–8.

APPENDIX A

Non-Linear Memristor Model

```
// Verilog-A code for non-linear memristor model (Vth and window function included)
`include "constants.vams"
`include "disciplines.vams"

// Take care of current blowup error
nature Current
   abstol = 1e-14 ;
        access = I ;
        units = "A" ;
        blowup = 1e12 ;
endnature

// Start of the module
module memristor_verilog_neurolearning(In, Out, w_D, RinitK, Vth);
input IRad_sc, RinitK, Vth;
output w_D;
inout In, Out;

electrical In, Out, w_D , capaux, capgnd, IRad_sc, RinitK, Vth;
branch (In, Out) mem;
branch (capgnd, capaux) cap;

parameter real Roff = 100k ;          //off-resistance in Ohms
parameter real Ron = 10k ;            //on-resistance in Ohms
parameter real D = 10n ;              //thickness of device in m
parameter real mu = 10f ;             //dopant ion mobility in m2/V s

real Gxconst, initcapV, Rhigh,Rinit,Vthp,Vthn,var,a,capv;   //variables used

// Start of the analog
analog begin
        Rhigh = Roff ;
        Vthp = 1* V(Vth);             // positive Vth
        Vthn = -1*V(Vth);             // negative Vth
        Rinit = 1000* V(RinitK);      // initial device state if defined externally by user
        //a = 45 + (abs( $random%30));              // generate random Rinit,
        //  Rinit = 1000* a;

        initcapV = (Rinit-Ron)/(Rhigh-Ron);       //initial voltage across capacitor
        Gxconst = mu*Ron/(D*D);           //Gx = Gxconst*Imem*window function

// Start of the analysis
if (analysis("ic"))begin              // to reflect the initial state of the device
        V(cap) <+ initcapV ;          //initializing capacitor to initial state
        Capv = V(cap);
```

```
end else begin
        V(capgnd) <+ 0;
        I(cap) <+ ddt(V(cap));          //current contribution from cap

 //including Vthn and Vthp, to include threshold to the device
        if  ((V(mem) > Vthp) || (V(mem) < Vthn)) begin
                //adding the window function
                I(capaux) <+ Gxconst*I(mem) *(1-(pow(((2*V(cap))-1),8)));
        end

end     // End of the analysis

//check the boundary conditions
if(V(cap) >= 1)   V(cap) <+1;
if(V(cap) <= 0)    V(cap) <+0;

V(w_D) <+ V(cap);                       //state (w/D) of the memristor
V(mem) <+ I(mem)* ((Rhigh) -( Rhigh - Ron)* V(cap));
                                //voltage across the memristor, V(mem) = V*Roff+Emem

end             // End of the analog
endmodule       // End of the module
```

APPENDIX B

Intercalated Ion Memristor Model

```
// Verilog-A code for intercalated-ion memristor model
`include "constants.vams"
`include "disciplines.vams"
`timescale 1us / 1us                    // defining dt time scale

// Start of the module
module basic_v1_Diffu_Drft_verilog(In, Out, IGsc, Rmem);
output Rmem;
inout In, Out;
input IGsc;

electrical In, Out, IGsc, capgnd, capactive ,Rmem ;
branch (In,Out) mem;
branch (capactive,capgnd) cap;

parameter real Ron = 0.1k ;             //on-resistance in Ohms
parameter real Roff = 1k ;              //off-resistance in Ohms
parameter real Rinit = 0.5k ;           //initial-resistance in Ohms
parameter real Rdrift1c = 60e12 ;       // resistance change for 1 C of current

parameter real w = 4u ;                 // width of graphene layer in m
parameter real l = 15u ;                // length of graphene layer in m
parameter real D = 0.4n ;               // diffusion constant for Li in m2/s
parameter real tao3 = 19 ;              // diffusion equ 3rd time constant
parameter real c1  = -13.6 ;            // diffusion equ 1st constant
parameter real c2  = -7.7 ;             // diffusion equ 2nd constant
parameter real c3 = 21.3 ;              // diffusion equ 3rd constant

real tao2, tao1;                // variables diffusion equ 1st and 2nd time constant
real M, delM;                           // variables for memristance
real source_dir, t, sc_pulse_arrived;
real diffusion_start_time, diffu_M,diffu_G, M_before_diffusion;

// Start of the analog
analog begin
        tao2 = (l*l)/(2*D);
        tao1 = (w*w)/(2*D);

// Start of the analysis
if (analysis("ic")) begin               // to reflect the initial state of the device
        M = Rinit;                      // memristor initial condition
        V(cap) <+ Rinit/Rdrift1c;       // capacitor initial condition
        sc_pulse_arrived = 0;           // setting sc pulse arrival to False

 end else begin
        I(cap) <+- I(IGsc);             // charging capacitor V=It (Q=CV (C=1,
```

```
                Q=V), Q=It) from current source
        V(capgnd) <+ 0;
        I(cap) <+ ddt(V(cap));          // charge the capacitor

//Capturing Drift
        if  (I(IGsc) != 0) begin          // if state-change(sc) pulse is on
                M = V(cap) * Rdrift1c;
                source_dir = -I(IGsc);          //if the discharge was -ve or +ve
                sc_pulse_arrived = 1;           // setting sc pulse arrival to True
                M_before_diffusion = M;       // setting max drift resistance
                diffusion_start_time = $abstime ;       //diffusion start time

//Capturing Diffusion
        end else if ((I(IGsc) == 0) && (sc_pulse_arrived == 1) && (($abstime-
diffusion_start_time) < 1)) begin
                t = $abstime-diffusion_start_time;     // diffusion time (dt) calculation
                diffu_M = ((c1 * exp(-t/tao1)) + (c2 * exp(-t/tao2)) + (c3 * exp(-
                                t/tao3)));          //change due to diffusion
                if (diffu_M < 0) diffu_M = 0;          //following boundary condition
                        //negative state change
                if (source_dir < 0) M = M_before_diffusion - diffu_M ;
                        //positive state change
                else M = M_before_diffusion + diffu_M;

                V(cap) <+ M/Rdrift1c;                  //update the capacitor voltage

//neither Drift nor Diffusion happening
        end else begin M = M;t = 0;
        end

end     // End of the analysis

V(Rmem) <+  M  ;                                       //device resistance at a given time
V(mem) <+ I(mem)* M ;                                  //voltage across memristor

end             // End of the analog
endmodule       // End of the module
```

APPENDIX C

Non-Linear Memristor Model with Radiation

```
// Verilog-A code for non-linear memristor model with state change radiation
`include "constants.vams"
`include "disciplines.vams"

// Take care of current blowup error
nature Current
   abstol = 1e-14 ;
        access = I ;
        units = "A" ;
        blowup = 1e12 ;
endnature

// Start of the module
module memristor_verilog_neurolearning_rad(In, Out, w_D, IRad_sc, RinitK, Vth);
input IRad_sc, RinitK, Vth;
output w_D;
inout In, Out;

electrical In, Out, w_D , capaux, capgnd, IRad_sc, RinitK, Vth;
branch (In, Out) mem;
branch (capgnd, capaux) cap;

parameter real Roff = 100k ;          //off-resistance in Ohms
parameter real Ron = 10k ;            //on-resistance in Ohms
parameter real D = 10n ;              //thickness of device in m
parameter real mu = 10f ;             //dopant ion mobility in m2/V s

real Gxconst, initcapV, Rhigh,Rinit,Vthp,Vthn,var,a,capv;   //variables used

// Start of the analog
analog begin
        Rhigh = Roff ;
        Vthp = 1* V(Vth);             // positive Vth
        Vthn = -1*V(Vth);             // negative Vth
        Rinit = 1000* V(RinitK);      // initial device state if defined externally by user
//a=45+ (abs( $random%30));           // generate random Rinit,
//  Rinit = 1000* a;

        initcapV = (Rinit-Ron)/(Rhigh-Ron);          //initial voltage across capacitor
        Gxconst = mu*Ron/(D*D);             //Gx = Gxconst*Imem*window function

// Start of the analysis
if (analysis("ic"))begin                    // to reflect the initial state of the device
        V(cap) <+ initcapV ;                //initializing capacitor to initial state
        Capv = V(cap);
```

```
end else begin
        V(capgnd) <+ 0;
        I(cap) <+ ddt(V(cap));                  //current contribution from cap

        //including Vthn and Vthp, to include threshold to the device
        if  ((V(mem) > Vthp) || (V(mem) < Vthn)) begin
                //adding the window function
                I(capaux) <+ Gxconst*I(mem) *(1-(pow(((2*V(cap))-1),8)));
        end

        //including the state change radiation current effect in auxiliary circuit
        I(capaux) <+ (-1) * Gxconst*I(IRad_sc)*(1-(pow(((2*V(cap))-1),8)));
        V(capgnd) <+ 0;

end     // End of the analysis

//check the boundary conditions
if(V(cap)>=1)   V(cap)<+1;
if(V(cap)<=0)    V(cap)<+0;

V(w_D) <+ V(cap);                               //state (w/D) of the memristor
V(mem) <+ I(mem)* ((Rhigh) -( Rhigh - Ron)* V(cap));
                                //voltage across the memristor, V(mem)= V*Roff+Emem

end             // End of the analog
endmodule       // End of the module
```

APPENDIX D

Leaky Integrate-and-Fire Circuit

```
// Verilog-A code for leaky integrate-and-fire (LIF) circuit
`include "constants.vams"
`include "disciplines.vams"
`timescale 1us / 1ns

// Take care of current blowup error
nature Current
   abstol = 1e-14 ;
        access = I ;
        units = "A" ;
        blowup = 1e12 ;
endnature

// Start of the module
module LIF_verilog_extcap(PostIn, PostVth, testout, LICcap, gnd);
input PostVth;
inout PostIn, LICcap, gnd;
output testout;

electrical PostIn, PostVth, testout,gnd, LICcap,LICaux,LICPostIn,firesource ;
branch (PostIn,LICaux) LICswitch;
branch (LICaux,LICcap) LICcharging;
branch (LICcap,gnd) LICdischarging;

        // LIF circuit parameters
parameter real Rcharging = 10e9 ;           // charging resistance
parameter real Rdischarging = 200e9 ;       // discharging resistance
parameter real Rpostdischarge = 10e9 ;      // cap discharge during post spike
        // output pulse parameters
parameter real pulse_width = 10e-3 ;        // output pulse width
parameter real pulse_max_amp = 5 ;          // maximum output pulse V
        // circuit connecting and disconnecting parameters
parameter real Ron = 0 ;                    // connection valid, current flowing
parameter real Roff = 1e300;                // connection invalid, no current flowing

real state, tfire, t, Rfire, LICdischarging_R, LICswitch_R, V_fire, charging_timecont,
discharging_timecont, chargingstart_starttime, charging, discharging, charging_amp,
discharging_amp, discharging_endtime;           //variables used

// Start of the analog
analog begin
        charging_timecont = 0.03*pulse_width;           // charging constant
        discharging_timecont = 0.4*pulse_width;         // discharging constant
        chargingstart_starttime = 0.05*pulse_width;     // charging start time
        discharging_endtime = 0.75*pulse_width;         // discharging end time
        charging = exp(-chargingstart_starttime/charging_timecont);
```

```
        discharging = exp(-discharging_endtime/discharging_timecont);
        charging_amp = pulse_max_amp;                    // charging max voltage
        discharging_amp = pulse_max_amp*0.25;            // discharging max voltage

// Start of the analysis
if (analysis("ic"))begin
        state = 0;
        LICdischarging_R = Roff;
        LICswitch_R = Ron;
        V_fire = 0;

end else begin
        V(LICPostIn) <+ V(PostIn);                       //separate circuit and LIF circuit
        V(LICswitch) <+ I(LICswitch)*LICswitch_R;        //(dis)connect LIC circuit
        V(LICcharging) <+ I(LICcharging)*Rcharging;      //charges the LIF capacitor
        V(LICdischarging) <+ I(LICdischarging)*LICdischarging_R;
                                                         //discharges the LIF capacitor

//if vcap < vth, post-synaptic neuron is not firing
        if  (( V(LICcap) < V(PostVth)) && (state == 0))begin
                tfire = $realtime;
                LICswitch_R = Ron;                       //connect LIC circuit
                if (V(PostIn) < V(LICcap)) begin
                        LICdischarging_R = Rdischarging; //turn on cap discharging
                        LICswitch_R = Roff;              //disconnect LIC circuit
                end
        end

//if vcap > vth, post-synaptic neuron starts firing
        else begin
                LICdischarging_R = Rpostdischarge;       //turn on cap discharging
                LICswitch_R = Roff;                      //disconnect LIC circuit
                State = 1;                               //set state to 1 for firing
                T = $realtime-tfire;                     //start timer for pulse width

        //start of the LIF spike
                if (t<= (pulse_width * 0.05)) begin   //generate potentiation part of the spike
                        V_fire = charging_amp *(t/(pulse_width * 0.05));
                end else if ((t > (pulse_width * 0.05)) && (t <= (pulse_width * 0.8))) begin
                                                      //generate depression part of the spike
                        V_fire = discharging_amp * (t - (pulse_width * 0.8))/(pulse_width
                        * 0.75);
                end else begin
                        V_fire = 0;
                        state = 0;                       //set state to 0 for not firing
                        LICdischarging_R = Roff;         //turn on cap discharging
```

```
                LICswitch_R = Ron;                  //turn on LIC switch
            end     //end of LIF spike

            V(PostIn) <+ V_fire;        //initialize input terminal voltage  to V_fire

        end     //post-synaptic neuron ends firing

end     // End of the analysis

V(testout) <+ V(LICPostIn) ;                //test terminal voltage, for circuit check

end             // End of the analog
endmodule       // End of the module
```